NSEL Report Series
Report No. NSEL-037
May 2015

Monitoring, Modeling, and Hybrid Simulation
An Integrated Bayesian-based Approach to High-fidelity Fragility Analysis

Jian Li

and

Billie F. Spencer, Jr.

Department of Civil and Environmental Engineering
University of Illinois at Urbana-Champaign

UILU-ENG-2015-1803

ISSN: 1940-9826

The Newmark Structural Engineering Laboratory (NSEL) of the Department of Civil and Environmental Engineering at the University of Illinois at Urbana-Champaign has a long history of excellence in research and education that has contributed greatly to the state-of-the-art in civil engineering. Completed in 1967 and extended in 1971, the structural testing area of the laboratory has a versatile strong-floor/wall and a three-story clear height that can be used to carry out a wide range of tests of building materials, models, and structural systems. The laboratory is named for Dr. Nathan M. Newmark, an internationally known educator and engineer, who was the Head of the Department of Civil Engineering at the University of Illinois [1956-73] and the Chair of the Digital Computing Laboratory [1947-57]. He developed simple, yet powerful and widely used, methods for analyzing complex structures and assemblages subjected to a variety of static, dynamic, blast, and earthquake loadings. Dr. Newmark received numerous honors and awards for his achievements, including the prestigious National Medal of Science awarded in 1968 by President Lyndon B. Johnson. He was also one of the founding members of the National Academy of Engineering.

Contact:
Prof. B.F. Spencer, Jr.
Director, Newmark Structural Engineering Laboratory
2213 NCEL, MC-250
205 North Mathews Ave.
Urbana, IL 61801
Telephone (217) 333-8630
E-mail: bfs@illinois.edu

This technical report is based on the first author's doctoral dissertation of the same title, which was completed in June 2013. The second author served as the dissertation advisor for this work.

Financial support for this research was provided in part by the National Science Foundation under NSF Grants No. CMS-060043, CMMI-0724172, CMMI-0928886, and CNS-1035573. In addition, we would like to thank the numerous collaborators on this work, including Amr Elnashai, Gul Agha, Kirill Mechitov, Sung-Han Sim, Tomonori Nagayama, Sheng-Lin Lin, Manuel Ruiz-Sandoval, Hongki Jo, Chia-Ming Chang, Brian Phillips, Robin Kim, Parya Moinzadeh, and Lauren Linderman.

The cover photographs are used with permission. The Trans-Alaska Pipeline photograph was provided by Terra Galleria Photography (http://www.terragalleria.com/).

ABSTRACT

Fragility functions are one of the key technical ingredients in seismic risk assessment. The derivation of fragility functions has been extensively studied in the past; however, large uncertainties still exist, mainly due to limited collaboration between the interdependent components involved in the course of fragility estimation. This research aims to develop a systematic Bayesian-based framework to estimate high-fidelity fragility functions by integrating monitoring, modeling, and hybrid simulation, with the final goal of improving the accuracy of seismic risk assessment to support both pre- and post-disaster decision-making. In particular, this research addresses the following five aspects of the problem: (1) monitoring with wireless smart sensor networks to facilitate efficient and accurate pre- and post-disaster data collection, (2) new modeling techniques including innovative system identification strategies and model updating to enable accurate structural modeling, (3) hybrid simulation as an advanced numerical-experimental simulation tool to generate highly realistic and accurate response data for structures subject to earthquakes, (4) Bayesian-updating as a systematic way of incorporating hybrid simulation data to generate composite fragility functions with higher fidelity, and 5) the implementation of an integrated fragility analysis approach as a part of a seismic risk assessment framework. This research not only delivers an extensible and scalable framework for high-fidelity fragility analysis and reliable seismic risk assessment, but also provides advances in wireless smart sensor networks, system identification, and pseudo-dynamic testing in civil engineering applications.

CONTENTS

Page

CHAPTER 1 INTRODUCTION 1

CHAPTER 2 BACKGROUND AND LITERATURE REVIEW 5

2.1 Strong Motion Instrumentation 5
2.2 Structural Health Monitoring 6
2.3 Wireless Smart Sensor Network 8
2.4 System Identification Using Seismic Measurements 11
2.5 Substructure Hybrid Simulation 13
2.6 Fragility Analysis 15
2.7 Summary 17

CHAPTER 3 EFFICIENT CAMPAIGN-TYPE SHM USING WSSN 18

3.1 A Post-sensing Time Synchronization Scheme 18
3.2 Multihop Bulk Data Transfer 24
3.3 Summary 27

CHAPTER 4 SYSTEM ID USING DECOUPLED OUTPUT SIGNALS 28

4.1 Decoupling of MIMO System 28
4.2 ARX-ERA Method for System Identification 36
4.3 Application to a Highway Overcrossing Bridge 38
4.4 Summary 45

CHAPTER 5 FRAGILITY FUNCTION UPDATING WITH HYBRID SIMULATION 46

5.1 Fragility Functions 46
5.2 General Concept of Bayesian Updating 46
5.3 Bayesian Updating of Fragility Functions 47
5.4 The Initial FE Model of the MRO Bridge 49
5.5 Model Calibration 51
5.6 Derivation of Analytical Fragilities (Case 1 and Case 2) 54
5.7 Bayesian Updating of Fragilities Using Hybrid Simulation (Case 3 and Case 4) 57
5.8 Risk Assessment 60
5.9 Summary 62

CHAPTER 6 SUBSTRUCTURE HYBRID SIMULATION WITH MSE 64

6.1 Formulations of Equations of Motion for MSE Problems 64
6.2 Comparison Between EOM-abs and EOM-rel 65
6.3 Effect of Ignoring Stiffness Change in EOM-rel 66
6.4 Implementation of Hybrid Simulation with MSE 71
6.5 Application to Santa-Monica Freeway Ramp Bridge 75
6.6 Summary 78

CHAPTER 7 NEES INTEGRATED SEISMIC RISK ASSESSMENT FRAMEWORK 79

7.1 Introduction 79

7.2 Architecture of NISRAF 79
7.3 NISRAF Components 80
7.4 Application Example 84
7.5 Potential, Limitations, and Challenges 90
7.6 Summary 90
CHAPTER 8 CONCLUSIONS AND FUTURE STUDIES 92
8.1 Conclusions 92
8.2 Future Studies 94
REFERENCES 97

INTRODUCTION

Throughout history, earthquakes have been one of the most devastating extreme natural events, causing untold casualties and economic loss. Over the last 12 years, according to the United States Geological Survey (USGS), earthquakes have caused more than 800,000 deaths worldwide (USGS, 2012), and the estimated total economic loss is over 1 trillion U.S. Dollars (Daniell and Vervaeck, 2011). In the United States, the Federal Emergency Management Agency has estimated the annual cost from earthquakes to the national building stock is over $5 billion on average (FEMA, 2008). While the occurrences of future earthquakes are not predictable, the damage and losses caused by potential earthquakes can be estimated. Therefore much effort has been devoted to seismic risk assessment to quantify the potential damage and losses due to future earthquakes, as well as the probability of these consequences. The result of seismic risk assessment provides the scientific basis for pre-disaster emergency and recovery planning and the formulation of risk reduction policies.

Hazard, inventory, and fragility definition are the three technical ingredients in seismic risk assessment. Seismic hazard definition seeks to characterize the ground motion during earthquakes, such as the intensity of ground motion, liquefaction, etc. The inventory (or exposure) is defined through a database containing information regarding the structures that are exposed to the seismic hazard. Fragility (or vulnerability) functions are essentially the sensitivity of the structures in the inventory to the seismic hazard. The reliability of seismic risk assessment relies on the quality of the models and data employed in these three components. Whereas the inventory component can be improved by existing methods of surveying assets, much remains to be done to improve hazard and fragility definition, the latter of which is the focus herein.

Based on the data source by which they are generated, fragility functions can be divided into four categories (Rossetto and Elnashai, 2003), including empirical fragility functions, judgmental fragility functions, analytical fragility functions, and composite fragility functions. Note that the last category was named hybrid fragility functions in Rossetto and Elnashai (2003). In order to avoid confusion with hybrid simulation which will be discussed later, composite fragility functions will be used hereinafter. Among these categories, analytical fragility functions have the widest application especially for the cases when no measured data is available. Although numerical analysis tends to have reduced bias compared with judgmental opinions derived from expert opinion, the accuracy of both the structure and hazard models dictates the reliability of the analytical fragility functions. Having an accurate structural model which closely represents the response of a real structure is essential to high fidelity fragility analysis. In most fragility simulations, however, either a very simplified numerical model is used or a complicated numerical model is used without calibration with real structures (Mosalam et al., 1997; Reinhorn et al., 2001; Pan et al., 2007). Such approaches introduce significant uncertainties to the derived analytical fragility functions due to the large uncertainties in the numerical models.

Seismic response monitoring systems instrumented on civil infrastructure provide a unique opportunity for better understanding of complex structural behavior resulting from earthquake excitation. The monitored structural and free field responses can be fed into system identification tools to extract key structural parameters, such as natural frequencies, mode shapes, and damping factors, etc., which can be used to refine the structural models. Parametric and nonparametric system identification methods have been extensively studied in many research fields. When earthquake records are considered, however, parametric methods generally produce better results due to the fact that earthquake records have short duration and are non-

stationary. Moreover, earthquake loadings are intrinsically multi-directional. Such loadings may lead to complex structural responses in which the contributions from various components are highly coupled. Identification of structural systems using multi-directional transient input and the induced complex responses is challenging.

For uninstrumented structures, campaign-type Structural Health Monitoring (SHM) can be performed to assist in timely pre- and post-earthquake structural condition assessment. Traditional SHM systems consist of a number of wired sensors distributed over the structure which are connected to a data acquisition system with cables. The installation of such wired SHM systems is often quite cumbersome and expensive, limiting their application for campaign monitoring. This point is especially true for large-scale structures (e.g., long-span bridges which require miles of cables for connecting sensors and days of work to deploy). SHM systems based on Wireless Sensor Networks (WSSNs) are low cost and easy to deploy and maintain, making them ideal for campaign monitoring. However, efficient data collection with wireless SHM systems remains a challenging task due to the large amount of data generated by typical SHM applications and the limited network bandwidth intrinsic to wireless networks.

While fragility functions may be calibrated based on available data, when more data becomes available, the analytical fragility functions should be updated. Moreover, combining difference sources of data is generally necessary for the reliable determination of fragility functions (Rossetto and Elnashai, 2003). The Bayesian statistical approach provides an effective way of combining additional data with existing fragility functions. Singhal and Kiremidjian (1998) applied the Bayesian approach to update the analytical fragility functions for reinforced concrete (RC) frame buildings with observational damage data from the Northridge earthquake in 1994. However, due to the limited amount of data, covering only six levels of ground motion intensity, the fragility functions could only be updated at discrete points. Koutsourelakis (2010) proposed a Bayesian framework for deriving fragility functions by estimating the posterior distributions of the mean and dispersion of the ground motion intensity. This method can also be used to update fragility functions. The advantage of this method, compared with the one proposed by Singhal and Kiremidjian (1998), is that the entire fragility function can be updated with limited data, as oppose to updating only at discrete points.

Substructure hybrid simulation, a pseudo-dynamic testing technique which combines numerical simulation and experimental testing, provides an effective and economic means of generating additional data to update or verify analytical fragility functions. Compared with observational data from earthquakes, which are often limited in both quantity and scope, experimental tests are conducted in a controlled manner, leading to a better distribution of data in terms of ground motion intensity. Substructure hybrid simulation is capable of testing large scale structures in an economic manner by modeling only the critical components of the structure experimentally. The Multi-Axial Full-Scale Sub-Structured Testing and Simulation facility (MUST-SIM) (Elnashai et al., 2004) at the University of Illinois, one of the fifteen equipment sites established in the George E. Brown Network for Earthquake Engineering Simulation (NEES), provides an unique environment for substructure hybrid simulation experiments. Various tests have been carried out which verified the efficacy of the MUST-SIM facility, including a geographically distributed hybrid simulation of a highway ramp bridge (Spencer et al., 2006), hybrid simulation tests for a steel moment resisting frame with semi-rigid connections (Mahmoud, 2011), and for RC shear walls (Hart et al., 2008).

Systematic integration of the above described interdependent research components, including monitoring (seismic response monitoring and structural health monitoring), modeling

(system identification based model updating), hybrid simulation, and Bayesian updating, into the fragility derivation process, can reduce the uncertainties of risk assessment results arising from engineering judgment. For instance, the nonlinear analytical or hybrid simulation models can be as realistic as possible by calibration with the system identification result from measured data. These nonlinear models and hybrid simulation models may be used to derive fragilities that are then fed into seismic loss assessment framework such as MAEviz and HAZUS.

The objective of this research is to develop an integrated approach to generate high-fidelity fragility functions for civil infrastructures by addressing some of the above challenges regarding monitoring, modeling, and hybrid simulation, and integrating them into a Bayesian framework. The final goal is to improve seismic risk assessment. In particular, this research addresses the following five aspects of the problem: (1) monitoring with wireless smart sensor networks to facilitate efficient and accurate pre- and post-disaster data collection, (2) new modeling techniques including innovative system identification strategies and model updating to enable accurate structural modeling, (3) hybrid simulation as an advanced numerical-experimental simulation tool to generate highly realistic and accurate response data for structures subject to earthquake loading, (4) Bayesian-updating as a systematic way of incorporating hybrid simulation data to generate composite fragility functions with higher fidelity, and 5) the implementation of an integrated fragility analysis approach as a part of a seismic risk assessment framework.

Chapter 2 provides background of this research and literature review of current status of structural health monitoring, system identification, hybrid simulation, and fragility analysis. Gaps of knowledge have been identified in each area, including time synchronization and efficient data collection with wireless smart sensors, system identification with multi-directional transient seismic measurement, substructure hybrid simulation under multiple-support excitation, and Bayesian updating of fragility functions using hybrid simulation data.

Chapter 3 presents an efficient data collection strategy for WSSNs tailored to SHM applications. Two critical issues have been addressed including time synchronization and network throughput. A post-sensing time synchronization protocol has been developed to improve the accuracy of time synchronization, especially for long-term data collection. This protocol also improves the efficiency of time synchronization. An efficient multi-hop data collection approach has been adopted and integrated into the framework. This new data collection strategy facilitates efficient pre- and post-disaster condition assessment for civil infrastructures.

Chapter 4 describes a new system identification method for multiple-input, multiple-output (MIMO) systems based on decoupling. This method converts a MIMO system into a number of single-input, multiple-output (SIMO) systems by identifying the contribution of a specific input to a desired output, leading to simplified problems which can potentially generate more accurate result. In addition, an automatic system identification strategy combining the Auto Regressive with eXogenous input method and the Eigensystem Realization Algorithm (ARX-ERA) has been proposed to identify the decoupled systems. The method has been validated through an application to a highway overcrossing bridge for which seismic measurements are available.

Chapter 5 presents a two-stage approach to derive high-fidelity fragility functions. The first stage involves an effective multi-step model calibration method and the generation of analytical fragility functions with the calibrated model. In the second stage, Bayesian updating is adopted to systematically incorporate hybrid simulation data to improve the numerical fragility

functions. The effectiveness of this approach has been demonstrated by deriving composite fragility functions for the highway overcrossing bridge considered in Chapter 4.

Chapter 6 addresses the issue of conducting substructure hybrid simulation with multiple-support excitation (MSE). The performance of two different formulations of the equations of motion has been investigated for hybrid simulation with MSE. The investigation led to the conclusion that the formulation in relative coordinates, which is widely adopted in conventional numerical simulation, can cause large error when the experimental substructures experience severe nonlinearity. Hence, the formulation in absolute coordinate was then implemented in UI-SimCor, the hybrid simulation platform developed at UIUC, allowing accommodating of a wider range of earthquake excitation scenarios.

Chapter 7 describes the developed NEES Integrated Seismic Risk Assessment Framework (NISRAF). In addition to the high-fidelity fragility analysis component developed in previous chapters, this framework also incorporates a critical component for high-fidelity hazard characterization. A Graphical User Interface (GUI) has been developed to facilitate ease of use.

Chapter 8 provides a summary of the research presented in this report and discusses a number of future research directions on the key areas explored in this report.

BACKGROUND AND LITERATURE REVIEW

This chapter provides background and a review of the literature for the related fields of the proposed research in this repot, including structural health monitoring, substructure hybrid simulation, and fragility analysis. The literature review begins with the strong motion instrumentation, a traditional source of response data for design verification and model calibration. Then, the recent advances of structural health monitoring (SHM) is presented, followed by a brief introduction of wireless smart sensor networks (WSSN) with the emphasis on the challenges for time synchronization and data transfer in SHM applications. Next, system identification methods using seismic measurement are discussed, which are critical to improving the accuracy of structural models. The background of substructure hybrid simulation is then introduced. Finally, fragility analysis is briefly introduced and previous research efforts on Bayesian updating of fragility functions are presented. The goal of this chapter is to identify the gaps in knowledge with respect to these interdependent components that limit the generation of high-fidelity fragility functions for seismic risk assessment.

2.1 Strong Motion Instrumentation

Ever since the first significant strong motion record captured during the Long Beach earthquake of 1933, seismologists and earthquake engineers have showed great interest in monitoring the response of the free field and structures during earthquakes, in recognition of the extreme importance of understanding of strong ground motion to earthquake safety. The number of strong motion instruments has been increasing, with some notable expansions being triggered by large earthquakes such as the 1976 Great Tangshan earthquake in China and the 1995 Hyogoken-Nambu (Kobe) earthquake in Japan (Iwan, 2008). In the United States, the largest two strong motion instrumentation programs are the Advanced National Seismic System (ANSS) managed by the United States Geological Survey (USGS) and the California Strong Motion Instrumentation Program (CSMIP) managed by the California Geological Survey (CGS).

The ANSS is a national wide network of earthquake sensor systems which aims to deploy over 7000 sensors in all areas of the country subject to earthquake hazards, with four basic goals including: 1) establish and maintain an advanced infrastructure for seismic monitoring throughout the United States; 2) continuously monitor earthquakes and other seismic disturbances throughout the United States; 3) thoroughly measure strong earthquake shaking at ground sites and in buildings and critical structures; and 4) automatically broadcast information when a significant earthquake occurs, for immediate assessment of its impact (USGS, 1999). As a national seismic system, the ANSS consists of three levels of monitoring strategies including a national seismic monitoring system with 100 seismographs to form a national backbone network, a regional seismic monitoring system with a total of 1,000 modern seismograph stations to monitor seismic activities on a regional or local scale, and an urban seismic monitoring system which is composed of 3,000 free-field strong-motion seismographs and 3,000 strong-motion instruments installed on buildings and structures deployed in 26 at-risk urban areas (USGS, 1999).

The CSMIP is a network for monitoring seismic ground motion, as well as structure responses under seismic excitations, in the state of California. This program has installed more than 900 stations, including 650 ground-response stations, 170 buildings, 20 dams and 60 bridges. Since the establishment in 1972, CSMIP has recorded many strong motions during large earthquakes including the 1979 Imperial Valley earthquake and the 1994 Northridge

earthquake. The recorded free-field motion and structural response data during large earthquakes has helped engineers better understand the behavior and the resulting damage of building structures under strong ground motions, revealed the ground shaking characteristics close to the fault, led to improved formulas in the Uniform Building Code for calculating building fundamental vibration period, and confirmed the effectiveness of modern concept in earthquake protection design such as base isolation (Huang and Shakal, 2001).

To ensure that the funds for strong motion instrumentation are spent in a cost-effective manner, a formal and nation-level process is used to rank and select engineered civil systems for ANSS response monitoring (ANSS, 2005). The selection of structures for instrumentation is based on both the structural parameters, such as structural type, construction materials, dimension, etc., and the site-related parameters such as the location which defines the severity of shaking based on the closeness to the faults with the area of consideration (Çelebi, 2004). The selection criteria of the CSMIP are similar to the ANSS. Buildings are selected for instrumentation based on recommendations of an advisory committee. The plan is to cover all representative building types (e.g., frames, shear walls, and base isolation), and various construction techniques and materials (steel, concrete, masonry and wood). Also, buildings located at locations where significant ground shaking is likely to occur are ranked high in the instrumentation plan (Huang and Shakal, 2001).

The two strong motion instrumentation networks described above cover a large number of structures; however, compared with the huge inventory of the infrastructure in the United States, the number of instrumented structures is still limited. As another important source of response data for design verification and model updating, structural health monitoring (SHM) has received considerable attention both in theory and in practice over the last few decades, as will be introduced in the next section.

2.2 Structural Health Monitoring

Structural health monitoring (SHM) is an emerging technology that encompasses a broad range of methods and applications with the goal of informing the current condition of a structure in order to assist structural maintenance. In civil engineering field, SHM is employed in practice to address various issues for civil infrastructures, including (Spencer et al., 2007):

1) to validate the structural design and characterize performance (e.g., develop database)
2) to characterize loads in situ
3) to assist with building/bridge maintenance
4) to monitor and control the construction process
5) to assist with emergency response efforts, including building evacuation and traffic control
6) and to detect and localize damage before it becomes critical

Visual inspection has been one of the major approaches in practice for the maintenance of structural facilities. For example, the Federal Highway Administration (FHWA) requires all bridges be inspected every two years. Although visual inspection still remains one of the most important maintenance method for civil infrastructure, it is time consuming, labor intensive, cost inefficient and prone to error. One tragic example is the collapse of the I-35W highway bridge over Mississippi River in Minnesota in 2007 killing 13 people and injuring 145 even though it passed a visual inspection a year prior to failure. Moreover, visual inspection is not able to provide data to support design validation and the characterization of loads in situ, etc. Structural Health Monitoring aims to assess the structural integrity using sensing technologies and signal

processing approaches, enabling a long-term, continuous monitoring paradigm which can potentially provide a more reliable and economic way of damage detection and maintenance of civil infrastructure.

Depending on the duration and the purpose of monitoring effort, Structural Health Monitoring system can generally be classified into two categories, i.e. short-term, or campaign-type SHM systems and long-term SHM systems. Campaign SHM systems are deployed for a short amount of time ranging from perhaps a few hours to a few days, in order to assess the current integrity of structures such as load-carrying capacity. Campaign SHM systems are widely applied in assessment of retrofitted structures, post-disaster condition assessment, and design optimization of long-term SHM systems before permanent deployment, etc. Brownjohn et al. (2003) carried out campaign SHM for a highway bridge in Singapore before and after strengthening of the bridge through dynamic testing and model updating. Brownjohn et al. (1994) also conducted several monitoring campaigns to the Humber Bridge in the UK with 63 sensors deployed on the bridge which include wind sensors, LVDTs, and accelerometers. The measured data was used to validate mathematical modeling of the bridge response under wind and to estimate the relationships between the loading and response parameters. Antonacci et al. (2012) describes a monitoring effort for a church structure in Italy to assess its dynamic properties after the 2009 L'Aquila earthquake using wireless smart sensors. Jang et al. (2012) estimated the corrosion of a historic truss steel bridge by using model updating with data collected through campaign-type SHM experiments. On the other hand, long-term SHM systems are generally in operation for a few months or years, aiming for monitoring long-term deterioration, fatigue damage of structures, and so on. A real-time SHM system was implemented for long-term monitoring of the cable-stayed Bill Emerson Memorial Bridge in Cape Girardeau, Missouri (Çelebi, 2004). The system comprises a total of 84 channels of accelerometers deployed on the superstructure, pier foundations and free field of the bridge. The SHM system was operated in a continuous manner so that both ambient vibration and seismic data were captured which were used for assessing the performance of the bridge and checking design parameters. Many long-span bridges in Hong Kong are installed with long-term SHM systems, such as the Tsing Ma Bridge, the Kap Shui Mun Bridge, the Ting Kau Bridge, and the Stonecutters Bridge (Wong, 2004; Wong and Ni, 2009; Ni, 2010). Xia et al. (2005) performed both campaign and long-term health monitoring of a single-span skew highway bridge in which modal property identification was the main goal of the campaign monitoring and fatigue damage assessment, extreme stress analysis and temperature effect on displacement were considered in the long-term monitoring.

One drawback of wired SHM systems is their high cost due to the cables that are needed to connect the sensors distributed over the structure to the central base station. Long span bridges require miles of cables to connect sensors which result in high cost of instrumentation hardware and installation. For example, the instrumentation of the SHM system on the Humber Bridge which has 63 sensors installed requires over 32 km of cabling (Brownjohn, 2007). The cost of installing over 350 sensing channels on the Tsing Ma Bridge in Hong Kong is estimated to be more than $8 million, resulting in about $23,000 per sensor channel (Lynch and Loh, 2006; Farrar, 2001). The total cost of the monitoring system on the Bill Emerson Memorial Bridge in Missouri is approximately $1.3 million for 84 channels of accelerometers (~$15,000 per channel) (Çelebi, 2004). High cost of wired SHM system due to onerous and expensive cabling work prohibits the number of sensors on structures and hence limits the application and success of SHM on large-scale civil infrastructures.

The emerging technology of wireless smart sensors, which will be discussed in the following section, has the potential to overcome the drawbacks of wired SHM systems.

2.3 Wireless Smart Sensor Network

2.3.1 Wireless smart sensors

Wireless smart sensors (WSS) are devices which have sensor, microprocessor, radio frequency (RF) transceiver, memory and power source integrated into one small size unit and are therefore featured by their capabilities of sensing, computation, data transmission and storage, all achieved by one single device. The wireless communication capability removes the necessity of cabling work in SHM systems when wireless sensors are used in place of wired ones. Therefore the cost of SHM systems is significantly reduced. In addition, with the rapid advances in Micro-electromechanical systems (MEMS), the mass production of MEMS devices makes the cost of wireless smart sensor decrease dramatically. The computation capability enabled by the on-board microprocessor allows each sensor node in the network to autonomously interrogate its data and interact with other sensor nodes when necessary, offering network scalability through decentralized operation of sensor networks. As envisioned by Spencer et al. (2004), smart sensors have the potential to change fundamentally the way civil infrastructure systems are monitored, controlled and maintained.

To date, various smart sensors have been developed in both academia and industry. Straser and Kiremidjian (1998) developed the first wireless smart sensor system, called the wireless modular monitoring system (WiMMS), for civil engineering application. Subsequently, a number of smart sensors were developed by individual research groups around the world, such as Bennett et al. (1999), Lynch et al. (2001, 2002), Mitchell et al. (2002), Kottapalli et al. (2003), Aoki et al. (2003) and Basheer et al. (2003), etc. More details can be found in a comprehensive review of wireless smart sensors and sensor networks applied in structural health monitoring by Lynch and Loh (2006). While these academic smart sensors have made substantial impact on the research field, these systems are of a proprietary nature so their availability to other users is limited. In the meantime, a number of commercial smart sensors were developed and some of them were found quite promising for SHM applications. Among them, the Mica motes developed by the University of California at Berkeley which were subsequently commercialized by Crossbow Technology (www.xbow.com) received significant attention because of their open hardware and software design. Later, the Imote (Kling, 2003) and especially the second generation Imote2 (Kling et al., 2005; Adler et al., 2005) designed by Intel (now available from MEMSIC Inc, www.memsic.com) provide much higher processor speed, larger bus size and memory than the Mica motes, making them better platform to meet the demanding computational needs typical in data intensive SHM applications.

Many smart sensor platforms, such as the imote2 and Mica2, adopted the stackable modular design which allows different types of daughter board to be attached. Therefore recent years much effort has been devoted to the development of various types of sensor boards to facilitate different measurements in SHM systems, such as strain, acceleration, displacement, etc. Nagayama et al. (2004) developed a strain sensor board to interface with the Mica2 sensor platform. Rice and Spencer (2008) developed an accelerator board for the Imote2 sensor platform. Jo et al. (2010, 2012) developed a high-sensitivity accelerator board and a high-precision strain sensor board, both for the Imote2 platform. The various types of sensor boards, in conjunction with the smart sensor platform, are the foundation of building a hybrid Wireless Smart Sensor Network (WSSN) for structural health monitoring (Jo et al., 2011).

2.3.2 The ISHMP Services Toolsuite

Software is another important component that enables a functioning wireless SHM system. Software for WSS includes the operating system, middleware services and application-level services. TinyOS (http://www.tinyos.net) is the first operating system designed specifically for WSSNs. It employs an event-driven architecture for conducting concurrency-intensive operations on resource-restrained (processing power, memory, and energy) devices such as the Berkeley Mote and the Imote2 in a power-efficient manner. TinyOS is non-blocking and uses a single stack. Tasks and event handlers are the two supported types of executions. Tasks are executed in a first in, first out (FIFO) manner based on the order they are posted and run to completion; therefore they are mainly used for performing long-running computations whose results are not needed immediately. Events handlers are executed in response to a signaled event and handle concurrent data flows. Tasks do not preempt each other, but a task can be preempted by a hardware event handler. Because of the above concurrency model, TinyOS does not support real-time operation and priority-based programming, posing challenges for developing some SHM applications with WSSNs, such as time synchronization, as will be discussed in detail in later sections.

Middleware services and application-level services are both essential components in the software for WSSN-based SHM systems. Middleware services aim to address many intrinsic issues in WSSNs, such as time synchronization, routing and reliable communication (Nagayama and Spencer, 2007), while application-level services build routines for specific SHM algorithms and applications using the low level components in the operating system and the middleware services, such as conducting sensing at remote nodes and then retrieving the collected data back to the based station wirelessly (*RemoteSensing*), processing the collected data within the network in a decentralized manner and estimating correlation functions in each sensor cluster (*DecentralizedDataAggregration*), and performing scheduled network-wise tasks autonomously and continuously (*AutoMonitor*). These middleware services and application-level services have been developed by the Illinois Structural Health Monitoring Project (ISHMP) as part of the ISHMP services Toolsuite, which will introduced in detail below.

The ISHMP Services Toolsuite (http://shm.cs.uiuc.edu/software.html) is a collection of open source middleware and application-level services designed specifically for implementing various SHM applications using Imote2 wireless smart sensors. The toolsuite is written in NesC (Gay et al., 2003), the same program language that the TinyOS is written in, and is designed based on the concept of Service-oriented architecture (SOA), which divides the software into smaller, more manageable components such that the concerns in application development are separated (Rice and Spencer, 2009). The toolsuite provides three types of services: (1) foundation services, (2) application services, and (3) tools and utilities. The Foundation services address the basic needs to fulfill a functioning wireless sensing network, such as time synchronization, sensing, reliable communication and multi-hop routing, etc. The application services provide building blocks for SHM applications, such as Synchronized Sensing, Correlation Function Estimation, Stochastic Damage Locating Vector (SDLV) method, Eigensystem Realization Algorithm (ERA), etc. Tools and Utilities contain the highest-level applications to operate or test the sensor network, such as the *RemoteSensing*, *DecentralizedDataAggregration* and *AutoMonitor* mentioned before, as well as some test applications. More detailed information about each application can be found in Rice and Spencer (2009), Sim and Spencer (2009), and Mechitov (2011).

2.3.3 Synchronized sensing

Measured data from individual sensor nodes in a wireless sensor network needs to be synchronized for SHM applications, especially when the data is used for identifying the structural mode shapes (Nagayama and Spencer, 2007). The local clocks of wireless smart sensors run independently and therefore do not produce time stamps which fit in a common global timeframe if these clocks are not synchronized. In addition, synchronized clocks do not guarantee synchronized data, because of (1) the uncertainties in the start-up time of sensing due to the randomness of the processing time in the sensor board driver, (2) the difference of the sampling frequencies among sensor nodes due to the low quality of crystals, and (3) the fluctuation of sampling frequency overtime for each individual sensor node due to jitter. Therefore, the realization of synchronized sensing in SHM has two components: one is synchronization of clocks, and the other is synchronization of data (Nagayama and Spencer, 2007; Mechitov, 2011).

Time synchronization of clocks in a distributed network has been widely investigated in the past decades. The Network Time Synchronization (NTP) protocol (Mills, 2004) is mostly widely used in the internet domain and is only suitable for low precision applications with WSSN. The three major time synchronization protocols that are being used in WSSN are Reference Broadcast Synchronization (RBS) (Elson et al., 2003), Time-sync Protocol for Sensor Networks (TPSN) (Ganeriwal et al., 2003), and Flooding Time Synchronization Protocol (FTSP) (Maroti et al., 2004). The FTSP has several advantages over the other two protocols. For example, it utilizes flooding to compensate packet loss and node failure and to accommodate dynamic topology change. FTSP also compensates clock drift using linear regression. Mechitov et al. (2004) implemented an adapted version of FTSP on the Mica2 mote and the time synchronization service can maintain better than 1 ms synchronization for minutes.

To achieve precise synchronization in the collected data among sensor nodes, Nagayama et al. (2007) and Mechitov (2011) proposed a resampling approach which can address the three issues mentioned previously at the same time. Resampling with a rational factor is achieved by a combination of upsampling, filtering and decimation. Polyphase implementation is employed with a Finite Impulse Response (FIR) filter to reduce the computation cost. To avoid too large upsampling factor, linear interpolation is introduced in the downsampling phase with a non-integer factor while a reasonable integer number of upsampling factor can be selected. The initial delay is also considered in the resampling process. This resampling approach is implemented in the ISHMP Services Toolsuite for Imote2. From a laboratorial test on a truss structure, the synchronization error of the measured signals is approximately 30 μs (Nagayama and Spencer, 2007).

However, current time synchronization approach implemented in the ISHMP Services Toolsuite has a number of limitations. First of all, the approach estimates linear clock drift rate before sensing by broadcasting beacon signals in the network, therefore it delays the start of sensing in order to collect adequate number of data points for regression analysis. In addition, since the clock drift rate was estimated before sensing, it does not necessarily provide an accurate description of the clock drift during sensing due to possible nonlinearity caused by temperature variation. A different strategy is needed to improve both the efficiency and the accuracy of time synchronization in SHM applications.

2.3.4 Multi-hop communication

Multi-hop communication protocols in WSSN enable communication between sensors that are out of the range of direct communication via intermediate sensor nodes. They can generally be split into two phases, including (1) multi-hop route discovery between the source and destination nodes and (2) data transfer using the established routes. In practical SHM applications, multi-hop communication is often desirable due to poor radio communication in the outdoor environment and long distance between sensor nodes because of the large scale of civil infrastructures such as bridges, tunnels and high-rise buildings. While many multi-hop communication protocols have been proposed in the past for ad hoc applications, such as the Ad-hoc On-demand Distance Vector routing (AODV) (Perkins and Royer, 1999), the Dynamic Source Routing (DSR) (Johnson et al., 2007), Temporally Ordered Routing Algorithm (TORA) (Park and Corson, 1997), etc., a detailed review of multi-hop routing protocols can be found in Nagayama et al. (2010), none of them is readily applicable to SHM systems due to the specific requirements and characteristics of SHM applications. Nagayama et al. (2010) summarized these requirements and characteristics and proposed two complimentary reliable multi-hop communication protocols for SHM, including a general purpose multi-hop (GPMH) protocol enabling any-to-any communication for reliable data transfer, which is adapted from the original AODV protocol, and a single-sink multi-hop (SSMH) communication protocol designed specifically for the case which has only a single sink node.

Current ISHMP Services Toolsuite has the GPMH implemented. However, GPMH retrieves data from the sensor nodes in a sequential manner in order to avoid packet collisions, leading to very long data retrieval time especially when the number of hops is large. Integrating the SSMH into the Toolsuite will facilitate high-efficiency data collection in pre- and post-disaster campaign monitoring. In order to support the core functions of the SSMH in the Toolsuite, including the multi-hop routing and data forwarding, the current ways of sending commands, waking up and resetting networks should be replaced by flooding based methods.

2.4 System Identification Using Seismic Measurements

One of the main purposes of collecting vibration data from structures and free field using strong motion instrumentation and structural health monitoring systems is to do system identification. System identification is a process of building a mathematical model of a dynamic system based on measured data. In civil engineering applications, system identification has served as an essential tool which delivers realistic structural models to facilitate a wide range of practical problems such as design verification, structural health monitoring, damage detection, structural control, and others. Various algorithms have been developed in the past decades to identify linear models of engineering structures. These methods can generally be classified into two categories, namely nonparametric and parametric methods, depending on whether a parameterized model of the underlying system is assumed. Nonparametric methods are often frequency domain approaches such as the Peaking-Picking (PP) method (Bendat and Piersol, 1993; Felber, 1993) and the Frequency Domain Decomposition (FDD) method (Brincker et al., 2001). Parametric methods are usually time domain approaches such as the Eigensystem Realization Algorithm (ERA) (Juang and Pappa, 1985), Stochastic Subspace Identification (SSI) (Overschee and Moor, 1996), Prediction Error Method (PEM) (Ljung, 1999), etc. Note that although ERA and SSI are parametric methods, their inputs are sometimes derived through nonparametric methods.

Non-parametric system identification methods are generally more efficient, but often less accurate, than parametric system identification methods. Although averaging can help smooth

the data and reduce noise, relatively larger amount of data points are generally needed and the signals need to be stationary. Seismic records are non-stationary transient signals with relatively short duration; therefore, parametric methods are more often applied than non-parametric methods to identify the modal properties of civil infrastructures. A method based on the Eigensystem Realization Algorithm (ERA) and the Observer/Kalman filter identification (OKID) approach was applied to the Vincent-Thomas cable suspension bridge with recorded input-output data during the Whittier and the Northridge earthquake (Lus and Longman, 1999). Another approach based on System Realization using Information Matrix (SRIM) was proposed and applied to three long-span cable-supported bridges in Japan using seismic records (Siringoringo and Fujino, 2006). Subspace-based approaches were applied to a five-story steel frame using simulated earthquake responses from shaking table tests (Huang and Lin, 2001) and to a highway overpass bridge (Anderson et al., 2007).

Prediction Error Methods have also been widely applied in system identification with seismic measurements. Beck and Jennings (1980) tried to estimate the optimal parameters of linear structural models by minimizing a measure-of-fit between the structural output and model output. The method was applied to the strong-motion records obtained in a 42-storey steel-frame structure during the 1971 San Fernando earthquake in California. Similar approaches within the framework of output-error methods were applied to a highway overcrossing bridge (Werner et al., 1987), base-isolated bridges (Chaudhary et al., 2000) and concrete arch dam (Alves and Hall, 2006). Smyth et al. (2003) applied an efficient least-squares-based time-domain identification procedure to the Vincent Thomas suspension bridge using earthquake records. The above parametric methods use the equations of motion as the underlying model and as the basis for formulating the error function. On the other hand, some general classes of time series models, such as the Autoregressive and moving-average model with exogenous inputs (ARMAX) and the Autoregressive model with exogenous inputs (ARX) have been reported for system identification with seismic records. Loh and Lin (1996) applied both the ARX and the ARMAX model to estimate the modal frequencies, damping ratios and modal contributions of a seven-story building using seismic data. By introducing a forgetting factor, these models are able to detect time-varying modal parameters. Loh and Wu (2000) applied the ARX model to an arch dam structure using seismic response data. Arici and Mosalam (2003) applied the same method to seven instrumented bridges in California.

Due to unavoidable noise in the measured data, the order of the ARX model is usually set much higher than twice the number of poles to represent the measured response, introducing noise modes in the identification result. These extra modes are a common problem in many parametric system identification methods. Various approaches have been proposed to filter out these noise modes. Among these are the positive damping rule and the stabilization diagram methods. Such efforts have been limited in the applications of the ARX method. Saito and Beck (2010) proposed a Bayesian based approach to select the structural modes from the identified ARX model. In their approach, the probable modes are firstly determined by the first earthquake, and the posterior probability distribution function (PDF) is formed. In the result of the next earthquake, the mode which maximizes the posterior PDF is considered as the corresponding structural mode. This method, however, is designed for the case when multiple records are available, and is not suitable for a single identification result. Ji et al. (2011) used damping ratio and Modal Phase Collinearity (MPC) combined with the stabilization diagram to select structural modes from the identified ARX model. However, the MPC has limited sensitivity to noise level,

and therefore the noise modes may not be distinguished by this single rule. The combined usage of MPC and EMAC should be investigated.

Another challenge of system identification using seismic measurement lies in the complexity of the input-output relationship. Civil structures typically have numerous degrees-of-freedom (DOFs) and large physical dimensions. When subjected to complex loadings such as earthquake excitations, they exhibit complex responses. For example, earthquake excitations are intrinsically multi-dimensional, creating inputs in different directions which are applied to the structural system simultaneously. Moreover, the structures may respond to the earthquake excitations in a complex way such that the effects of these inputs on the structural responses are coupled, i.e., the measured response contains the contributions from more than one input. System identification of these structures is therefore treated as a Multiple-Input, Multiple-Output (MIMO) problem if the inputs and the coupled output measurements are to be used.

Compared with Single-Input, Multiple-Output (SIMO) system identification problems, MIMO problems are more challenging, regardless of the use of parametric or nonparametric methods. In the case of parametric methods, the existence of multiple inputs implies the estimation of more parameters. For nonparametric methods, estimating impulse or frequency response functions requires the inversion of the input correlation or cross power spectrum matrices. If the multiple inputs are correlated and have restricted bandwidths, which is often the case for earthquake excitations, these matrices may be ill-conditioned and the inversions are prone to error. Therefore, to reduce computational complexity and improve the accuracy of results, decoupling a MIMO problem into a number of SIMO problems is desirable.

The key issue in decoupling a MIMO problem for system identification is to isolate the contribution of each input to a specific output. In regression analysis, this idea has also been used to select the optimal set of regressors (Draper and Smith, 1998; Miller, 2003; Chen et al., 1989; Chen et al., 1991; Wei et al., 2004; Lind and Ljung, 2008). For example, to select the centers (regressors) for the Radial Basis Function (RBF) neural networks, Chen et al. (1991) proposed an Orthogonal Least Squares (OLS) method to decouple the desired output into a linear combination of a set of orthogonal basis vectors. This method allows calculation of the individual contributions of the output energy from each basis vector. However, the drawback of this approach is that the coefficients of the linear combination are obtained from a least squares solution, introducing error in the decoupled result. A variation of the OLS method was then proposed by Westwick et al. (2006) based on QR factorization. In the latter approach, the factorization is performed for the matrix formed by not only the inputs, but also the desired output. The individual contribution to the output from each input is thus obtained directly after the factorization. Nonetheless, applications of these methods have been focused on identifying the relative contribution of an individual input to the output energy, by which the less significant inputs can be removed from regression analysis or system identification. In contrast, the approach advocated in this research is to decouple the outputs and then perform system identification directly. In such a case, the accuracy of the decoupled outputs is critical to the subsequent system identification result based on the decoupled outputs.

2.5 Substructure Hybrid Simulation

Hybrid simulation is a laboratory testing method of structures under dynamic loads. It is also called Pseudo-Dynamic (PsD) testing method in which the structural displacements under dynamic loading such as earthquakes are calculated through time-stepping integration of the equations of motion (EOM) and are then applied quasi-statically to the experimental specimens

(Mahin and Shing, 1985; Takanashi and Nakashima, 1987). The restoring forces measured from the experimental specimens are combined with the numerical terms of inertial and damping forces in the next step of integration to obtain the next target structural displacements. The advantage of hybrid simulation is that the displacements are applied in an extended time-scale such that the hydraulic actuators do not have to respond quickly, making the testing of large-scale structures possible. In addition, the extended time-scale for each loading step allows a careful examination of the specimens along the testing (Williams and Blakeborough, 2001). Substructure hybrid simulation is when hybrid simulation is combined with substructuring technique, and is even more efficient in that only the critical structural components which are likely to have nonlinear response or damage are needed to be tested experimentally, while the other parts of the structure can be modeled numerically (Pegon and Pinto, 2000).

Time-stepping integration is an essential part of hybrid simulation. Both explicit and implicit methods can be applied to hybrid simulations. Explicit methods, such as the Central Difference Method (CDM) (Shing and Mahin. 1985), calculate the target displacements based only on the results of the previous time step, therefore the displacements can be readily applied to the testing specimens. However, explicit methods are only conditionally stable and so may require a very small time step especially for very stiff structures. On the other hand, implicit methods are unconditionally stable, but the calculation of the target displacements requires the knowledge of the current time step. Therefore, the application of implicit methods involves an iterative process which achieves the target displacement through subcycling at each time step (Shing and Manivannan, 1990; Shing et al., 1991). This process may introduce problems for testing in the nonlinear range because the overshooting of hydraulic actuators can affect the properties of the specimens. Nakashima et al. (1990) developed the operator-splitting (OS) method, which is non-iterative, linearly implicit and nonlinearly explicit. Combescure & Pegon (1997) combines the α-modified Newmark scheme with the OS method, in order to damp numerically the undesired spurious oscillations.

Other variations of hybrid simulations have been developed in recognition of the drawbacks of pseudodynamic testing. In conventional pseudodynamic testing, displacement increments are applied to specimens quasi-statically through a ramp-hold procedure. Measurements are then taken during the hold period. Load relaxation may occur if the specimen is yielding, resulting in significant load reduction. To overcome this problem, continuous pseudodynamic testing method is therefore developed in which the hydraulic actuators move continuously during the test (Casciati and Magonette, 1990; Pinto et al. 2004; Mosqueda et al., 2004). Another drawback of pseudodynamic testing is that it cannot test rate-dependent behavior of the specimen. Therefore, real-time hybrid simulation methods are developed and have received significant attention in recent years (Nakashima et al., 1992; Darby, 1999; Wu et al., 2007; Carrion et al., 2009). Geographically-distributed hybrid simulation has also been attempted (Watanabe et al., 2001; Tsai et al., 2003; Mosqueda et al., 2004; Spencer et al., 2004).

Most of the hybrid simulation tests mentioned in previous paragraphs considers uniform ground excitation. Hybrid simulation considering multiple-support excitation (MSE), or asynchronous excitation, has been limited. Pegon & Pinto (2000) and Pinto et al. (2004) reported a continuous pseudodynamic testing with nonlinear substructuring on a large-scale model of an existing bridge. The test considers both synchronous and asynchronous ground excitation input. However, there is still a lack of thorough investigation on the selection of the formulation of equations of motion in the case of MSE. In addition, adding the MSE capability to the current hybrid simulation framework developed at the University of Illinois, the UI-SimCor (Kwon,

2008), will allow the accommodation of a wider range of earthquake excitation scenarios under the fully modularly-designed framework.

2.6 Fragility Analysis

Fragility functions, commonly expressed as the conditional probability of reaching or exceeding a certain damage limit state under a given ground motion intensity, are one of the driving technical ingredients in regional risk and loss estimations (Elnashai, 2003; Pan et al., 2007), which are essential for the purpose of disaster planning and formulating risk reduction policies. Based on the data source by which they are generated, fragility functions are generally divided into four categories (Rossetto and Elnashai, 2003), including empirical fragility functions, judgmental or expert-based fragility functions, analytical fragility functions, and composite fragility functions. Among them, empirical fragility functions are derived based on data from post-earthquake surveys and are therefore considered the most realistic; however, they suffer from the limitation of applicability due to the nature of its data source (e.g., scarcity of damaging earthquakes, low level of refinement of damage and structure classifications, judgmental and subjective nature of damage rating, etc.). Judgmental fragility functions are purely based on expert opinions and are therefore associated with large uncertainties. Examples of judgmental fragility functions include the curves proposed in ATC-13 (Rojahn and Sharpe, 1985) and ATC-40 (Applied Technology Council, 1996). Analytical fragility functions have the widest application especially for the cases when no actual data is available. Although numerical analysis tends to have reduced bias compared with expert opinion, the accuracy of both the structure and hazard models dictates the accuracy of the analytical fragility functions. Composite fragility functions combine data from different sources, such as combining the analytical or judgmental fragility functions with observational data from either surveys or experiments. For example, the Bayesian approach has been applied to update the analytical fragility functions using additional survey data (Singhal and Kiremidjian, 1998).

Analytical fragility functions are often formulated using a two-parameter log-normal distribution functions (Shinozuka et al., 2000; Nielson, 2005) with the following mathematical form:

$$P_f = P\left(\frac{S_d}{S_c} \geq 1\right) = \Phi\left[\frac{\ln\left(S_d / S_c\right)}{\sqrt{\beta_d^2 + \beta_c^2}}\right] \tag{2.1}$$

where Φ is the Cumulative Distribution Function (CDF) of the standard normal distribution; S_d and S_c are the structural demand and the structural capacity, respectively, and β_d and β_c are the associated dispersions. Apparently, the capacity and demand models are the two essential elements in analytical fragility functions. There have been a number of different methodologies to model the capacity and demand. As summarized in Nielson (2005), elastic spectral analysis (Yu et al., 1991; Jernigan and Hwang, 2002), nonlinear static analysis or capacity spectrum method (CSM) (Dutta, 1999; Mander and Basoz, 1999; Shinozuka et al., 2000; Rossetto and Elnashai, 2004), and nonlinear time history analysis (Cornell et al., 2002; Mackie and Stojadinovic, 2001; Hwang et al., 2000; Pan et al., 2007) are the three main methods to generate analytical fragility functions. Among them, the nonlinear time history analysis is the most reliable methods, although it tends to be the mostly computationally expensive method (Shinozuka et al., 2000).

The generation of analytical fragility functions based on nonlinear time history analysis is composed of six steps. In the first step, a suite of seismic ground motions is generated for the nonlinear time history analysis. These ground motions can either be selected from the historic seismic ground motion database or be synthetically generated. For both procedures, the seismic characteristics and local site condition of the considered geographic location need to be taken into account to have realistic representation in the selected/generated ground motions. Also, appropriate uncertainties need to be considered to have reasonable uncertainties in the demand model. In the second step, the parameterized structural model is built and the most sensitive structural parameters are considered random variables and are used to generate a number of nominally identical but statistically different structural models. Different sampling techniques, such as the Latin Hypercube sampling approach (Wyss and Jorgensen, 1998; Ayyub and Lai, 1989), can be applied to generate a set of combinations of the structural parameters, such that the highest accuracy of random distribution is achieved by a reduced number of samples. In the third step, these models are then paired with the suite of ground motions from step 1 and nonlinear time history analyses are then performed for each pair of structural model and ground motion. In the fourth step, the probabilistic capacity model is generated. Damage index is selected and different levels of damage limit states are defined, which can be done by pushover analysis numerically or experimentally. Appropriate uncertainties are assigned to each limit state according to experimental testing or engineering judgment. The seismic demand values from the nonlinear time history analyses are then identified from the maximum values of the damage index that occurred in the response time histories. In the fifth step, regression analyses are applied to the seismic demand values to obtain the probabilistic demand model. Regression analyses can also be applied to the ratio between the structural demand and capacity (Pan, 2007). In the final step, the probabilistic demand model and the probabilities capacity model are combined to generate the analytical fragility functions as shown in Eq. (2-1).

The analytical fragility functions can be updated in a continuous manner when additional survey or experimental data becomes available. The Bayesian statistical approach enables an effective way of combining additional data with existing fragility functions. Singhal and Kiremidjian (1998) applied the Bayesian approach to update the analytical fragility functions for reinforced concrete (RC) frame buildings with observational damage data from Northridge earthquake in 1994. However, due to the limited number of data covering only six levels of ground motion intensity, the fragility functions are only updated at discrete points. Der Kiureghian (1999a, 1999b, 2002) proposed a Bayesian statistical technique to assess the fragility of lifeline components based on field observations, which is demonstrated on electrical substation equipment. Koutsourelakis (2010) proposed a Bayesian framework for deriving fragility functions by estimating the posterior distributions of the mean ground motion intensity and the dispersion. This method can also be used to update fragility functions. The advantage of this method, compared with the one proposed by Singhal and Kiremidjian (1998), is that the entire fragility function can be updated with limited data, as oppose to updating only discrete points. Some researchers (Gardoni et al, 2002; Gardoni et al., 2003; Choe et al., 2007; Zhong et al., 2008; Huang et al., 2010) focused on developing probabilistic capacity models of structural components, in which Bayesian updating is used to assess the unknown model parameters or update the existing model parameters based on observational data. The probabilistic capacity models are then used to estimate the fragility of structural components.

Compared with observational data, hybrid simulation provides a better way of generating additional data to update analytical fragility functions, because the tests can be conducted in a

controlled manner, leading to a better data distribution in terms of ground motion intensity. In addition, these experimental data can be obtained in a cost-effective way. The effectiveness of using a limited number of data points from hybrid simulation tests to improve the fidelity of fragility functions has not been investigated in previous research.

2.7 Summary

This chapter reviewed some key aspects of the research fields involved in the integrated approach for high fidelity fragility analysis and identified the gaps in knowledge in these key fields. The collection of data using wireless SHM system compliments the limited coverage of strong motion instrumentation. The efficiency of data collection in current wireless SHM system is not optimized and needs improvement. The identification of dynamic parameters of civil infrastructures using seismic measurements is still challenging, and the existing system identification methods may not be readily applied with success using the collected raw data. Decoupling the complex input-output relationship can simplify the system identification problem and can potentially yield more accurate result. A thorough investigation for conducting hybrid simulation under multiple-support excitation is lacking in the literature. Different formulations in conventional dynamic analysis may not be readily adopted in hybrid simulation. Bayesian updating of fragility functions have been studied by many researchers, however, Bayesian updating of fragility functions using hybrid simulation test results and the effectiveness has not been reported in the literature. Systematic integration of these various interdependent components will effectively reduce the uncertainty involved in the fragility derivation process and enhance the accuracy of the subsequent risk assessment. Again, this type of integration has not been seen in the literature. The research presented in the subsequent chapters seeks to develop an integrated approach for generating high-fidelity fragility function by addressing some of the above challenges including monitoring, modeling, and hybrid simulation.

EFFICIENT CAMPAIGN-TYPE SHM USING WSSN

In this chapter, a number of improvements to the ISHMP Services Toolsuite to facilitate efficient data collection for campaign monitoring are presented. A post-sensing time synchronization scheme is proposed to reduce the latency of data collection and provide more effective clock drift compensation for long term data collection. Tests are conducted to assess the synchronization accuracy for both short and long term data collection. In addition, the effectiveness of removing outliers and using nonlinear curve fitting are illustrated. The multi-hop bulk data transfer approach using multiple RF channels is also integrated into the ISHMP Service Toolsuite. The implementation and integration details are also presented. This improved wireless campaign monitoring system provides a more efficient way of collecting high quality data to support accurate structural model characterization, which is an important component in high-fidelity fragility analysis and seismic risk assessment.

3.1 A Post-sensing Time Synchronization Scheme

In this section, the current synchronized sensing middleware service implemented in the ISHMP Service Toolsuite is introduced, followed by a new post-sensing time synchronization scheme which aims to reduce the latency for starting sensing by moving the clock drift compensation phase after sensing is finished. This approach also allows for more effective clock drift compensation for long-time data collection, during which the clock drift rate may change due to temperature variations. Implementation details such as outlier detection and nonlinear curve fitting for drift compensation are discussed herein. Finally, the experimental test results of the post-sensing time synchronization scheme are presented.

3.1.1 Current Synchronized Sensing Middleware Service in the ISHMP Service Toolsuite

The synchronized sensing middleware service in the ISHMP Service Toolsuite has two components, including clock synchronization and data synchronization. The former is realized by a hierarchical synchronization tree protocol based on periodic beacon messages using the Flooding Time Synchronization Protocol (FTSP) (Maroti et al, 2004) packet timestamping method. Clock drift is considered to be linear, and the drift rate is estimated by a least-squares approach with the beacon data points. The estimation is performed before sensing and takes 30 seconds to collect a sufficient number of data points. However, synchronized clocks do not guarantee synchronized data due to the uncertainty of start-up time, the difference of sampling frequency among sensor nodes and the fluctuation of sampling frequency over time (Nagayama and Spencer, 2007). Data synchronization is achieved by a resampling based approach, which addresses the above three issues towards synchronized data (Nagayama and Spencer, 2007). The procedure is illustrated in Fig. 3.1(a).

3.1.2 Post-sensing time synchronization

As shown in Fig. 3.1(a), the current approach to clock drift rate estimation imposes a 30-second delay before sensing starts. To reduce the latency and improve the efficiency of data collection, a single beacon/synchronization message is used to calculate the initial clock offset (Δt_0) and correct the local clocks of the leaf nodes; subsequently, all sensor nodes start sensing at roughly the same time. Meanwhile, the gateway node keeps broadcasting beacon messages with its global time stamps (t_{gb}) during sensing. These beacon messages are sent in a flooding manner which means that upon receiving these beacon messages, the leaf nodes rebroadcast the same

messages. In the meantime, the leaf nodes record the local time stamps (t_{lb}) and calculate the offset (Δt_b). After sensing is finished, the vector of clock offsets and local time stamps are used to estimate the clock drift rate over time through regression analysis, which is then used to correct the time stamps of sensor data (t_{gd}). Resampling is finally carried out based on the drift compensated time stamps. The procedure is illustrated in Fig. 3.1(b) and Fig. 3.5.

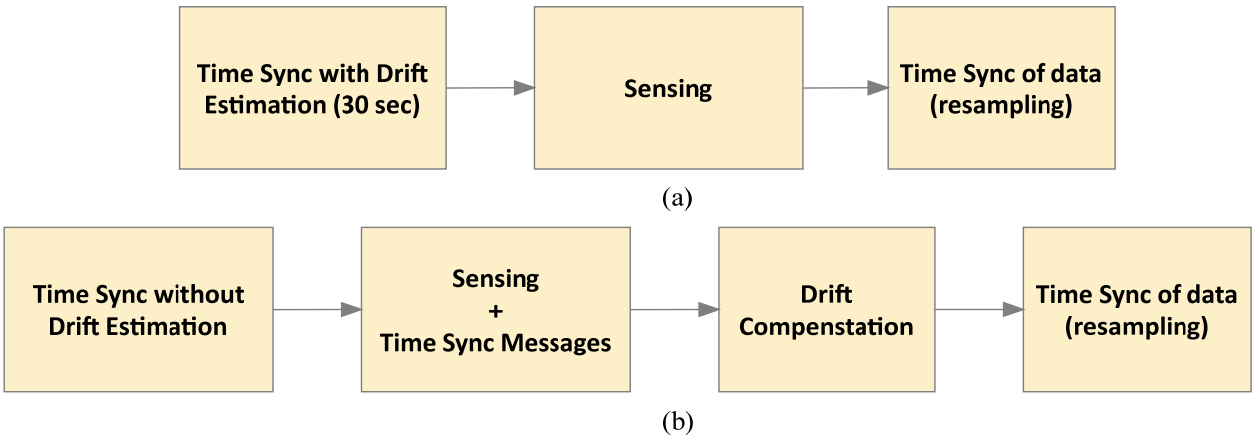

Figure 3.1 Synchronized sensing procedures: (a) pre-sensing time synchronization; (b) post-sensing time synchronization.

Outlier detection and removal using Cook's Distance

One issue to be addressed for post-sensing time synchronization is the potential conflict between the sample acquisition and RF communication for synchronization messages. The proposed post-sensing time synchronization approach requires the smart sensors to handle these two tasks concurrently. With the concurrency model of TinyOS, all tasks are scheduled and executed in a First In, First Out (FIFO) manner. If the entire computation related to sending/receiving messages is finished in the window between sample timestamping, there is no conflict; however, if the message processing is delayed so it overlaps with the sample acquisition and timestamping code, it's up to the scheduler to determine which one executes first and which one is delayed.

Tests were carried out to evaluate the effect of such a conflict. The Imote2 sensor platform with the SHM-A sensor board (commercially available as ISM400 from MEMSIC) (Rice and Spencer, 2009; MEMSIC, 2010) was used in the tests. 100 seconds of data were collected at three different sampling rates: 25 Hz, 100 Hz and 280 Hz. Meanwhile, for all three cases, 100 beacon messages were sent during sensing. The clock offsets collected over time are plotted in Fig. 3.2. Increasing the sampling frequency is shown to increase the chance for outliers. One can imagine that with even higher sampling rates, the number of outliers will increase and can affect the accuracy of clock drift rate estimation. Therefore, detecting the outliers and removing them before regression analysis is essential for effective drift compensation.

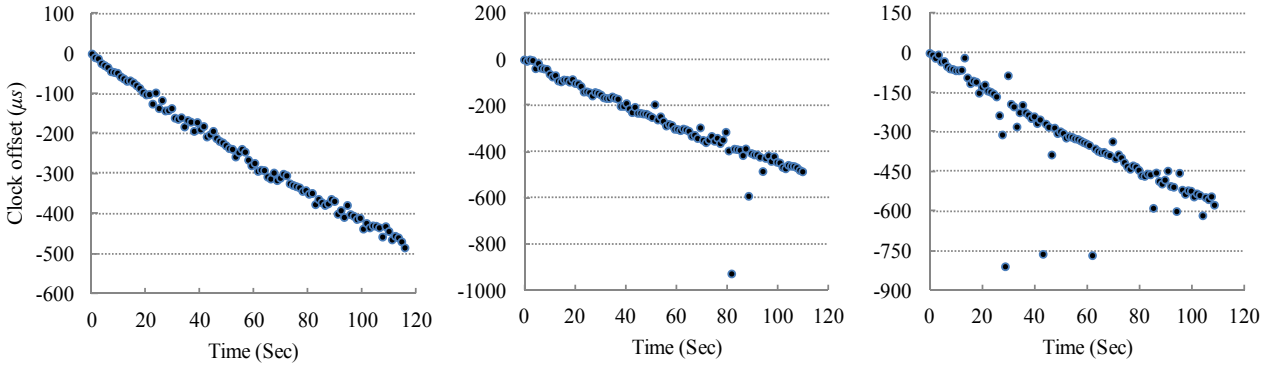

(a) f_s = 25 Hz (b) f_s = 100 Hz (c) f_s = 280 Hz

Figure 3.2 Clock offset during sensing under different sampling rates.

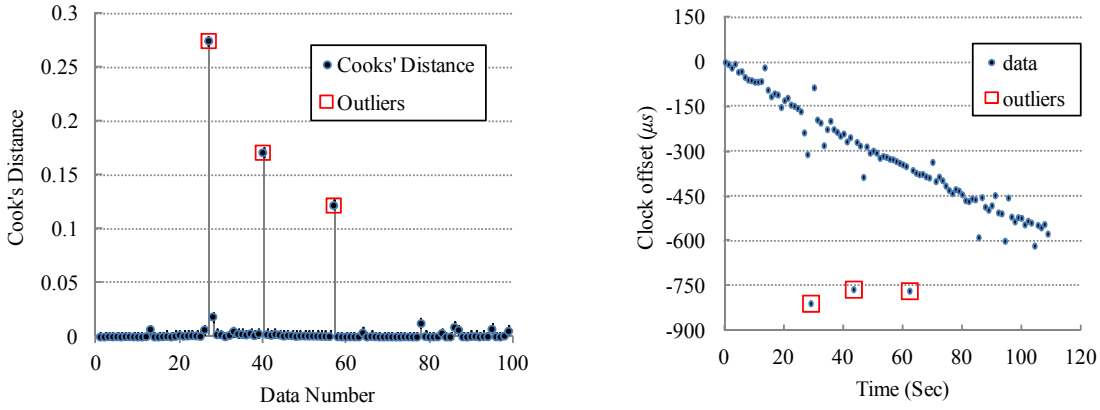

(a) Cook's distances (b) Outliers

Figure 3.3 Outlier detection using Cook's Distance.

Cook's distance (Cook, 1977) is employed in this study to detect outliers from the collected synchronization data. In regression analysis, Cook's distance measures the influence of removing one certain data point, which is calculated as

$$D_i = \frac{\sum_{j=1}^{n}\left(\hat{y}_j - \hat{y}_j(\mathrm{i})\right)^2}{(p+1)s^2}, \quad i = 1,2,...,n \tag{3.1}$$

in which $\hat{y}_j$ and $\hat{y}_j(\mathrm{i})$ are the regression estimates of the observation j using the full data set and the data set with the i^{th} data point removed, respectively; s^2 is the mean square error of the regression model; $p+1$ is the number of parameters in the regression model. Large value of Cook's Distance indicates outlier in the synchronization message caused by the conflict. As a rule of thumb, a data point is treated as outlier when

$$D_i \geq \frac{4}{n-(p+1)} \tag{3.2}$$

Cook's Distance is implemented in TinyOS as a numerical service in the ISHMP Services Toolsuite. Fig. 3.3(a) shows the Cook's Distance for the data given in Fig. 3.2(c), and the detected outliers are highlighted in Fig. 3.3(b), which demonstrates Eq. (3.2) effectively removes the outliers from the collected time synchronization data.

Nonlinear regression analysis for clock drift compensation

Clock drift is another common issue that needs to be addressed for time synchronization of distributed systems. In the current ISHMP synchronization protocol, clock drift is compensated by estimating a constant drift rate using linear regression. However, the crystal oscillator in the timer circuit of Imote2 is sensitive to temperature changes (Uddin and Castelluccia, 2010; Yang et al., 2012). Clock drift usually is linear if the temperature remains constant. However, the temperature of the Imote2 oscillator could change due to (1) environmental temperature change during sensing and (2) the heat generated by the Imote2 CPU and the Quickfilter ADC chip on the SHM-A sensor board. Fig. 3.4 shows the results from an indoor test with four Imote2 leaf nodes. In the test, an application was designed to collect time stamps and temperature readings from these leaf nodes during sensing. While the indoor environment provides constant ambient temperature, the on-board temperature of Imote2 was raised by almost 6 ^{o}C in 10 minutes due to the heat generated by the CPU and the Quickfilter chip on the SHM-A sensor board. As a result, all four curves of clock drift have significant nonlinearity (see Fig. 3.4). Note that unit-to-unit variation is found in the clock drift between sensors, which is why the sensors exhibit different offset curves for very similar temperature changes. Therefore, for long term data collection during which temperature change due to either of the above two factors may become significant, nonlinear regression analysis is needed to achieve high accuracy of time synchronization. The clock drift compensation procedure employing both the Cook's distance and nonlinear regression analysis is illustrated in Fig. 3.5.

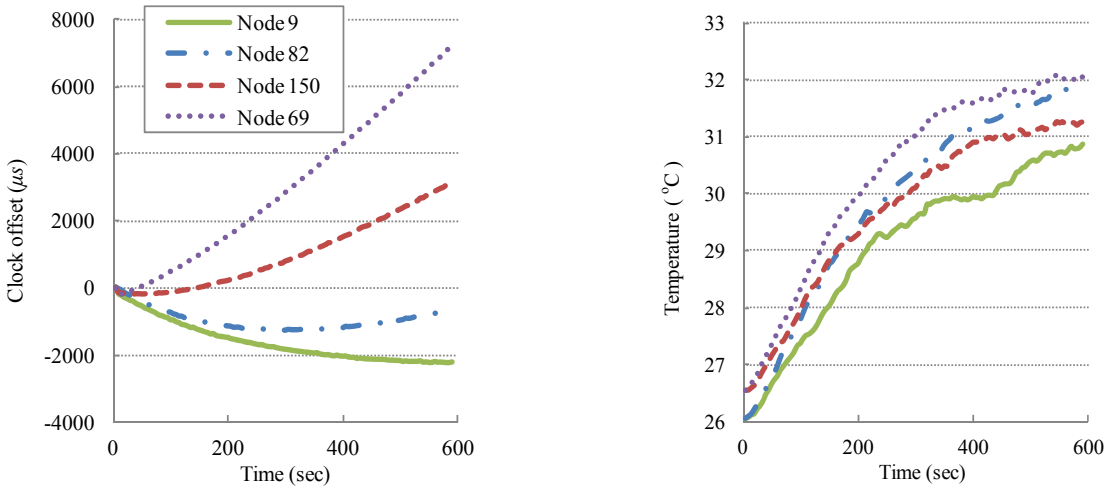

Figure 3.4 Nonlinear clock drift (left) due to temperature change (right).

1. Record beacon data (during sensing): $\Delta t_b = t_{gb} - t_{lb}$ (3.3)

2. Outlier detection and removal for beacon data (after sensing)

3. Regression analysis (after sensing): $\Delta t_b = c_0 + c_1 t_{lb} + c_2 t_{lb}^2 + \cdots + c_p t_{lb}^p$ (3.4)

   ($c_0, c_1, \ldots c_p$ are regression parameters; p is the order of regression analysis.)

4. Correct data time stamps (after sensing): $t_{ld} = t_{gd} - \Delta t_0$ (local time stamp of sensor data) (3.5)

   $\Delta t_{ld}^{corrected} = c_0 + c_1 t_{ld} + c_2 t_{ld}^2 + \cdots + c_p t_{ld}^p$ (3.6)

   $t_{gd}^{corrected} = t_{ld} + \Delta t_{ld}^{corrected}$ (3.7)

Figure 3.5 Clock drift compensation procedure in the post-sensing time synchronization scheme.

3.1.3 Time synchronization accuracy

To estimate the performance of the proposed post-sensing time synchronization scheme, as depicted in Fig. 3.6, tests were conducted using one Imote2 sensor platform as the gateway node connected to the base station computer and three Imote2s with SHM-A sensor boards as leaf nodes. A Siglab spectrum analyzer (Spectral Dynamics, Inc., 2012) provides the signal to the 4th channel of the SHM-A sensor board on each Imote2. To make sure each sensor node receives an identical signal from Siglab, split connectors were used to connect all senor nodes to the same output channel of Siglab. The input signal is Band Limited White Noise (BLWN) with 20 Hz bandwidth. The sampling frequency of data acquisition is 100 Hz. Time synchronization error between two sensor nodes can be evaluated through the phase angle of the cross power spectrum between their acceleration data. More specifically, linear curve fitting is applied to the phase angle in the range between 0 and 20 Hz to find the slope of the phase angle, θ, which can be converted to time synchronization error in microseconds as

$$TS_{error} = \frac{\theta}{2\pi} \times 10^6 \ (\mu s) \tag{3.8}$$

Several tests were carried out for three different sensing durations, including 1 minute, 10 minutes and 30 minutes. Both linear curve fitting and nonlinear curve fitting (5th order) were applied to clock drift compensation. Outlier detection and removal algorithm was used for both cases. In the calculation of the cross power spectral densities, the Hanning window with the width of 1024 Fast Fourier Transform (FFT) points and 50% overlapping was adopted. For each pair of sensor nodes, the absolute values of the synchronization errors from three repeated tests were averaged. The results are summarized in Table 3.1. The proposed post-sensing time synchronization scheme achieves high accuracy both in short and long term data collection. Moreover, for long term data collection, especially for the 30-minute case, when the proposed

nonlinear curve fitting is applied in the clock drift compensation, the accuracy of time synchronization is improved significantly compared with the case with linear curve fitting.

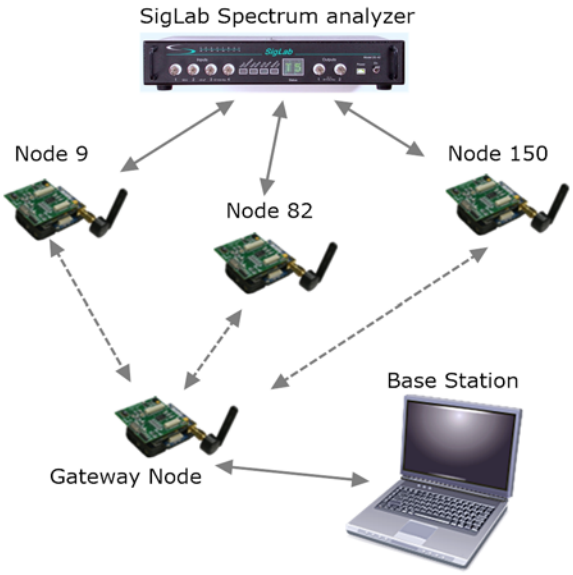

Figure 3.6 Test Setup for time synchronization accuracy estimation.

Table 3.1 Time Synchronization errors with post-sensing time synchronization

Sensing Duration	Curve Fitting Approach in Drift Compensation	Pairwise synchronization Error (μ sec)		
		Node 9 and 82	Node 9 and 150	Node 82 and 150
1 min	1st order	26.3	6.8	22.8
	5th order	25.5	6.7	22.6
	difference*	-2.98%	-1.21%	-0.87%
10 min	1st order	19.2	10.6	25.2
	5th order	18.4	10.4	24.8
	difference*	-4.25%	-2.05%	-1.57%
30 min	1st order	11.3	15.0	26.3
	5th order	6.9	13.0	19.9
	difference*	-38.55%	-13.37%	-24.15%

* difference = (5th order - 1st order)/(1st order)*100%

3.2 Multihop Bulk Data Transfer

In multihop communication, transporting large data set in wireless SHM applications is challenging. In the current ISHMP Services Toolsuite, to avoid packet collisions, data retrieval in multihop is done in a sequential manner, i.e. the gateway node requests data from each leaf node one by one. This approach slows down the data retrieval significantly especially when the number of hops is large. Nagayama et al. (2010) proposed a multihop bulk data transfer protocol which utilizes multiple RF channels to allow multiple neighboring pairs of nodes to transmit data simultaneously. As a joint research effort between the University of Illinois and the University of Tokyo, multihop bulk data transfer has been integrated into the ISHMP Services Toolsuite. For completeness, the background of the protocol is first introduced, followed by some additional considerations to improve the efficiency of data collection in campaign monitoring using the multihop bulk data transfer protocol.

3.2.1 Multihop Routing for single sink data collection

To facilitate the multihop bulk data transfer with multiple RF channels, a specific routing protocol was designed (Nagayama et al., 2010).A single sink node is assumed, which in this case is the gateway node in SHM system. The routing process is performed in a backwards manner from the leaf nodes to the gateway node. First, the leaf nodes within one-hop range of the gateway node establish routes; then the leaf nodes that are two-hops away from the gateway node find the routes. The process repeats for a predetermined number of times until all nodes in the network have a route to the gateway node. The procedure is illustrated in Fig. 3.7.

To initialize the routing process, the gateway node sends a command to the leaf nodes. Upon receiving the command, the leaf nodes start to broadcast the Route Request (RREQ) messages with Time-To-Live (TTL) equal to one hop. To avoid heavy package collision when many nodes start to broadcast messages, each node waits for a random interval before broadcasting. The value of TTL decides how far the RREQ messages can travel. Having TTL = 1 reduces the packet collision in the network and allows the shortest path to be built. When the gateway node receives the RREQ messages, it examines the Received Signal Strength Indicator (RSSI) values and responds with Route Reply (RREP) messages if the RSSI value is higher than a predetermined threshold value. When the RREP messages reach the leaf nodes which sent the RREQ messages, the leaf nodes examines the RSSI value and establish routes to the gateway node if the RSSI value is higher than the threshold. After the first stage, all nodes within one-hop range from the gateway node have established routes to the gateway node.

After waiting for a random interval, the rest of the leaf nodes that still do not have routes to the gateway node continue to broadcast RREQ messages. Now not only the gateway node, but also the leaf nodes which have built routes to the gateway node are eligible to reply with RREP messages. If the RSSI values in both the RREQ and RREP messages satisfy the threshold, the routes are established. The same process is repeated for nodes that are more hops away until all nodes in the network have routes to the gateway node or a timeout timer is fired.

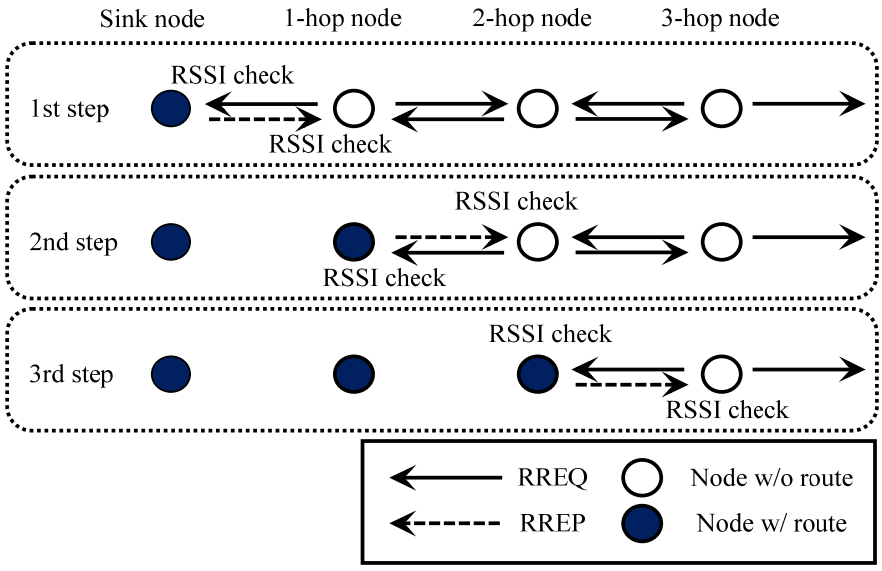

Figure 3.7 Multihop routing process for single sink data collection (Nagayama et al., 2010).

3.2.2 Multihop data forwarding using multiple RF channels

Having the routing table obtained in the previous step, the network can be divided into layers assigned with two additional channels besides the common communication channel. One is the data transmit channel and the other is the data reception channel. The data reception channel of the lower layer nodes is the same as the data transmit channel of its upper layer nodes. For example, the nodes which are *n*-hops away from the gateway node, also called the *n*-hop layer nodes, have the data reception channel the same as the data transmit channel as the (*n*+1)-hop layer nodes. The IEEE802.15.4 RF device employed by the Imote2 sensor platform provides 16 user-selectable and non-overlapping channels. These 16 channels are used in a round robin manner in the case when more than 16 hops are needed, providing network scalability. For example, the 17-hop layer nodes and the 1-hop layer nodes will share the same channels; however, the interference between these two layers is considered minimal because they are physically far apart from each other.

When sensing is finished and data is saved into the flash memory of each leaf node, the gateway node sends a command to the leaf nodes to initiate the data forwarding process. When data is ready to be transmitted back to the gateway node, all nodes in the network switch to their own data reception channel from the common communication channel. After a random wait interval, when a sender node starts to transmit data using the routing table, it switches its RF channel to its data transmit channel, and examines whether the channel is being used by other nodes. If the channel is being used, the sender node waits for another random interval. If not, the sender node sends an inquiry packet to the receiver node asking if the receiver node is ready. If the receiver node is not communicating with other nodes and has adequate buffer space, the data forwarding begins. Using a reliable data transfer service (Nagayama and Spencer, 2007), the sender sends all sensor data stored in flash memory to the receiver and then switches its RF channel to the data reception channel. If the receiver is not ready, the sender waits for a random interval before starting the process again. Fig. 3.8 illustrates the simultaneous data transfer between multiple pairs of sensor nodes within the network using multiple RF channels.

3.2.3 Test results

In test results reported by Nagayama, et al. (2010), 49 sensor nodes were installed on a suspension bridge in Japan. Routes with maximum of eight hops were established in the network. Data was collected using two gateway nodes. One of the gateway nodes collected data from 24 sensor nodes; each one has 108 kB of data. Six minutes was used to retrieve all data back, resulting in 7.2 kB/s throughput. Compared with the data throughput of the MintRoute-based approach reported by Kim, et al. (2007), which is about 0.75 kB/s, the proposed Multihop Bulk Data Transfer approach achieved approximately a tenfold improvement in performance.

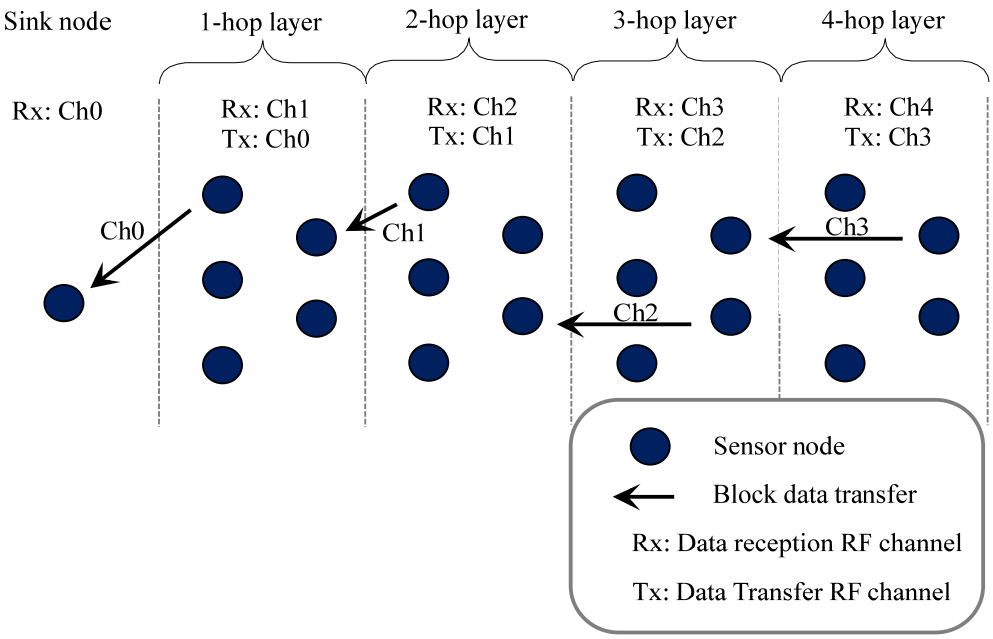

Figure 3.8 Bulk data transfer using multiple RF channels (Nagayama et al., 2010).

3.2.4 Implementation in the ISHMP Services Toolsuite

The Multihop Routing and Data Forwarding methods described above are modularized into two separate interfaces in the ISHMP Service Toolsuite, which are then integrated into the current *RemoteSensing* application for data retrieval once data becomes available. Meanwhile, current command delivery approach does not suit the need to maintain high efficiency of the new Multihop Bulk Data Transport method; a different flooding based command delivery approach is therefore implemented.

In the current ISHMP Services Toolsuite, commands are delivered using a series of unicasts based on the reliable communication protocol. This acknowledgement based method ensures the reliability of command delivery but may slow down the application when the network size is large and a few nodes do not respond, thus cancelling out the benefit of the Multihop Bulk Data Transport method. Moreover, the Data Forwarding service assumes all sensor nodes start forwarding data approximately at the same time. Therefore, commands, such as the initialization of multihop routing and data forwarding, are all delivered using flooding.

Flooding is also implemented to wake up the network. For campaign monitoring, to conserve energy during sensor node installation, sensor nodes are put into sleep cycle, in which the nodes spend most of the time in a low-power deep sleep mode and wake up periodically to

listen for external commands. Waking up the network as quickly as possible is also critical for efficient data collection. In the implementation, to wake up the network, the gateway node keeps broadcasting the wakeup messages to the network for duration t, which is the sleep time in the sleep cycle. Upon reception of the wakeup message after switching to the listening mode, the leaf nodes stay awake and also keep broadcasting the same wakeup command for duration t. Meanwhile, the gateway node keeps listening to the wakeup messages coming back from the network during the flooding process. When the gateway node no longer receives wakeup messages from the network, the wakeup process is considered completed. If the maximum number of hops in the network is N, after $N \times t$ seconds, it is almost sure that all nodes are awake.

One more issue is resetting the network after data forwarding is finished. As described in section 3.2.2, all nodes will switch back to their own data reception RF channel after current data block has been transferred, waiting for the next round of data transfer. Without a notification message sent from the gateway node or a timer to timeout the data forwarding, the leaf nodes will not know whether the data forwarding is completed or not and stay in their own RF reception channels, making the network unreachable by communication within any one RF channel. In the implementation, the gateway node sends the reset command by scanning all the available RF channels. Upon the reception of the reset command, leaf nodes also broadcast the command by scanning all the RF channels. After a timeout timer gets fired, all nodes that have received the reset command reset themselves and hence switch back to the common communication RF channel.

3.3 Summary

In this chapter, critical components of an efficient campaign-type SHM system based on WSSNs have been proposed and implemented. A post-sensing time synchronization scheme was proposed to reduce the latency of data collection while maintaining high accuracy of synchronization of collected data. Results showed that high accuracy of synchronization was achieved for both short and long term data collection. In addition, removing outliers and nonlinear curve fitting were found essential for effective clock drift compensation. A multi-hop bulk data transfer approach using multiple RF channels was also integrated into the ISHMP Services Toolsuite to achieve high data throughput. This efficient wireless campaign monitoring system, along with the traditional seismic instrumentation systems, serves as a critical tool for collecting essential data to facilitate accurate structural characterization, which will be discussed in the next chapter.

SYSTEM IDENTIFICATION USING DECOUPLED OUTPUT SIGNALS

System identification with the measured structural response serves as a critical step towards high accuracy structural modeling, which is an essential component in high-fidelity fragility analysis and seismic risk assessment. Despite the numerous advances in system identification techniques, challenges still remain in their applications to civil engineering structures, such as bridges, buildings, and towers. These structures typically have numerous degrees-of-freedom (DOFs) and large physical dimensions, and are often subjected to multi-directional actions such as earthquake ground motion, which lead to complex structural responses. The contributions from the latter multi-directional actions to the response are highly coupled, leading to a Multiple-Input, Multiple-Output (MIMO) system identification problem. Compared with Single-Input, Multiple-Output (SIMO) system identification, MIMO problems are more computationally complex and error-prone. In this chapter, a new system identification strategy is proposed for civil engineering structures with multiple inputs that induce strong coupling in the response. The proposed solution comprises converting the MIMO problem into separate SIMO problems, decoupling the outputs by extracting the contribution from the respective input signals to the outputs. To this end, a QR factorization-based decoupling method is employed, and its performance is examined. Three factors which affect the accuracy of the decoupling result, including memory length, input correlation, and system damping, are investigated. Additionally, a system identification method which combines the AutoRegressive model with eXogenous input (ARX) and the Eigensystem Realization Algorithm (ERA) is proposed. The associated Extended Modal Amplitude Coherence (EMAC) and Modal Phase Collinearity (MPC) are used to delineate the structural and noise modes in the fitted ARX model. The efficacy of the ARX-ERA method is then demonstrated through identification of the modal properties of a highway overcrossing bridge.

4.1 Decoupling of MIMO System

Considering a Multiple Input and Multiple Output (MIMO) Linear Time Invariant (LTI) system with n inputs ($x_1, x_2, \ldots, x_n$) and m outputs ($y_1, y_2, \ldots, y_m$), in discrete time domain, the response of each output can be expressed as a linear combination of delayed copies of the input signals given by

$$y_j(t) = \sum_{i=1}^{n} \sum_{\tau=0}^{M-1} h_{ji}(\tau) x_i(t-\tau) + \omega(t), \; j = 1, 2, ..., m \tag{4.1}$$

in which h_{ji} is the Impulse Response Function (IRF) from input x_i to output y_j, M is the memory length of the system, and $\omega(t)$ is a term to account for the noise in the output measurement as well as the effect of unmeasured disturbances. The memory length (M) is a finite number if the underlying system is a Finite Impulse Response (FIR) system, and is infinity for an Infinite Impulse Response (IIR) system.

In the above MIMO system, the measured output y_j may contain contribution from any of the n inputs if the corresponding IRF is not zero. As discussed in the previous section, having coupled multiple inputs will complicate the system identification problem not only because more

computational power is required, but also its accuracy may decrease. To identify the component in the output which can be attributed solely to a specific input, Westwick et al. (2006) proposed a method based on QR factorization. To find the contribution of the input x_k to the output y_p, two matrices are first constructed

$$\begin{aligned}\mathbf{M}_1 &= \left[\mathbf{X}_1,...,\mathbf{X}_{k-1},\mathbf{X}_{k+1},...,\mathbf{X}_n\right] \\ \mathbf{M}_2 &= \mathbf{X}_k\end{aligned} \tag{4.2}$$

where $\mathbf{X}_i\left(i=1,2,...,k,...,n\right)$ are block matrices formed by delayed copies of the input x_i with T elements:

$$\mathbf{X}_i = \begin{bmatrix} x_i(1) & 0 & \cdots & 0 \\ x_i(2) & x_i(1) & \cdots & 0 \\ \vdots & \vdots & \ddots & \vdots \\ x_i(T) & x_i(T-1) & \cdots & x_i(T-M+1) \end{bmatrix} \tag{4.3}$$

The matrix $\mathbf{M}_1$ contains the inputs of the structure whose contribution to the output y_p are not of interest, while $\mathbf{M}_2$ contains the input of interest to the output y_p.

The next step is to combine the above two matrices with the output vector to be decoupled and then apply QR factorization to the combined matrix, as shown in Eq. (4.4). The input signals are orthogonalized and the desired output can be projected onto these orthogonalized vectors.

$$\begin{bmatrix}\mathbf{M}_1 & \mathbf{M}_2 & \vec{y}_p\end{bmatrix} = \mathbf{QR} = \begin{bmatrix}\mathbf{Q}_1 & \mathbf{Q}_2 & \vec{q}_y\end{bmatrix}\begin{bmatrix}\mathbf{R}_{11} & \mathbf{R}_{12} & \vec{r}_{1y} \\ 0 & \mathbf{R}_{22} & \vec{r}_{2y} \\ 0 & 0 & r_{3y}\end{bmatrix} \tag{4.4}$$

Here, $\mathbf{Q}_1$ and $\mathbf{Q}_2$ have the same dimensions as $\mathbf{M}_1$ and $\mathbf{M}_2$, respectively. The projection of each input and the output to a new set of orthogonalized vectors can be obtained as follows,

$$\begin{aligned}\mathbf{M}_1 &= \mathbf{Q}_1\mathbf{R}_{11} \\ \mathbf{M}_2 &= \mathbf{Q}_1\mathbf{R}_{12} + \mathbf{Q}_2\mathbf{R}_{22}\end{aligned} \tag{4.5}$$

and

$$\vec{y}_p = \mathbf{Q}_1\vec{r}_{1y} + \mathbf{Q}_2\vec{r}_{2y} + \vec{q}_y r_{3y} \tag{4.6}$$

As can be seen from Eq. (4.6), the three terms in the equation are orthogonal to each other because all columns in $\mathbf{Q}$ are orthogonal. Therefore, the second term $\mathbf{Q}_2\vec{r}_{2y}$ is orthogonal to $\mathbf{Q}_1$ and hence $\mathbf{M}_1$. Thus, $\mathbf{Q}_2\vec{r}_{2y}$ can be considered as the component in the output $\vec{y}_p$ which is attributed solely to the input $\mathbf{X}_k$.

The next step in Westwick et al. (2006) is the computation of the mean squared value of the second term in Eq. (4.6). This step ranks the importance of each input, allowing insignificant inputs to be removed subsequently. However, the interests in the application of this method herein is to use the term related to the decoupled output to convert the MIMO problem into a

SIMO one. The above procedure can be applied in a sequential manner to all output measurements such that the contributions from a specific input to these outputs can be extracted and then used to identify the SIMO systems. In this regard, the accuracy of the decoupled output is essential to system identification. In the following sections, three factors that have significant impact on the accuracy of the decoupling result will be investigated, including the memory length used in Eq. (4.3), the correlation of the inputs, and the system damping ratio.

4.1.1 FIR and IIR Systems

Two types of dynamic systems are considered including a Finite Impulse Response (FIR) system and an Infinite Impulse Response (IIR) system. The reason for investigating both types of systems is that the original algorithm was developed for FIR systems, but most civil engineering structures belong to IIR systems. For illustrative purposes, systems having three degrees-of-freedom (DOFs) are considered. As shown in Fig. 4.1a, the FIR system consists of three 30^{th} order FIR lowpass filters which have different stopband and passband frequencies. Each of the filters takes a band limited Gaussian white noise as input and the corresponding outputs are then mixed with a 3×3 mixing matrix to generate three coupled outputs. The IIR system depicted in Fig. 4.1b is realized by a spring-mass system which also takes three band limited Gaussian white noise inputs and generates three coupled outputs. 5% damping is considered in the IIR system. The inputs and outputs are acceleration signals for both systems. The simulation parameters, for both systems, consist of 30 seconds in duration and a sampling frequency of 100 Hz.

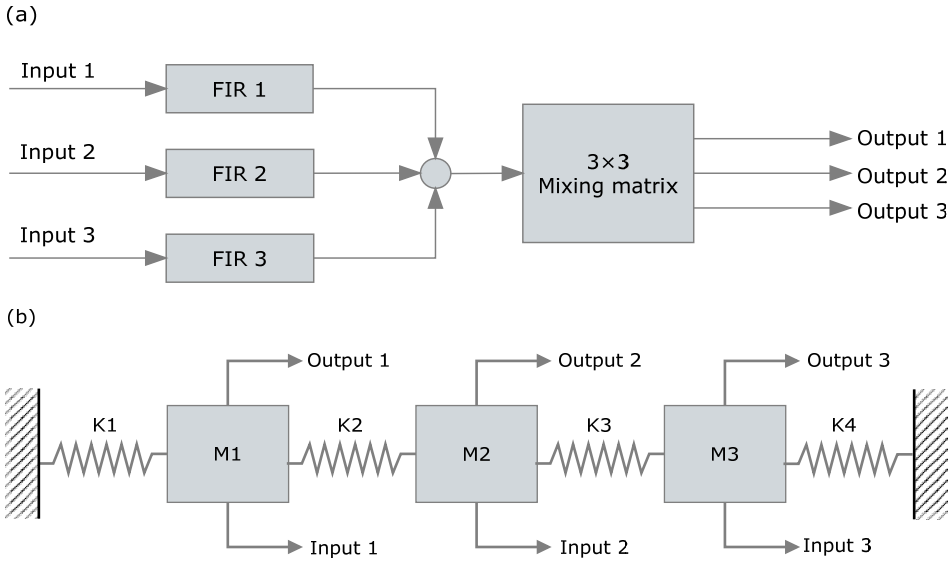

Figure 4.1 Two types of dynamic systems: (a) FIR; (b) IIR.

4.1.2 Effect of the Memory Length

As indicated in Eq. (4.1), the memory length M controls the duration of the past input which can affect the current output. Therefore, for FIR systems which have a finite memory length, the number of columns in Eq. (4.3) is equal to M. However, for IIR systems, the memory length is infinite, and in such cases, the selection of M for the input matrices in Eq. (4.3) becomes less apparent. If the memory length is too small, the constructed input matrices may not provide adequate information for the orthogonalized matrices in Eq. (4.6) to fully reconstruct the target

output. If the selected memory length is too large, resulting in a large matrix in Eq. (4.4), the QR decomposition will be more computationally demanding and error-prone.

To investigate the effect of the memory length on the accuracy of the decoupled responses for both FIR and IIR systems, numerical simulations are carried out based on the above two models. Three uncorrelated band limited Gaussian white noise inputs are generated and then fed into the two systems. The effect of correlation between inputs is not considered here but will be discussed in the next section. The coupled output signals are recorded for decoupling analysis. By changing the memory length M, the QR decomposition-based method introduced in the preceding section is applied to all three outputs sequentially to exact contributions from the three inputs, resulting in nine sets of decoupled outputs. The accuracy of the decoupled output is represented by an error factor J (Werner et al., 1987), defined by

$$J_{kp} = \sum_{i=1}^{T} \left(y_{kp}^{\text{ref}}(i) - y_{kp}^{\text{dec}}(i) \right)^2 \Big/ \sum_{i=1}^{T} \left(y_{kp}^{\text{ref}}(i) \right)^2, \quad k = 1,2,3, \;\; p = 1,2,3 \tag{4.7}$$

The superscript "ref" denotes the reference signals and "dec" means the decoupled outputs. k and p are the indices of the input and output, respectively. For example, y_{12} denotes the contribution from the Input 1 to the Output 2 and J_{12} is the corresponding error factor.

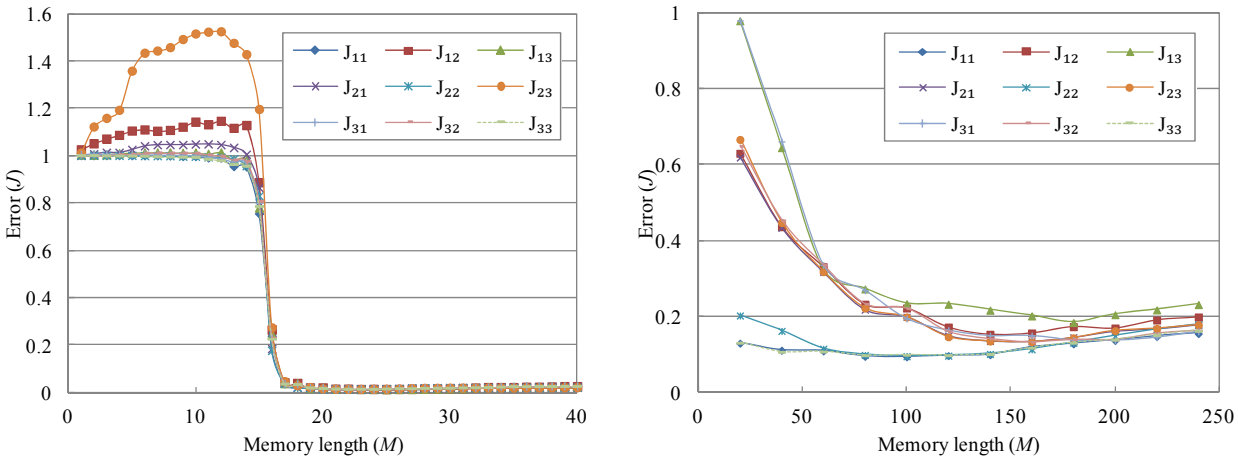

Figure 4.2 Accuracy of decoupled outputs for different memory lengths for FIR system (left) and IIR system (right).

Table 4.1 Minimum errors of the decoupled outputs and the corresponding memory lengths

	J_{11}	J_{12}	J_{13}	J_{21}	J_{22}	J_{23}	J_{31}	J_{32}	J_{33}
FIR	0.0119	0.0119	0.0119	0.0122	0.0121	0.0125	0.0130	0.0130	0.0130
IIR	0.0941	0.1567	0.1845	0.1353	0.0958	0.1341	0.1381	0.1338	0.093
	M_{11}	M_{12}	M_{13}	M_{21}	M_{22}	M_{23}	M_{31}	M_{32}	M_{33}
FIR	25	25	25	23	22	23	24	24	24
IIR	100	140	180	160	100	160	200	160	80

Fig. 4.2 shows the change of J values as the memory length increases. The minimum J values and the corresponding optimal memory lengths are listed in Table 4.1. First of all, for the FIR system, when the memory length reaches a threshold (M=17 in this case), the error of each decoupled output decrease dramatically and becomes relatively stable beyond that point. The minimum errors are found to be very small (less than 0.015), indicating high accuracy achieved in the decoupled outputs. A sample result for the FIR system is plotted in Figs. 4.3a,b, where the reference signals are obtained by simulations with a single input. The decoupled contribution from Input 1 to Output 1 matches very well with the reference signal. However, the minimum errors are found when M is less than 31, which is the filter length or the theoretical memory length, possibly due to numerical error in QR decomposition when dealing with large matrices.

For the IIR system, no clear threshold is observed as the J values change more slowly when varying the memory length. Unlike the FIR system, the IIR system takes infinite time for the system dynamics to die out, or at least it takes much longer time to decrease to a low level when damping is small; therefore, the optimal memory lengths are all larger than the FIR system and are associated with larger uncertainty. The overall accuracy of the decoupled outputs is not as high as the FIR system, due to the fact that the QR decomposition has to deal with much larger matrices and the larger uncertainties from the optimal memory length. However, the decoupled outputs still possess reasonable accuracy, especially for the diagonal terms where the input and the output share the same DOF (i.e., J_{11}, J_{22} and J_{33} are all less than 0.1). Sample results for J_{11} shown in Figs. 4.3c,d demonstrate a good match between the decoupled response and reference signal.

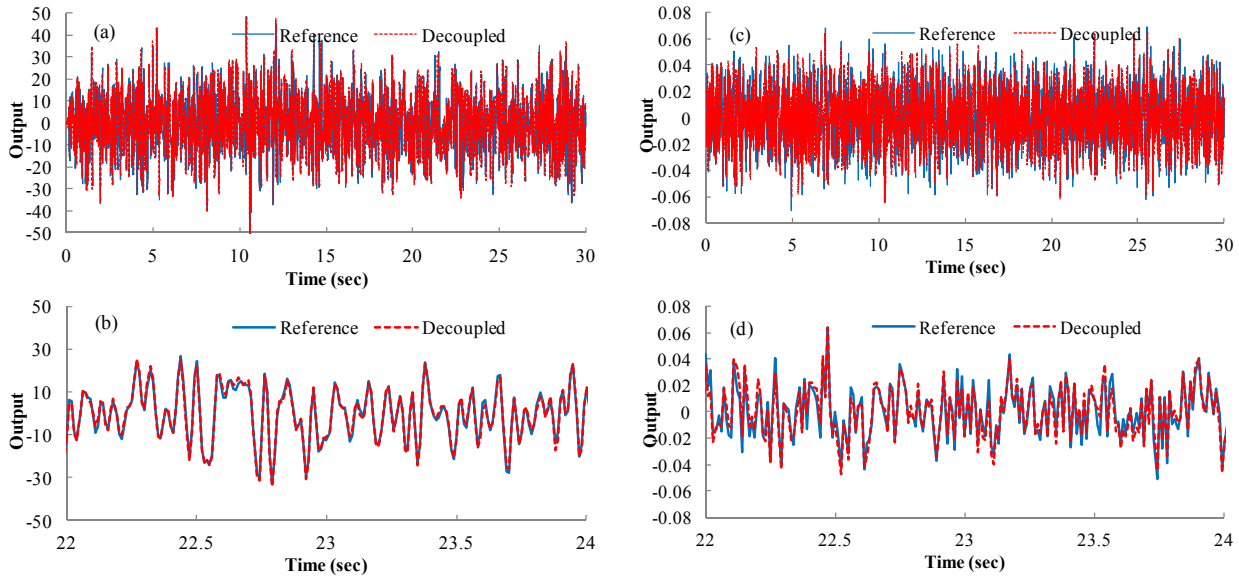

Figure 4.3 Comparison between the decoupled and reference outputs.
(a) and (b): J_{11} of the FIR system; (c) and (d): J_{11} of the IIR system.

4.1.3 Effect of the Input Correlation

The effectiveness of the decoupling method has been demonstrated with uncorrelated inputs; however, the correlation of the inputs can affect the accuracy of the result. If a system is

subjected to two identical inputs (fully correlated), distinguishing between the contributions from these two inputs to the output will be challenging. Assessment of the influence of the input correlation gives a broader picture of the decoupling approach.

Two aspects of the input correlation are investigated including global correlation and local correlation; both are quantified by a correlation coefficient. The global correlation coefficient between two discrete signals $x_1(i)$ and $x_2(i)$ is computed using the entire records and is defined as:

$$\rho = \frac{\sum_{i=1}^{N}\left[x_1(i)-\bar{x}_1\right]\left[x_2(i)-\bar{x}_2\right]}{\sqrt{\sum_{i=1}^{N}\left[x_1(i)-\bar{x}_1\right]^2}\sqrt{\sum_{i=1}^{N}\left[x_2(i)-\bar{x}_2\right]^2}} \tag{4.8}$$

where N is the length of a signal. $\bar{x}_1$ and $\bar{x}_2$ are the mean values of x_1 and x_2, respectively. The local correlation coefficient is calculated within a sliding window to track the correlation between two signals over time, and is therefore defined as:

$$\rho_w(t) = \frac{\sum_{i=t}^{t+w}\left[x_1(i)-\bar{x}_{1t}\right]\left[x_2(i)-\bar{x}_{2t}\right]}{\sqrt{\sum_{i=t}^{t+w}\left[x_1(i)-\bar{x}_{1t}\right]^2}\sqrt{\sum_{i=t}^{t+w}\left[x_2(i)-\bar{x}_{2t}\right]^2}} \tag{4.9}$$

where w is window length. $\bar{x}_{1t}$ and $\bar{x}_{2t}$ are the mean values of x_1 and x_2 within the sliding window at time t, respectively.

To generate two inputs which are globally uncorrelated but have varying correlation over time, two earthquake records measured at the same location but in perpendicular directions are selected. These two records are orthogonalized to make them globally uncorrelated, but the local correlation is still time-varying. Fig. 4.4 shows the time history of the orthogonalized records, as well as the change of correlation angle over time. Note that correlation coefficient is cosine of the angle between two time series vectors. The window size is 5 seconds when calculating the local correlations. These two inputs are then used as the Input 1 and Input 2 to the FIR system shown in Fig. 1a and Input 3 is set to zero. Fig. 4.5a shows the change of J_{11}, which has a minimum value of 0.00956 when the memory length equals to 23. Such a high accuracy indicates that the performance of the decoupling approach is not affected by the local correlation of the inputs. Therefore, high accuracy can be achieved as long as the inputs are globally uncorrelated.

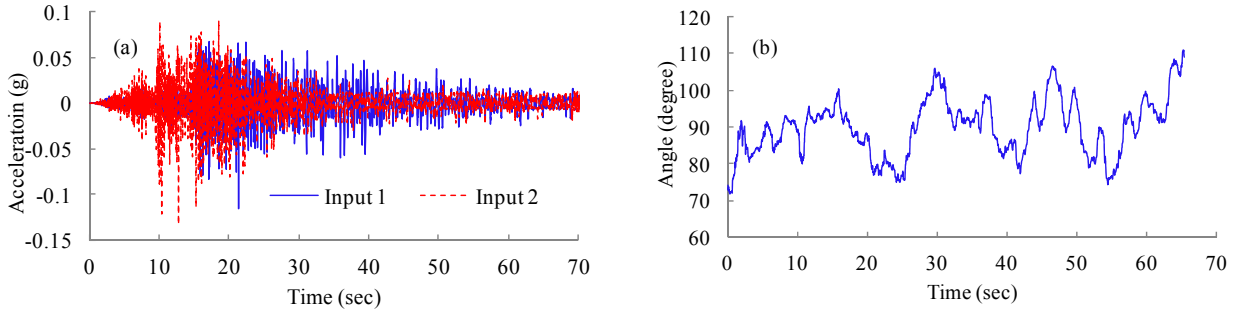

Figure 4.4 Two orthogonalized earthquake inputs (a) with time-varying correlation (b)

Knowing that the local correlation of inputs is not affecting the performance of the decoupling approach, the effect of the global correlation is then further investigated. A series of pairs of band limited white noise inputs are generated with global correlation angles ranging from 0 to 90 degrees. Similarly, the two inputs are applied to the first two DOFs of both the FIR and the IIR systems. The changes of J_{11} are plotted in Fig. 4.6, showing clearly that the accuracy of the decoupled output increases when the input correlation decreases. At 90 degrees angle, the result reflects the conclusion from the previous section, namely, the FIR system has higher accuracy in the result than the IIR system. One important observation for the IIR system is that when the angle between the two inputs is larger than 80 degrees, the error in the decoupled output is lower than 0.1. Because all civil engineering structures are IIR systems, this observation can serve as a rough guideline to assess whether the decoupling approach is applicable or not to a specific problem.

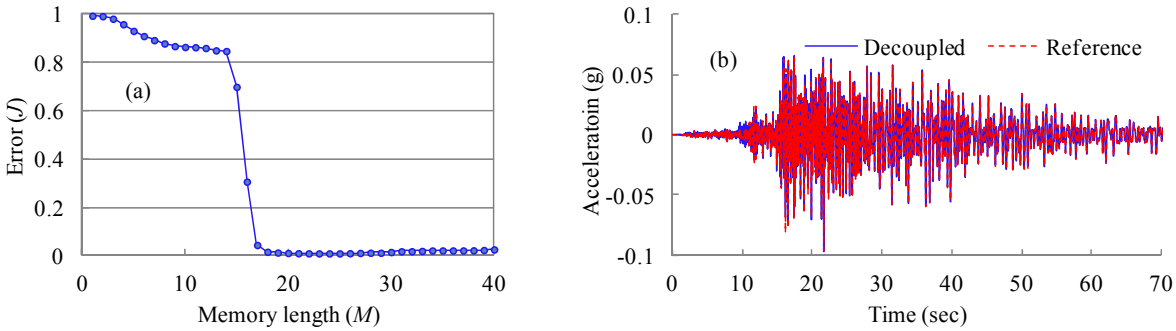

Figure 4.5 Decoupling result with the orthogonalized earthquake inputs: (a) change of error with different memory lengths; (b) decoupled output at the optimal memory length.

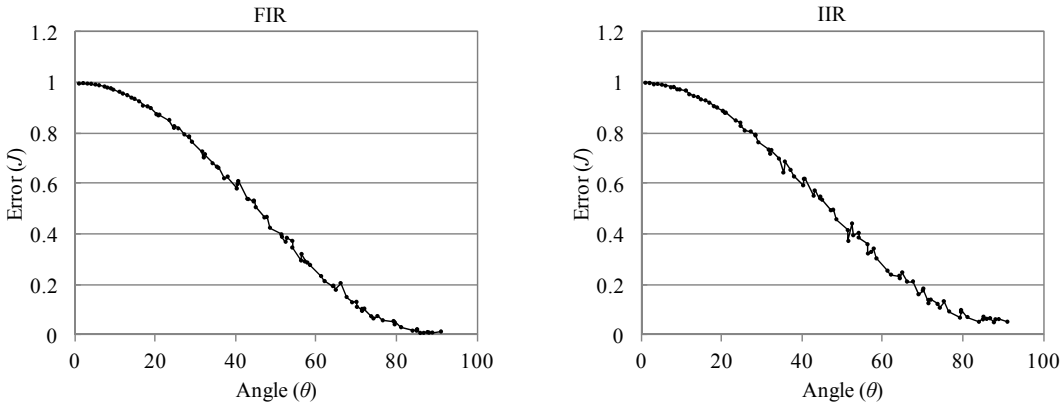

Figure 4.6 Effect of the global correlation between inputs for the FIR (left) and the IIR (right) systems.

4.1.4 Effect of Damping

The third factor that affects the performance of the decoupling approach is the system damping. As explained in previous section, the IIR system requires a much longer time to have its system dynamics decay, and hence the required memory length is much larger than for the FIR system. The fact that QR decomposition has to deal with much larger matrix introduces numerical errors into the result; therefore the accuracy of the decoupled output is lower than the FIR system. System damping affects directly the decay time and hence the optimal memory length, therefore affecting the accuracy of the decoupled output. Using the IIR system in Fig. 1b, the damping ratio of the IIR system is changed from 5% to 90%. As shown in Fig. 4.7, the error of the decoupled output decreases dramatically as the system damping increases. With 20% damping in the IIR system, a comparable accuracy to the FIR system is achieved.

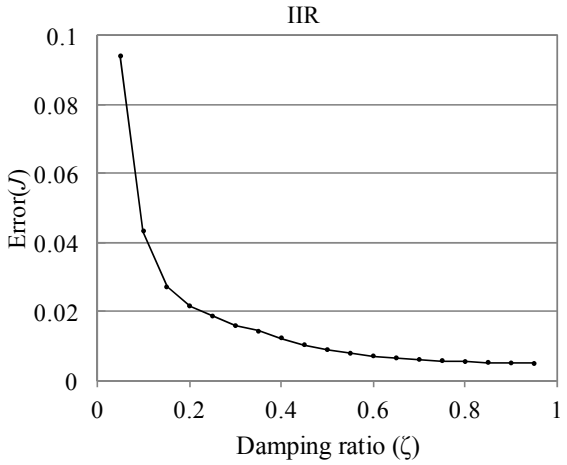

Figure 4.7 Effect of damping ratio for the IIR system.

4.2 ARX-ERA Method for System Identification

As mentioned previously, earthquake records are non-stationary signals and have relatively short duration; therefore, parametric time-domain methods such as time series models are often used. The autoregressive model with exogenous input (ARX) method is adopted herein because of its good performance in such situations, as reported in the literature (Loh and Lin, 1996; Loh and Wu, 2000; Arici and Mosalam, 2003).

Consider a linear time-invariant (LTI) system with input $x(t)$ and output $y(t)$, the input-output relationship can be described in the following linear difference equation (Ljung, 1999):

$$y(t) = b_1 x(t) + b_2 x(t-1) + \cdots + b_{n_b} x(t-n_b+1) + a_1 y(t-1) + \cdots a_{n_a} y(t-n_a) + e(t) \tag{4.10}$$

The output coefficients a_i and input coefficients b_i are the so called the autoregressive and moving average coefficients, respectively. n_a is the number of poles and n_b is the number of zeros plus one. $e(t)$ is a white noise term representing the stochastic system disturbance. In a more compact form, Eq. (4.8) can be written as in Eq. (10), where $A(q)$ and $B(q)$ are polynomials with respect to the backward shift operator q^{-1}.

$$\begin{aligned} A(q)y(t) &= B(q)x(t) + e(t) \\ A(q) &= 1 + a_1 q^{-1} + \cdots + a_{n_a} q^{-n_a} \\ B(q) &= b_1 + b_2 q^{-1} + \cdots + b_{n_b} q^{-n_b+1} \end{aligned} \tag{4.11}$$

Eq. (4.11) is the well-known Auto-Regressive model with exogenous input (ARX). AR refers to the Auto-Regressive part $A(q)y(t)$ and X to the extra input part $B(q)x(t)$. For the SIMO case, the output coefficient $A(q)$ in the ARX model becomes a matrix defined in Eq. (4.12), in which m is the number of outputs.

$$A(q) = \begin{bmatrix} 1 & 1 & \cdots & 1 \\ a_{11}q^{-1} & a_{12}q^{-1} & \cdots & a_{1r}q^{-1} \\ \vdots & \vdots & \ddots & \vdots \\ a_{n_a 1}q^{-n_a} & a_{n_a 2}q^{-n_a} & \cdots & a_{n_a m}q^{-n_a} \end{bmatrix} \tag{4.12}$$

The coefficients of the ARX model can be solved by minimizing the errors or residuals $e(t)$ in Eq.(4.11) by the Least Squares method. In the multiple output case, the norm of the error is minimized (Ljung, 1999), which is

$$\begin{aligned} V(\theta, \hat{y}, \hat{x}) &= \frac{1}{T}\sum_{t=1}^{T}\left(y(t) - \hat{y}(t)\right)^2 \\ \theta &= \left[a_1, \cdots, a_{n_a}, b_1, \cdots, b_{n_b}\right]^{\mathrm{T}} \\ \hat{\theta} &= \arg\min_{\theta} V(\theta, \hat{y}, \hat{x}) \end{aligned} \tag{4.13}$$

where $\hat{y}$ and $\hat{x}$ are measured outputs and inputs in the time interval $t \in [0, T]$, and $\hat{\theta}$ is the solution of the Least Squares problem, which gives the coefficients of the ARX model.

To minimize estimation error, especially when the signal-to-noise ratio is low, the ARX model order is usually set higher than the actual model; therefore, the fitted model may contain more poles and zeros in the transfer function than the actual structure with a certain sampling frequency. To distinguish effectively the structural modes with the noise modes, two noise mode indicators associated with the Eigensystem Realization Algorithm (ERA), namely, the Modal Phase Colinearity (MPC) and the Extended Modal Amplitude Coherence (EMAC) are used (see Juang and Pappa (1985) and Pappa et al. (1993) for more details). Herein, the impulse response function extracted from the fitted ARX model is used as input to the ERA; subsequently, the identified modes with EMAC and MPC values higher than the predetermined thresholds are considered as candidates of structural modes. Then, the stabilization diagram is constructed by increasing the number of retained singular values in the ERA and plotting all the candidates of structural modes in one chart. Based on the idea that a structural mode should exist in systems with various orders, a mode which is identified in at least five realizations of different orders is considered stable and reliable. Among them, the ones with the highest EMAC values are selected as the confirmed modes.

MPC has been previously proposed to work with ARX model without introducing ERA method (Ji et al., 2011), because MPC can be calculated directly with the identified mode shapes. However, there are several drawbacks for using MPC only. First of all, MPC is not applicable for single-input, single-output (SISO) problems because no mode shapes can be identified with only one input and one output. In other words, the MPC values are always equal to 100%. Secondly, MPC is not as sensitive as EMAC to noise modes. Relying on MPC only may not filter out all noise modes. As an illustration, three impulse response functions (h_{12}, h_{22}, h_{32}) of the IIR system shown in Fig. 4.1b with 1% damping are obtained and added with 5% Gaussian white noise. ERA is applied to these impulse response functions and the candidate structural modes are identified by applying either MPC or EMAC; hence two stabilization diagrams are plotted as shown in Fig. 4.8. The solid dots in each stabilization diagram are the final confirmed modes which have the highest EMAC values. Fig. 4.8a shows the result after filtering the noise modes by setting the MPC threshold to 90%; however, the stabilization diagram is not as clean as the one which has EMAC threshold equal to 20%. In fact, after adding 5% noise to the impulse response functions, the MPC values associated with noise modes are still very high, whereas the EMAC values drop down significantly. This simulation shows that combining EMAC and MPC can lead to a more effective method to filter out noise modes from the fitted ARX mode.

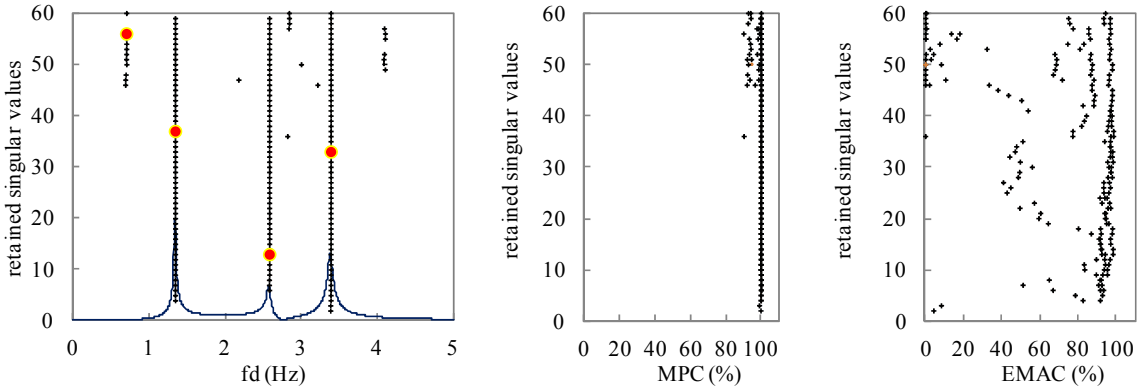

(a) Stabilization diagram with MPC threshold = 90%

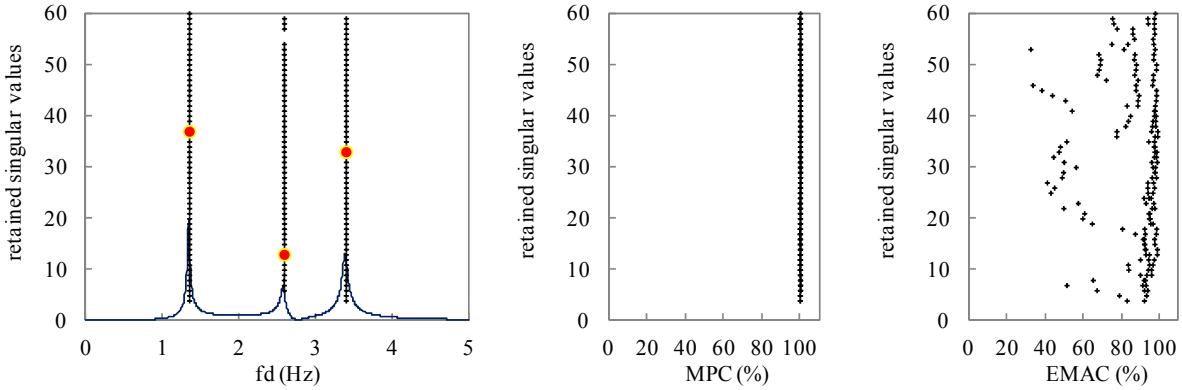

(b) Stabilization diagram with EMAC threshold = 20%

Figure 4.8 Sensitivities of EMAC and MPC to noise modes (5% noise level)

4.3 Application to a Highway Overcrossing Bridge

The Meloland Road Overcrossing (MRO) Bridge is located over Interstate 8, about 10 miles to the east of El Centro, California. The bridge is a reinforced concrete (RC) box-girder bridge with two spans monolithically connected to a single pier. Each span is 104 ft (31.70 m) and the deck is 34 ft (10.36 m) wide. The center pier is about 21 ft (6.40 m) high from the foundation and has a circular cross-section with the diameter of 5 ft (1.52 m). Fig. 4.9 shows the elevation, cross section and plan view of the MRO Bridge. In April, 1978, 26 accelerometers were deployed on the bridge deck, foundation, embankment, and free field. In December 1991, the sensor array was augmented by 6 additional accelerometers. Fig. 4.9 illustrates the sensor locations and directions. A number of earthquake events were captured since the bridge was instrumented. The recorded seismic ground motions and structural responses have been studied extensively in the past. These studies include soil-structural interaction analysis (Crouse and Price, 1993; Zhang and Makris, 2001; Kwon and Elnashai, 2007), seismic analysis (Wilson and Tan, 1988; Saadeghvaziri and Foutch, 1991; Werner, et al., 1993), and system identification (Werner et al., 1987; Arici and Mosalam, 2003), among others. In the following system identification analysis, the data measured during the Calexico Area Earthquake of Nov. 20th, 2008 is utilized. As one of the most recent recorded earthquakes, this one has a small Peak Ground Acceleration (PGA = 0.007 g) and hence is believed to induce only linear response of the bridge-embankment system.

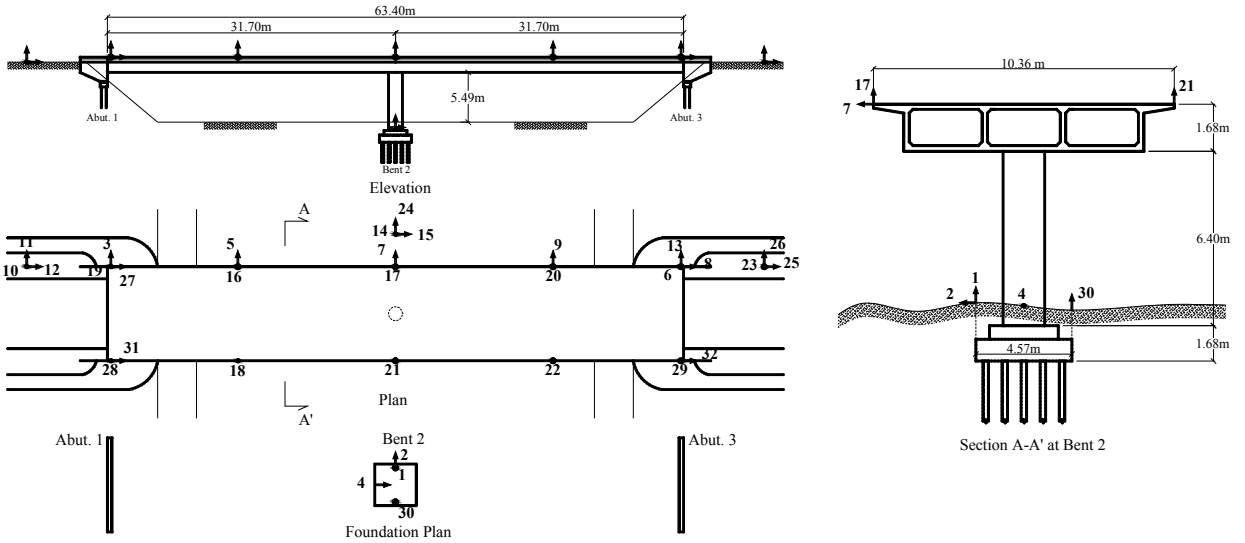

Figure 4.9 MRO Bridge configuration and sensor instrumentation

Inputs and outputs are first identified from the measurement channels. For structures subjected to three-directional ground excitation, the equations of motion (EOMs) are commonly formulated in relative coordinates such that the input term on the right-hand side of the EOM is the product between the mass and the ground acceleration, as shown below:

$$\mathbf{M}\ddot{\mathbf{u}}(t)+\mathbf{C}\dot{\mathbf{u}}(t)+\mathbf{K}\mathbf{u}(t)=-\mathbf{M}\mathbf{G}\ddot{\mathbf{u}}_g(t) \tag{4.14}$$

$$\mathbf{M}=\begin{bmatrix}\mathbf{M}_{xx} & \mathbf{0} & \mathbf{0}\\ \mathbf{0} & \mathbf{M}_{yy} & \mathbf{0}\\ \mathbf{0} & \mathbf{0} & \mathbf{M}_{zz}\end{bmatrix},\mathbf{C}=\begin{bmatrix}\mathbf{C}_{xx} & \mathbf{C}_{xy} & \mathbf{C}_{xz}\\ \mathbf{C}_{yx} & \mathbf{C}_{yy} & \mathbf{C}_{yz}\\ \mathbf{C}_{zx} & \mathbf{C}_{zy} & \mathbf{C}_{zz}\end{bmatrix},\mathbf{K}=\begin{bmatrix}\mathbf{K}_{xx} & \mathbf{K}_{xy} & \mathbf{K}_{xz}\\ \mathbf{K}_{yx} & \mathbf{K}_{yy} & \mathbf{K}_{yz}\\ \mathbf{K}_{zx} & \mathbf{K}_{zy} & \mathbf{K}_{zz}\end{bmatrix}$$

$$\ddot{\mathbf{u}}=\begin{bmatrix}\ddot{\mathbf{u}}_x & \ddot{\mathbf{u}}_y & \ddot{\mathbf{u}}_z\end{bmatrix}^T,\dot{\mathbf{u}}=\begin{bmatrix}\dot{\mathbf{u}}_x & \dot{\mathbf{u}}_y & \dot{\mathbf{u}}_z\end{bmatrix}^T,\mathbf{u}=\begin{bmatrix}\mathbf{u}_x & \mathbf{u}_y & \mathbf{u}_z\end{bmatrix}^T$$

$$\ddot{\mathbf{u}}_g=\begin{bmatrix}\ddot{u}_{gx} & \ddot{u}_{gy} & \ddot{u}_{gz}\end{bmatrix}^T$$

in which the subscripts x, y and z represent three orthogonal directions. $\mathbf{M}$, $\mathbf{C}$, and $\mathbf{K}$ are mass, damping, and stiffness matrices of the structure, respectively. $\mathbf{u}$, $\dot{\mathbf{u}}$ and $\ddot{\mathbf{u}}$ denote the displacement, velocity, and acceleration responses of the structure, respectively. $\ddot{\mathbf{u}}_g$ is the ground acceleration vector which contains three components in x, y, and z directions. $\mathbf{G}$ is a binary matrix which distributes the inertia forces induced by the ground accelerations to corresponding Degrees of freedom (DOFs) on the structure. Therefore, ground acceleration measurements can be used as the input to the system to perform system identification.

In this study, the embankments and the bridge are considered as an integral system subjected to a three-dimensional uniform ground excitation; therefore the three measured ground motion components are used as inputs to the bridge-embankment system, including two horizontal

ground motions, one in the longitudinal direction (channel 15) and the other in the lateral direction (channel 24) of the bridge, and one vertical (channel 14) ground motion. Among these three directions, the lateral and vertical vibration modes of the bridge are the lowest frequency modes and hence are of the most interest. The lateral mode has low frequency because the lateral movement of the deck is essentially driven by the movement of the embankments, which has low stiffness in the lateral direction. Therefore, data from channel 24 and 14 are considered as inputs to the lateral and the vertical systems, respectively. However, further scrutiny of the bridge indicates that while the vertical ground motion contributes only to the vertical response, the lateral ground motion affects not only the lateral responses, but also the vertical responses due to the rotation of the bridge deck in response to the lateral excitation. In this regard, system identification is a SIMO problem in the lateral direction, but a MIMO problem in the vertical direction if the measured data is used as it is. To convert the MIMO problem in the vertical direction into a SIMO problem, the vertical measurements on the bridge deck should be decoupled using the approach proposed in the previous sections.

In what follows, the proposed decoupling method and system identification strategy are first validated through numerically simulated structural response in vertical direction and then applied to identify the modal parameters of the bridge in both lateral and vertical directions using measured data.

4.3.1 Numerical validation of the proposed method

To validate the effectiveness of the proposed decoupling method and the ARX-ERA system identification approach, a linear finite element (FE) model of the MRO Bridge is built in MATLAB (Mathworks, 2009) based on the as-built drawings of the bridge. A lumped mass model is adopted for the bridge. The embankment-abutment system is modeled as two linear springs attached with the embankment mass, one in the lateral direction and the other in the vertical direction. Damping (5%) is added to the first two modes of the system by assuming proportional damping. The measured free field records from channels 24 and 14 during the 2008 Calexico Area Earthquake are used to excite the FE model in the lateral and vertical directions simultaneously to generate coupled response in the vertical direction. Meanwhile, the responses due to only the vertical ground motion (channel 14) are also simulated, which serve as the reference signals for assessing the error of the decoupled result. All measured input and output data are downsampled from 100 Hz to 20 Hz to focus on the frequency range of interest. Before downsampling, digital anti-aliasing filters were applied to remove the frequency contents beyond the Nyquist frequency (10 Hz).

4.3.1.1 Decoupling outputs in the vertical direction

To decouple the vertical responses, as discussed in section 4.1.2, the optimal memory lengths need to be known at various locations on the bridge. The simulated vertical responses at the locations of channel 21, 22, and 29, each corresponds to the locations of the pier top, mid-span and abutment, respectively, are used to determine the corresponding optimal memory lengths. The procedure applied in section 4.1.2 is repeated to search for the optimal memory lengths. Table 4.2 lists the optimal memory lengths and the minimum errors associated with the decoupled responses at the three locations. The angle between the two ground motion inputs is 89 degrees, indicating low correlation between the inputs. Therefore the errors in the decoupled

outputs are expected to be very low based on the discussion in section 4.1.3. These small errors have validated the effectiveness of the proposed decoupling strategy based on the simulated data.

The optimal memory lengths are then applied to decouple the simulated vertical deck responses corresponding to the locations of the ten sensor channels, including two pier top channels (17 and 21), four abutment channels (6, 19, 28 and 29), and four mid-span channels (16, 18, 22 and 20). Fig. 4.10 shows the deck responses from the two mid-span channels (16 and 18) before and after decoupling. Before decoupling, these responses contain contributions from both the vertical and lateral ground motion inputs. The lateral input introduces different response to these two locations of the deck in the vertical direction, which make the total responses look quite different (see Fig. 4.10a). However, after decoupling, the contributions from the lateral input are effectively removed, leaving only the contributions from the vertical input. Therefore, the decoupled responses are almost identical to each other (see Fig. 4.10b).

Table 4.2 Optimal memory lengths and minimum errors of the decoupled outputs for the MRO Bridge

	Location		
	Pier top	Mid-span	abutment
Optimal M	19	47	44
J_{min}	0.098	0.080	0.079

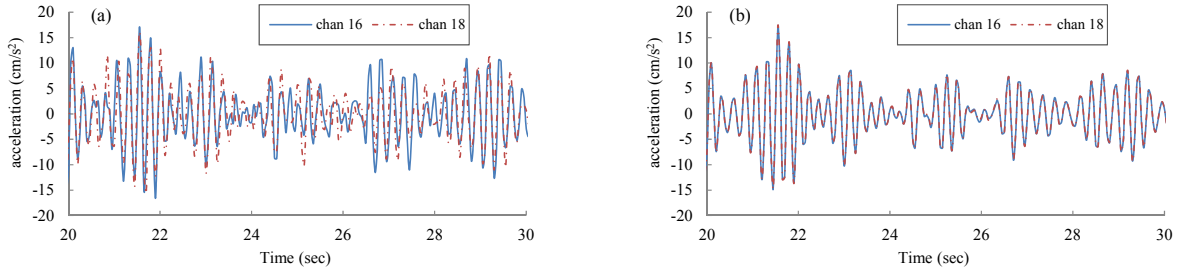

Figure 4.10 The vertical deck responses before (a) and after (b) decoupling using simulated data

4.3.1.2 System identification with the decoupled outputs

With the decoupled outputs which contain only the contribution from the vertical ground input, system identification in the vertical direction can be treated as a SIMO problem. A SIMO ARX model is therefore adopted. Channel 14 is considered as the input and the ten decoupled channels are used as the outputs. n_a and n_b are determined through a trial-and-error process. The ARX model utilizes the same set of poles and zeros to describe both the system dynamics and noise properties. If the values of n_a and n_b are too small, the resulting model may not have enough poles and zeros to represent the system dynamics; on the other hand, overfitting may occur if the values are too large. Herein, in the identification of vertical modes, n_a and n_b are set to 7 and 3, respectively, resulting in a model with 70 poles and 2 zeros. The transfer functions of the ARX model are plotted in Fig. 4.11a.

In the vertical direction, the FE model of the bridge has two modes, which are both symmetric bending modes, under the uniform ground motion inputs, as shown in Fig. 4.11b. The embankment masses move in phase with the deck in the first mode but out-of-phase in the

second mode. The two modal frequencies of the FE model are 4.17 Hz and 5.03 Hz, respectively, as listed in Table 4.3. Apparently, within the range of the sampling frequency, which is 20 Hz after downsampling, only 4 of the poles correspond to true system dynamics while the rest are noise modes. The EMAC and MPC associated with the ERA method are then used to automatically filter out these noise modes and find the true modal properties, as shown in the stabilization diagram in Fig. 4.11a. In this case, the threshold values of EMAC and MPC are set to 20% and 90%, respectively. Both vertical bending modes are picked up by the stabilization diagram with high accuracy, with errors of natural frequency less than 0.5%. The clear stabilization diagram, with only true modes retained in the plot, indicates the effectiveness of the combined usage of EMAC and MPC in filtering the noise modes in the fitted ARX model. Meanwhile, both identified mode shapes match with the FE model very well as indicated by the Model Assurance Criteria (MAC) values (Allemang and Brown, 1982). The results are summarized in Table 3. This section has demonstrated that the proposed decoupling approach and the ARX-ERA method are effective for system identification using highly coupled output signals.

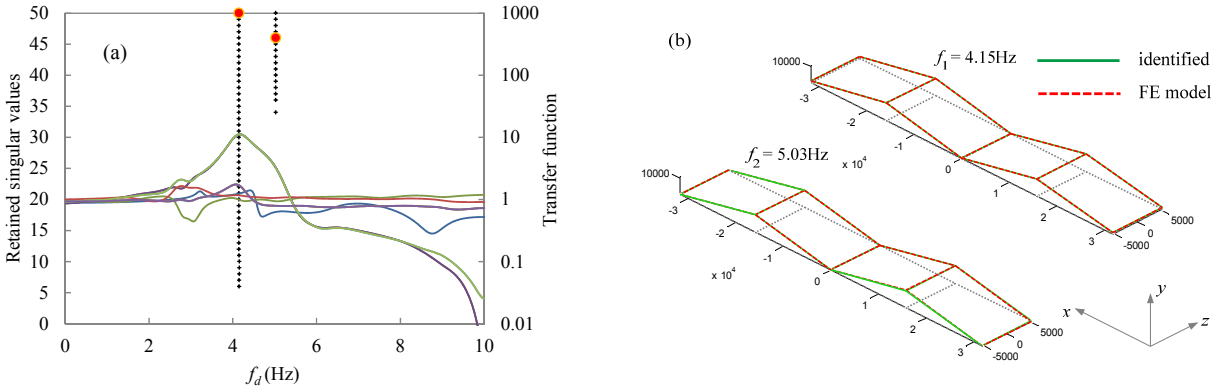

Figure 4.11. Identification result with simulated data: (a) stabilization diagram; (b) modal frequencies and mode shapes.

Table 4.3. Accuracy of the identified modal parameters with simulated data

Mode	Natural Frequency (Hz)			Mode shape (MAC)
	FE Model	Identified	Error	
1	4.1671	4.1488	-0.44%	1.0000
2	5.0373	5.0269	-0.21%	0.9999

4.3.2 Decoupling and system identification with measured structural response

System identification is carried out independently in the lateral and vertical directions using measured data. In the lateral direction, as mentioned previously, the lateral responses are induced only from the lateral ground motion and hence a SIMO ARX model is used, with channel 14 as the input and channels 11, 3, 5, 7, 9, 13, and 26 as the outputs. Note that channels 11 and 26 which measure the embankment responses are included herein, because the bridge and the embankments are treated as an integral system subject to a single uniform ground excitation. In the identification of lateral modes, n_a and n_b are set to 2 and 3, respectively, resulting in a model with 14 poles and 2 zeros. In this case, the threshold values of EMAC and MPC are set to 20% and 90%, respectively. A lateral bending mode at 3.13 Hz associated with 4.9% damping is identified. The mode shape is depicted in Fig. 4.13b.

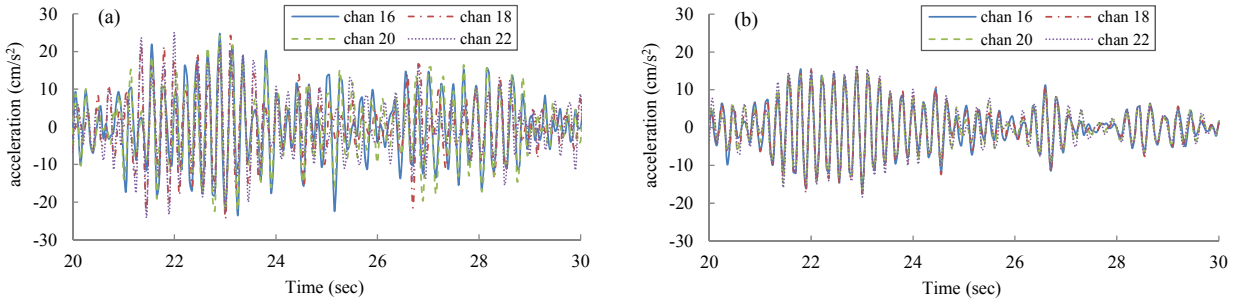

Figure 4.12. The vertical deck responses before (a) and after (b) decoupling using measured data

In the vertical direction, the procedure described in section 4.3.1.1 and the optimal memory lengths listed in Table 4.2 are applied to decouple the measured structural responses from the ten vertical sensor channels. Fig. 4.12 shows the deck responses from the four mid-span channels before and after decoupling. Similar to Fig. 4.10, one indication of the effectiveness of the decoupling method is that these records become quite similar to each other after the components contributed from the lateral input have been removed. With the decoupled vertical outputs, a SIMO ARX model is used to fit the input-output data. n_a and n_b are also determined as 2 and 3, respectively, resulting in 20 poles and 2 zeros in this case. The stabilization diagram is shown in Fig. 4.14a, in which the EMAC and MPC thresholds are again set to 20% and 90%, respectively. Again, a clear stabilization diagram is obtained with all noise modes filtered out effectively using the proposed method. One asymmetric bending mode at 3.13 Hz and one symmetric bending mode at 4.51 Hz are identified as shown in Fig. 4.14b. The associated damping ratios are 3.3% and 2.8%, respectively.

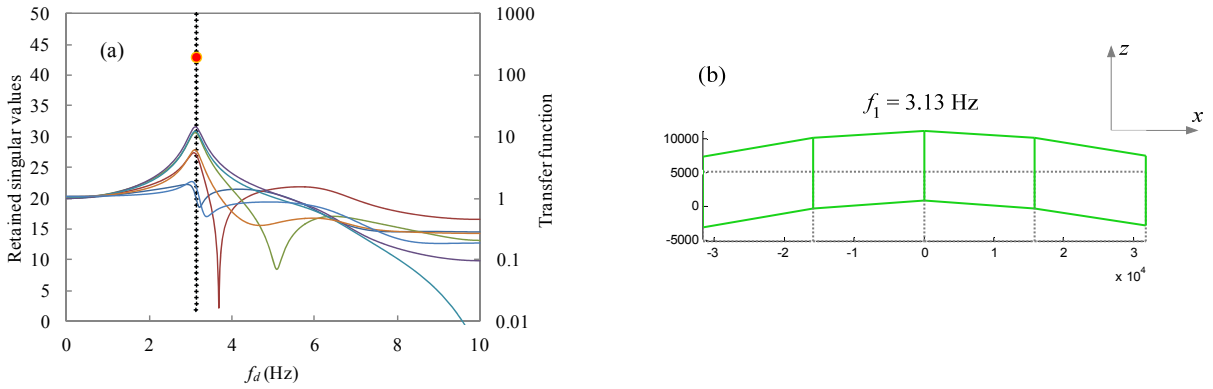

Figure 4.13 Identification result in the lateral direction: (a) stabilization diagram; (b) modal frequency and mode shape.

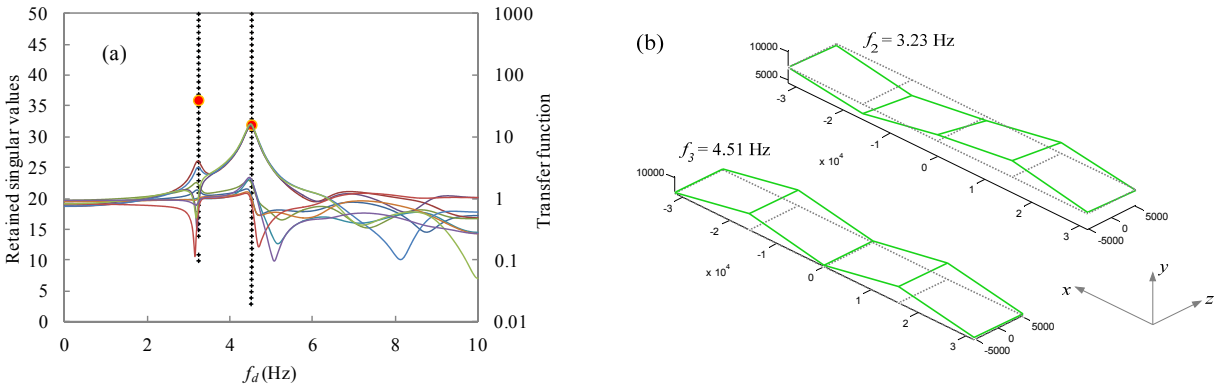

Figure 4.14 Identification result in the vertical direction: (a) stabilization diagram; (b) modal frequencies and mode shapes.

Comparing between the results with the simulated (Fig. 4.11) and measured responses (Fig. 4.14), one can observe that both cases have identified the first symmetric bending mode which has the embankment mass moving in phase with the bridge deck. However, in the latter case, the second symmetric bending mode is not identified whereas an additional asymmetric bending mode is identified. The difference can be attributed to the discrepancy between the FE model and the real bridge. As indicated previously, the FE model is built based on the as-built drawing and many parameters such as the embankment mass and the spring stiffness can have some uncertainties. For example, the stiffness of the embankment could be higher than the FE model such that the second symmetric bending mode exists in much higher frequency range for the real bridge. In addition, the 3.23 Hz asymmetric bending mode indicates that, unlike the FE model, the bridge is not perfectly symmetric, because otherwise the asymmetric mode could not be excited by the uniform vertical ground excitation. Note that the asymmetric mode does not have identical shapes along the two sides of the bridge deck in the longitudinal direction, which supports the speculation that the bridge is not symmetric. In contrast, the 4.51 Hz symmetric bending mode has quite similar shape along the two sides of the deck. One possible reason could

be that during earthquakes, the center pier was not providing identical bending stiffness to the deck in the longitudinal direction due to uneven support at the bottom of the pier.

4.4 Summary

In this chapter, a new system identification strategy is proposed for civil engineering structures subjected to multiple earthquake inputs that lead to strong coupling in the response signals. By decoupling the outputs, the contribution from each individual input can be separated. This separation leads to the conversion of the MIMO system identification into SIMO problems, which are computationally less complex and have potential to yield more accurate results. The accuracy of the decoupling approach has been comprehensively examined by focusing on three critical factors: the memory length, the input correlation, and the system damping. By selecting the appropriate memory length, both FIR and IIR systems can be identified with high accuracy in the decoupled outputs. The global correlation of the inputs, rather than the local correlation, affects the accuracy of decoupled outputs. Increasing the global correlation of inputs will decrease the accuracy. For the IIR system with 5% damping, when the input angle is larger than 80 degrees, satisfactory result can be achieved. Finally, systems with higher damping can yield higher accuracy in the result.

A parametric system identification method which combines the ARX and the ERA methods has been proposed for seismic measurements. The noise mode indicators associated with the ERA method, including the EMAC and MPC, are utilized to filter out the noise modes in the fitted ARX model, enabling accurate and automatic system identification with ARX. The combined usage of EMAC and MPC has been found beneficial due to the lack of sensitivity of the MPC to noise modes compared with the EMAC.

Finally, the effectiveness of the proposed system identification strategy approach has been demonstrated using the Meloland Road Overcrossing Bridge with both simulated and measured seismic measurements. The dynamic modes in lateral direction is directly identified as a SIMO problem using the proposed ARX-ERA method, while in the vertical direction, the decoupling strategy was first applied to remove the contribution from the lateral input to the vertical outputs, allowing SIMO identification in the vertical direction. One lateral bending mode and two vertical bending modes were successfully identified. The identified modal parameters will be used in the next chapter to calibrate the linear model of the bridge as a part of a model calibration procedure. The results reported in this chapter established a firm foundation for high accuracy structural characterization, which is an essential component for high-fidelity fragility analysis and seismic risk assessment.

FRAGILITY FUNCTION UPDATING WITH HYBRID SIMULATION

In this chapter, a two-stage approach is proposed to derive improved fragility functions for engineering structures. In the first stage, the linear and nonlinear parameters of the finite element model are calibrated using measured earthquake responses and cyclic testing data; analytical fragility functions are then generated with the calibrated model. In the second stage, Bayesian updating is employed to update the derived fragility functions using hybrid simulation experiments. Fragility functions are generated for the Meloland Road Overcrossing (MRO) Bridge considering four cases which represent an increasing level of data availability. Finally, a hypothetical regional seismic risk assessment is carried out with the four sets of fragility functions for Imperial County, California. The methodology proposed in this chapter provides a systematic way of improving fragility estimation incorporating hybrid simulation data.

5.1 Fragility Functions

Fragility functions are often formulated using a two-parameter log-normal distribution functions (Shinozuka et al., 2000; Nielson, 2005) with the following mathematical form:

$$P_f = P\left(\frac{S_d}{S_c} \geq 1\right) = \Phi\left[\frac{\ln\left(S_d/S_c\right)}{\sqrt{\beta_d^2 + \beta_c^2}}\right] \tag{5.1}$$

where Φ is the Cumulative Distribution Function (CDF) of the standard normal distribution; S_d and S_c are the structural demand and the structural capacity, respectively, and β_d and β_c are the associated dispersions. When the fragility function is expressed with respect to ground motion intensity (denoted by *x*), such as Peak Ground Acceleration (PGA) or Spectral Acceleration (SA), the mathematical form can be expressed as (Koutsourelakis, 2010):

$$P_f = F_X\left(x; \mu, \sigma\right) = \frac{1}{2} + \frac{1}{2} erf\left[\frac{\ln\left(x\right) - \mu}{\sigma\sqrt{2}}\right] \tag{5.2}$$

where *erf* is the error function, $\sigma = \sqrt{\beta_d^2 + \beta_c^2}$ is the dispersion, and μ is the natural logarithm of the median ground motion intensity, which corresponds to when $S_d / S_c = 1$.

5.2 General Concept of Bayesian Updating

The Bayesian approach provides a systematic way of updating existing knowledge of a random variable with new information. Essentially, the parameters describing a random variable, such as the mean, the variance, the skewness, etc, are also treated as random variables (denoted by θ) and are modeled with prior distribution (demoted by $f'(\boldsymbol{\theta})$) based on existing knowledge. Meanwhile, the newly obtained information, such as observations or experimental outcome (denoted by $\boldsymbol{\varepsilon}$), is formulated into a likelihood function (denoted by $L(\boldsymbol{\varepsilon}|\boldsymbol{\theta})$), which is simply the conditional probability of obtaining a particular experimental outcome given the parameters θ. According to Bayes' theorem, the updated distribution of the parameters, called the posterior

distribution (denoted by $f''(\boldsymbol{\theta})$) which combines the existing knowledge and the newly obtain information, is given as follows (Ang and Tang, 1975):

$$f''(\boldsymbol{\theta}) = \kappa L(\boldsymbol{\varepsilon} \mid \boldsymbol{\theta}) f'(\boldsymbol{\theta}) \tag{5.3}$$

where $\kappa = \left[\int_{-\infty}^{\infty} L(\boldsymbol{\varepsilon} \mid \boldsymbol{\theta}) f'(\boldsymbol{\theta}) \, d\boldsymbol{\theta} \right]^{-1}$ is a normalizing constant required to make $f''(\boldsymbol{\theta})$ a proper probability density function. With the posterior distribution, one can either estimate the confidence interval of the random variables or have a point estimate using the mean or mode of the posterior distribution.

5.3 Bayesian Updating of Fragility Functions

To update the fragility functions shown in Eq. (5.2) using the above Bayesian framework, the random variables θ that need to be updated are μ and σ, i.e. the natural logarithm of the mean ground motion intensity and the dispersion, respectively. More specifically,

$$\begin{aligned} \theta_1 &= \mu \\ \theta_2 &= \sigma \end{aligned} \tag{5.4}$$

The existing knowledge about μ and σ is from the analytical fragility function

$$P_f = F_X(x; \mu_a, \sigma_a) = \frac{1}{2} + \frac{1}{2} erf\left[\frac{\ln(x) - \mu_a}{\sigma_a \sqrt{2}} \right] \tag{5.5}$$

where subscript *a* means analytical value. In this proposed approach, μ_a and σ_a are considered as the mean values of θ_1 and θ_2 in the prior distributions. θ_1 is assumed to follow normal distribution with known mean $\mu_{\theta_1} = \mu_a$ and unknown variance $\sigma_{\theta_1}^2$. One can assign a deterministic value to $\sigma_{\theta_1}^2$ depending on the prior knowledge about μ_a. For example, if the derivation process of fragility functions is believed to lead to a reliable estimation of μ_a, a small $\sigma_{\theta_1}^2$ can be used or a large $\sigma_{\theta_1}^2$ if otherwise. A more flexible alternative is modeling $\sigma_{\theta_1}^2$ with a hyperprior distribution. For the sake of mathematical convenience, a conjugate hyperprior distribution is adopted here, i.e. an inverse gamma distribution with parameters a_1 and b_1 is selected herein for $\sigma_{\theta_1}^2$ (Lynch, 2007; Robert, 2007), i.e.

$$1/\sigma_{\theta_1}^2 \sim \Gamma(a_1, b_1) \tag{5.6}$$

By marginalizing the normal distribution of θ_1 over the inverse gamma distribution of $\sigma_{\theta_1}^2$, the prior distribution of θ_1 becomes a student's *t*-distribution with parameters λ and ν:

$$P(\theta_1 \mid \lambda, \nu) = \frac{\Gamma\left(\frac{\nu+1}{2}\right)}{\Gamma(\nu/2)}\left(\frac{\lambda}{\pi\nu}\right)^{1/2}\left[1+\frac{\lambda\left(\theta_1-\mu_{\theta_1}\right)^2}{\nu}\right]^{-\frac{\nu+1}{2}} \tag{5.7}$$

in which $\nu = 2a_1, \lambda = a_1/b_1$. μ_{θ_1} is the mean of the normal distribution of θ_1 as mentioned previously and now becomes the mode (also mean if ν >1) of the student's t-distribution, so the updated θ_1 is taken as the mode of the posterior distribution, as will be described in subsequent section.

Meanwhile, the prior distribution of θ_2, i.e., the dispersion σ of fragility function, is assumed to follow a gamma distribution with parameters a_2 and b_2, i.e.

$$P(\theta_2 \mid a_2,\ b_2) = \theta_2^{a_2-1}\frac{e^{-\theta_2/b_2}}{b_2^{a_2}\Gamma(a)} \tag{5.8}$$

The selection of gamma distribution is to ensure the dispersion is positive. The mean value of the gamma distribution is $a_2 \cdot b_2$ and is equal to σ_a . Although other distributions may also be appropriate, it is beyond the scope of this paper to illustrate the performance of various prior distributions. The two parameters θ_1 and θ_2 can be considered independent to each other; therefore, the joint prior distribution is the product of the two prior distributions, namely,

$$f'(\boldsymbol{\theta}) = P(\theta_1 \mid \lambda, \nu)\cdot P(\theta_2 \mid a_2,\ b_2) \tag{5.9}$$

The new information about the fragility functions is incorporated into the likelihood function, which is formulated in Eq. (5.10) by treating each hybrid simulation outcome as a realization of a Bernoulli experiment (Shinozuka et al., 2000).

$$L(\varepsilon \mid \theta) = \prod_{i=1}^{n}\left(1-F_X(x_i;\theta)\right)^{1-\varepsilon_i} F_X(x_i;\theta)^{\varepsilon_i} \tag{5.10}$$

The experimental result ε_i is expressed as a binary number. For each limit state, if experimental result exceeds the predefined limit state, ε_i = 1; otherwise, ε_i = 0. $F_X(x_i;\theta)$ is the fragility function given in Eq. (2), which is the probability of exceeding a certain limit state under a specific ground motion intensity x_i .

The posterior distribution, which is the updated prior distribution incorporating new data, is proportional to the product of the prior distribution and the likelihood function, as shown in Eq. (5.3). If a point estimation of the fragility function is desired, such as in the regional risk assessment where fragility functions are used to determine the damage state of structures, the updated μ and σ can be estimated using the mode and the mean of the posterior distributions. The posterior distribution formulated in this study has a complicated mathematical form and is not analytically tractable. In such cases, to calculate the mode and mean of the posterior

distributions, the Markov Chain Monte Carlo (MCMC) sampling techniques are generally applied to draw samples from the posterior distribution. The mode and the mean are then calculated directly from the drawn samples.

In what follows, the two-stage strategy for improved fragility function estimation as described in the introduction section is verified through an application to the Meloland Road Overcrossing (MRO) Bridge. To demonstrate the approach, fragility functions are generated for the MRO Bridge considering four cases which represent an increasing level of data availability: *Case 1* – no data available, fragility functions are derived purely based on the uncalibrated numerical model; *Case 2* – data is only available for bridge model calibration; *Case 3* – hybrid simulation experiments are carried out at the Multi-Axial Full-Scale Sub-Structured Testing and Simulation (MUST-SIM) facility at NEES@UIUC to update the fragility functions derived with the uncalibrated model in *Case 1*; and *Case 4* – bridge model is calibrated and the derived fragility functions are further updated using hybrid simulation experiments.

5.4 The Initial FE Model of the MRO Bridge

In engineering practice, when no data is available (neither field measurement nor lab experiment) for model calibration, models that are as representative as possible are developed. In this study, Zeus-NL (Elnashai et al., 2004) is selected because of its effectiveness in determining the dynamic response of RC structures (see, for example, Madas and Elnashai, 1992; Izuddin et al., 1994; Lee and Elnashai, 2001). In addition, to have realistic model of the shear spring for the pier, Response-2000 (Bentz, 2000), a widely adopted software tool for shear strength analysis of RC members, is employed to derive the primary curve of the pier implemented in the model. Moreover, to model the embankment-abutment system, the pushover curve from a detailed 3-D finite element analysis of the embankment-abutment component using OpenSees (McKenna and Fenves, 2001) reported in Kwon and Elnashai (2007) is adopted to find the primary curve of the embankment-abutment shear spring. Therefore, the modeling process of the initial model of the MRO Bridge represents a typical and comprehensive procedure for modeling a highway bridge structure when experimental and field data is not available. Below, the model of each component of the bridge is described.

5.4.1 Modeling of Bridge Deck

As illustrated in Fig. 5.1, a lumped mass model is adopted for the bridge. In the design of bridge structures, the bridge piers and abutments are designed to undergo inelastic deformation during large earthquakes, while the superstructure is designed to have only elastic response through a capacity design (Aviram et al., 2008). Therefore, the bridge deck is assumed linear and is modeled with 16 beam elements. The multi-cell box-girder cross section is equivalently modeled with the RCHRS (reinforce concrete hollow rectangular section) in Zeus-NL. The dimension of the RCHRS is optimized such that the sectional properties match the actual cross section. To model the torsional behavior of the deck, part of the mass is lumped along the center line and the rest along the edge of the deck. The ratio between the center and edge masses is determined by the mass moment of inertia.

5.4.2 Modeling of Embankment-Abutments and Piles

The MRO Bridge has monolithic abutments which allow force to be transferred between the bridge and the embankments. The embankment-abutment system is therefore modeled as a

nonlinear spring attached with the embankment mass. Kwon and Elnashai (2007) conduct a 3D nonlinear finite element analysis for the embankment-abutment system of the MRO Bridge, in which the embankment, wing wall, abutment and pile are all included in the model. From the pushover curve from this analysis, the displacements at cracking, yielding and ultimate states and the corresponding stiffness values are identified, as shown in Table 5.2, and are used in the primary curve for the nonlinear spring in this initial model. The embankment mass is calculated based on the elastic stiffness of the spring and the first identified natural period in the transverse direction.

The MRO Bridge site has a deep soft alluvium profile and hence the effect of SSI (Soil-Structure Interaction) cannot be ignored (Kwon and Elnashai, 2007). A linear spring is adopted to model the non-rigid connection to the ground at the bottom of the bridge pier. The linear stiffness value of the pile group estimated from the nonlinear finite element analysis by Kwon and Elnashai (2007) is used for modeling the linear spring.

5.4.3 Modeling of Bridge Pier

To account for both the flexural and shear deformation of the bridge pier, a flexure-shear interaction model is adopted (Lee and Elnashai, 2001), in which a fiber-based beam element with displacement-based formulation and a shear spring are connected in series to model the flexural and shear behaviors, respectively, as shown in Fig. 5.1. The RCCS (Reinforced Concrete Circular Section) in Zeus-NL is used for the beam element to model the cross section of the pier, which is also depicted in Fig. 5.1. The beam element is divided into 8 sub-elements with refined mesh at the two ends in order to quantify reliably the inelastic response. The compressive strength of the concrete is 20.68 Mpa (3000 psi) and the reinforcement is Grade 60, with yield strength of 413.69 Mpa (60 Ksi). The hysteretic model of the shear spring is defined by a quatrilinear primary curve that accounts for the cracking, yielding, and ultimate states. For this initial FE model, Response 2000 (Bentz, 2000) is utilized to find the primary curve of the pier which is then idealized as the quatrilinear primary curve.

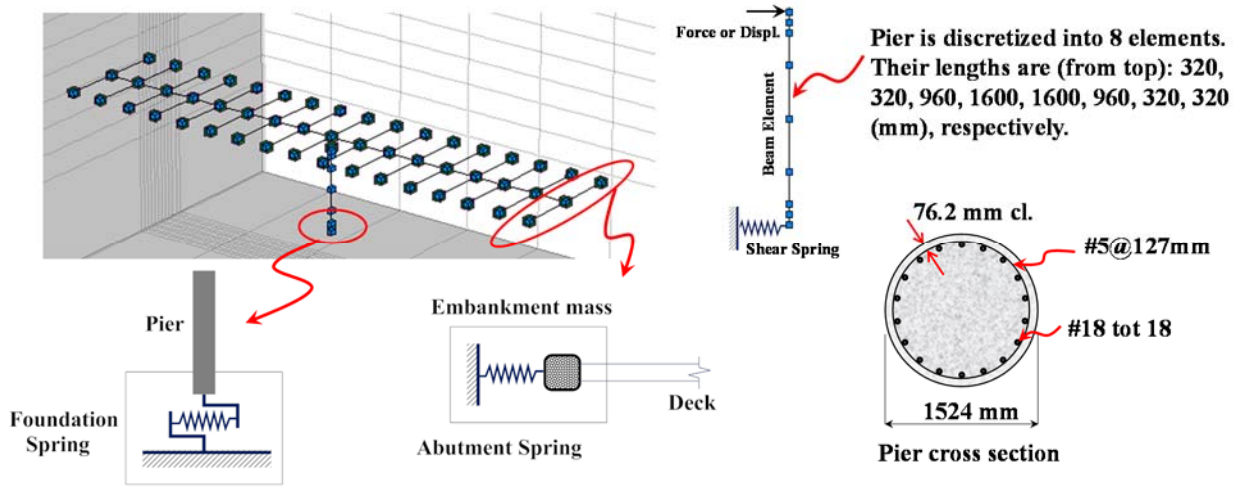

Figure 5.1 Finite element model of MRO Bridge (Zeus-NL) and pier cross section

5.5 Model Calibration

A reliable FE model is critical for the fidelity of analytical fragility functions. The initial FE model has been established without knowledge about the actual behavior of the bridge. Therefore, large uncertainties may exist in the model especially in the nonlinear components, such as the bridge pier and the abutments. The sensor measurements of the bridge during past earthquakes, such as the structural response and the free field measurements, provide great opportunity for understanding the real dynamic behavior of the bridge, which can be used to calibrate the initial FE model such that it generates realistic data for fragility analysis.

The initial FE model of the MRO Bridge is calibrated in a step by step manner. Firstly, the nonlinear pier model is calibrated with cyclic test data. After that, the linear parameters of the bridge deck and the abutment-embankment model are calibrated through model updating based on the identified dynamic properties including natural frequencies and mode shapes. Finally, the nonlinear parameters of the abutment spring are calibrated with the acceleration response time history captured during the 1994 Northridge earthquake. Details of each step will be described in the following sections.

Figure 5.2 Small scale RC pier specimens

5.5.1 Calibration of Pier Model with Cyclic Test

A cyclic test is conducted with one of the nine 1/25th scale RC pier specimens, as shown in Fig. 5.2. The rest of the specimens will be used in subsequent hybrid simulation tests. The use of small scale specimens, rather than full or large scale ones in both cyclic tests and hybrid simulation tests, is justified by similar experiments (Holub, 2009), which showed that small scale RC piers, with cautious design of the microconcete and rebar, were able to capture similar behavior of large scale specimens in terms of all measures of load, deformation and absorbed energy. Therefore, the mix of microconcete is carefully designed to achieve correct balance of compressive strength, tensile strength and stiffness. Following the design guideline proposed by Holub (2005), Type III cement is adopted to expedite the fabrication. Locally available limestone sand was used and graded for later recombination. To avoid excessive tensile strength, the aggregate material below the US #100 sieve [0.15 mm] is removed. Annealed thread rod is used for small scale rebar. An appropriate heat treatment, i.e. annealing at 538 ˚C (1000 ˚F) for one hour, is applied to the threaded rod to achieve satisfactory yield point (Holub, 2009). In addition, the 1/5th-scale Local and Boundary Condition Box (LBCB) of the MUST-SIM facility at the University of Illinois (Elnashai et al., 2004) used for the small scale specimen is an exact replica of the large scale LBCB and allows for very precise execution and measurement of displacements and forces. All the above considerations led to successful cyclic and hybrid tests with the small scale specimens.

The lateral load is defined by 8 drift ratios, including 0.5%, 1%, 2%, 3%, 4%, 5%, 6% and 7%. Each drift level is repeated for 3 full cycles. A constant gravity load calculated from the initial FE model is applied vertically throughout the test. In the cyclic test, the top and bottom of the pier are fixed against rotation. The load-drift curve from the test is shown in Fig. 5.3, in which the measured force has been converted to the prototype scale. Severe pinching effect is observed, indicating large shear deformation. Fig. 5.3(a) compares the load-drift curves between the initial FE model and the cyclic test. The maximum strength is predicted relatively well in the initial FE model; however, stiffness degrades much sooner than in the cyclic test. Moreover, the elastic stiffness is overestimated in the initial FE model. Pinching behavior is not fully captured, resulting in larger energy dissipation capability in the model.

The initial FE model of the pier is calibrated according to the cyclic test by tuning the parameters of the shear spring of the pier model, including the stiffness and displacement values of the cracking, yielding and ultimate states. The parameters are shown in Table 5.2 before and after calibration. Fig. 5.3(b) shows that after calibration, the FE model predicts well the elastic stiffness, stiffness degradation and strength.

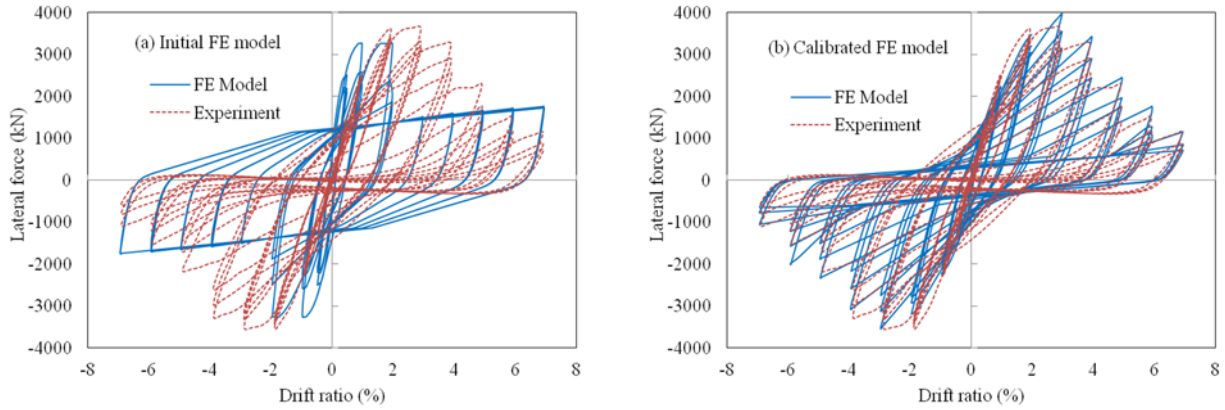

Figure 5.3 Comparison of load-drift curve between the FE model and the cyclic test: (a) Initial FE model; (b) Calibrated FE model

5.5.2 Linear Model Updating of Deck and Abutments

Sensitivity based model updating approach is applied to update the linear parameters of the bridge deck and the abutment-embankment model. The basic idea is that an objective function is formulated containing the residual terms representing the difference between the FE model and real structure. The objective function is then minimized by varying a set of structural parameters using optimization algorithms.

Sensitivity analysis is firstly conducted to select the parameters to which the natural frequencies are mostly sensitive. The elastic modulus (E_d) and the lumped masses at the center line (m_{dc}) and the edge (m_{de}) of the deck, the lumped mass of the center pier (m_p) as well as the linear stiffness of the abutment (K_a) are selected as the updating parameters. The initial values of these parameters are shown in Table 2. Eq. (5.11) gives the objective function which contains the residual terms for natural frequencies and mode shapes (Jang et al., 2012).

Table 5.1 Identified natural modes and linear model updating result

Mode	Natural frequency error		Mode shape (MAC)		Damping ratio
	Before updating	After updating	Before updating	After updating	identified
1	-9.08%	0.03%	0.910	0.955	5.64%
2	4.01%	-0.85%	0.983	0.983	3.35%
3	11.36%	6.00%	0.967	0.967	4.27%

$$F(x)=\sum_{i=1}^{N_f} w_{f_i}\left(\frac{f_{ai}-f_{ei}}{f_{ei}}\right)^2+\sum_{i=1}^{N_m} w_{m_i}\frac{\cos^{-1}\left(\sqrt{MAC_i}\right)}{(\pi/2)} \tag{5.11}$$

$$MAC_i=\frac{\left(\phi_{ai}^T\phi_{ei}\right)^2}{\left(\phi_{ai}^T\phi_{ai}\right)\left(\phi_{ei}^T\phi_{ei}\right)} \tag{5.12}$$

where f_{ai} and f_{ei} denotes the analytical and experimental (identified) natural frequencies, respectively. ϕ_{ai} and ϕ_{ei} are the associated mode shape vectors. w_{f_i} and w_{m_i} are the weighting factors applied to the natural frequency residuals and the mode shape residuals, respectively. In this analysis, the identified three natural frequencies and mode shapes are included in the objective function. Noticing that the discrepancy in natural frequencies are larger than in the mode shapes and the error in the first natural frequency is higher than in the other modes (see Table 5.1), the biggest weighting factor was assigned to the first natural frequency residual in Eq. (5.11). The values of w_{f_i} considered are 5.0, 0.1, 0.2 and the values of w_{m_i} considered are 0.05, 0.03, and 0.02 for the first three modes, respectively. MAC_i is the Modal Assurance Criteria (Allemang and Brown, 1982) which measures the similarity between two mode shape vectors. The second term in Eq. (5.11) is the normalized angle between the two mode shape vectors, which is more sensitive to the change of mode shapes than the *MAC* itself, and hence performs more effectively (Jang et al., 2012).

Optimization is carried out using the Sequential Quadratic Programming (SQP) algorithm. The updated parameters are given in Table 5.1. The updated model has better representation of the real structures in terms of both natural frequencies and mode shapes.

5.5.3 Nonlinear Calibration of Abutment-Embankment Model

The nonlinear model of the abutment-embankment mode is critical for the FE model of the MRO Bridge. Nonlinear finite element analysis (Kwon and Elnashai, 2007) indicates that the embankment yields at small displacement in the transverse direction, leading to significant stiffness reduction. The embankment is therefore much softer than the deck such that the deck motion is driven by the embankment movement. Fig. 5.4(a) depicts the simulated deck response with linear abutment-embankment model and the measured deck response during the 1994 Northridge earthquake, the largest earthquake recorded by the instrumentation so far. With linear

abutment model, the response contains high frequency components which do not exist in the measurement. Moreover, the peak response, which is the most important quantity for subsequent fragility analysis, is greatly underestimated.

Table 5.2 Structural parameters in linear and nonlinear model updating

Linear model updating of deck and embankment-abutment					
Parameters	$E_d\left(N/mm^2\right)$	$K_a\left(N/mm\right)$	$m_{dc}\left(10^3 Kg\right)$	$m_{de}\left(10^3 Kg\right)$	$m_p\left(10^3 Kg\right)$
Initial	22000	741000	29.65	6.448	28.02
Updated	20900	930000	31.13	6.77	27.79

Nonlinear model calibration of Pier						
Parameters	$\Delta_{cr}\left(mm\right)$	$\Delta_y\left(mm\right)$	$\Delta_m\left(mm\right)$	$K_{cr}\left(N/mm\right)$	$K_y\left(N/mm\right)$	$K_m\left(N/mm\right)$
Initial	0.39	4.88	17.57	3082.3	290.9	64.2
Updated	2.5	18.0	137.50	231.5	63.47	23.54

Nonlinear model calibration of embankment-abutment						
Parameters	$\Delta_{cr}\left(mm\right)$	$\Delta_y\left(mm\right)$	$\Delta_m\left(mm\right)$	$K_{cr}\left(N/mm\right)$	$K_y\left(N/mm\right)$	$K_m\left(N/mm\right)$
Initial	6.0	10.0	1000.0	741000	300	200
Updated	5.2	25.0	1000.0	930000	120	67

The uncalibrated nonlinear model has better performance than the linear mode in that the response shows similar period with the measurement, as illustrated in Fig. 5.4(b). However, the peak response is still underestimated. Similar to the calibration of the bridge pier model, the calibration of the abutment-embankment model is carried out by adjusting the primary curve of the shear spring. The parameters of the shear spring before and after calibration are shown in Table 5.2. The deck response of the calibrated model in Fig. 5.4(c) shows the calibrated model is able to capture important features including the period and the peak response.

5.6 Derivation of Analytical Fragilities (Case 1 and Case 2)

Two sets of analytical fragility functions are derived in this section, one with the initial FE model (*Case 1*) and the other with the calibrated model (*Case 2*) as described in previous section. The capacity is estimated directly using the cyclic testing data and the demand is obtained through nonlinear time history analyses. Uncertainties are considered for both capacity and demand.

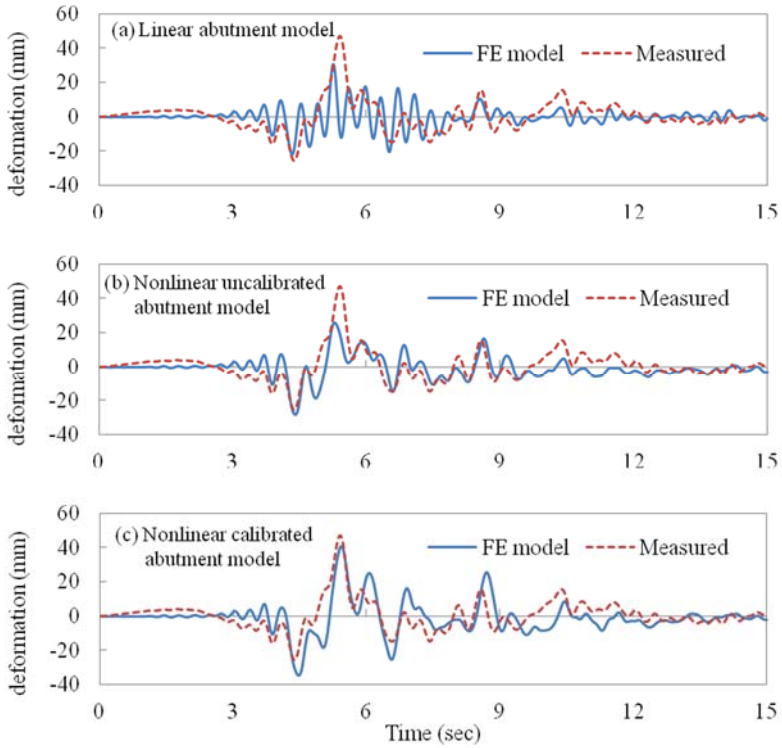

Figure 5.4 Comparison between the simulated and measured deck responses: (a): linear abutment model; (b) nonlinear uncalibrated abutment model; (c): nonlinear calibrated abutment model

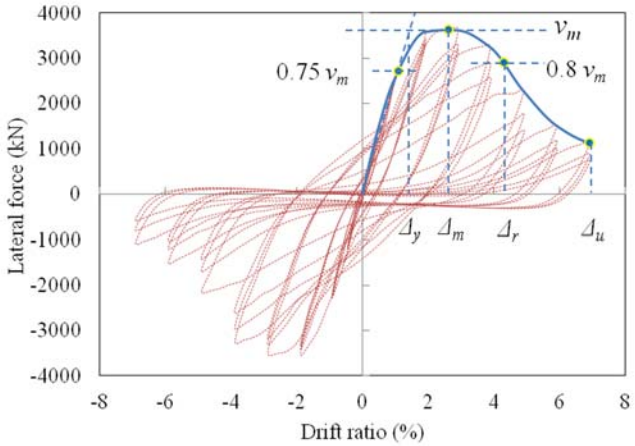

Figure 5.5 Damage limit states of the MRO Bridge

5.6.1 Damage Limit States (Capacity)

Damage limit states are defined in terms of the drift of the bridge pier in the transverse direction. Four damage limit states are identified using the cyclic testing data. Finite element analysis shows that during earthquake excitation, the rotation at the top of the pier is small. Therefore, the cyclic testing of the pier conducted in a fixed-fixed configuration can be used to define the global limit states for the bridge. As shown in Fig. 5.5, the displacements at first yielding (Δ_y), maximum load (Δ_m), 20% load reduction (Δ_r) and 80% load reduction (Δ_u) are defined as the

slight, moderate, extensive and complete damage limit states, respectively. The corresponding drift ratios are 1.45%, 2.6%, 4.3% and 6.9%. For the slight and moderate damage limit states, the coefficients of variation (COVs) are assumed to be 0.1 and 0.2, respectively. For the extensive and complete damage limit states, the COVs are assumed to be 0.3. The selection of these COVs incorporates engineering judgment, but also considers the fact that the behavior of the test specimen has higher uncertainty in the larger deformation range than in the lower deformation range (Kwon and Elnashai, 2007; Nielson and DesRoches, 2007).

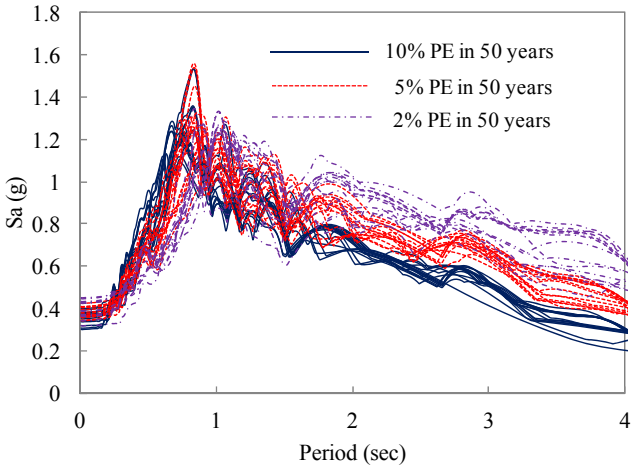

Figure 5.6 Response spectra of synthetic surface ground motions

5.6.2 Synthetic Ground Motions

To generate realistic ground motions for deriving analytical fragility functions for the MRO Bridge, bedrock motions are generated by firstly conducting seismic hazard deaggregation at the bridge site using the interactive deaggregation program of the U.S. Geological Survey (USGS). Three hazard levels are considered, including 10%, 5% and 2% probability of exceedance (PE) in 50 years. Seismic hazard deaggregation gives the magnitude, distance and standard deviation of the scenario earthquakes, which are then used in the Next Generation Attenuation (NGA) model (Campbell and Bozorgnia, 2008) to generate the corresponding response spectra. SIMQKE (Gasparini and Vanmarcke, 1976) is then applied to generate spectrum-compatible ground motion time histories for each hazard level. One input parameter required by SIMQKE is the significant duration of earthquake ground motion. Significant duration proposed by Kempton and Stewart (2006) is adopted, which provides the estimated mean duration ± standard deviation. Therefore three significant duration values including the mean ± standard deviation are obtained for each hazard level. In addition, to account for the uncertainty of duration, each estimated duration is expanded to five levels, including 95%, 100%. 105%, 110% and 120% of the original duration, leading to 45 ground motions in total with 15 ground motions from each hazard level.

To account for the local site effect, 1-D site response analysis is then carried out with the bedrock motions using DEEPSOIL (Hashash et al., 2009). The soil profile is adopted from the Resolution of Site Response Issues from the Northridge Earthquake (ROSRINE) test program (Anderson, 2003) which investigated the dynamic properties of the MRO Bridge site. The response spectra of the 45 surface ground motions are shown in Fig. 5.6.

5.6.3 Analytical Fragilities

Analytical fragility functions are derived using Monte Carlo simulation. To calculate seismic demand, the synthetic ground motions generated in previous section are scaled to have PGA from 0.1g to 1.0g with 0.1g increment based on the fact that higher hazard level tends to have larger PGA (Shah et al., 1975; Frankel and Leyendecker, 2001). More specifically, the ground motions from the first hazard level, i.e. 10% PE in 50 years, are scaled from 0.1 g to 0.3g. The second hazard level ground motions (5% PE in 50 years) are scaled from 0.4g to 0.6g. The third hazard level ground motions (2% PE in 50 years) are scaled from 0.6g to 1.0g. This scaling method can avoid the scaling factors being too large and hence keeps the realistic relationship between PGA and frequency content in the record. Therefore 150 ground motions in total are obtained and used in the nonlinear time history analyses for calculating the demand values (S_d). Meanwhile, 150 capacity values (S_c) are generated for each of the 4 damage limit states according to the mean capacity value and the associated COV. The median PGA and the dispersion of analytical fragility functions are then determined by using linear regression between $\ln(S_d/S_c)$ and $\ln(PGA)$. The mean value of $\ln(S_d/S_c)$, denoted by λ, is obtained as (Pan, 2007):

$$\lambda = a\ln(PGA) + b \tag{5.13}$$

in which a and b are regression parameters. The median PGA is then calculated by setting λ equal to 0. The dispersion is calculated as the standard deviation of $\ln(S_d/S_c)$ with respect to λ. The median PGAs and the dispersions of the two sets of analytical fragility functions, one with the initial FE model and the other with the calibrated FE model, are summarized in Table 5.4. The fragility functions are also depicted in Fig. 5.9 as the Case 1 and Case 2. Comparison shows that the fragility functions derived with the uncalibrated model are less vulnerable than these derived with the calibrated model, since the uncalibrated model tends to underestimate the bridge response as shown in Fig. 5.4(b) and Fig. 5.4(c).

5.7 Bayesian Updating of Fragilities Using Hybrid Simulation (Case 3 and Case 4)

5.7.1 Hybrid Simulation

The MRO Bridge is divided into three substructures, including the deck-abutment-embankment module, the pier module and the pile foundation module, in which the pier substructure is tested experimentally while the other two are simulated analytically in Zeus-NL, as illustrated in Fig. 5.7. The small scale pier specimens depicted in Fig. 5.2 are tested using the portable Load and Boundary Condition Box (pLBCB) at NEES@UIUC (Elnashai et al., 2004). The communication and interaction amongst the three substructure modules, as well as the numerical integration are handled in UI-SimCor (Kwon et al., 2005).

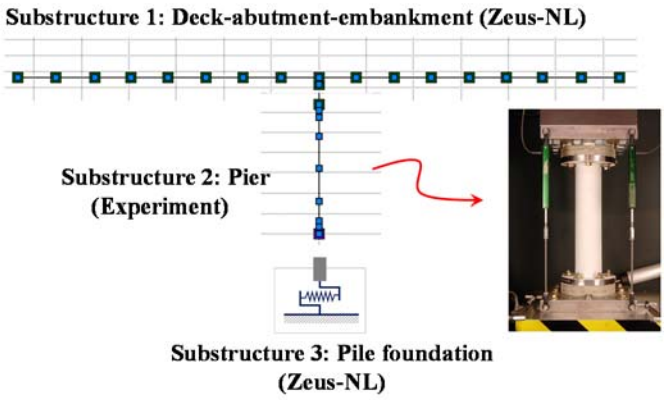

Figure 5.7 Substructuring of the MRO Bridge

Eight hybrid simulation experiments are conducted using seven pier specimens, with ground motion PGA ranging from 0.2g to 0.9g. One of the specimens is used in both the 0.2g and 0.3g tests due to the linear behavior of the specimen during the 0.2g test. Three synthetic ground motions, with each one of them corresponding to one hazard level, are selected from the 45 records described previously. Then, the record from the first hazard level is scaled from 0.2g to 0.3g. The record from the second hazard level is scaled from 0.4g to 0.6g and the record from the third hazard level is scaled from 0.8g to 0.9g. Three sample results from the 0.3g, 0.5g and 0.9g tests are shown in Fig. 5.8, which indicate that the model calibrated with cyclic test data predicts well the response in the cases with lower PGA, but overestimates the energy dissipation capability and underestimates the peak lateral drift response under large earthquake (0.9g). Therefore the calibrated model may yield lower failure probability in fragility functions in the range of high ground motion intensity. Table 5.3 summarizes the results of the eight tests, which are also expressed in binary numbers to form the likelihood function (Eq. (10)) for subsequent Bayesian updating.

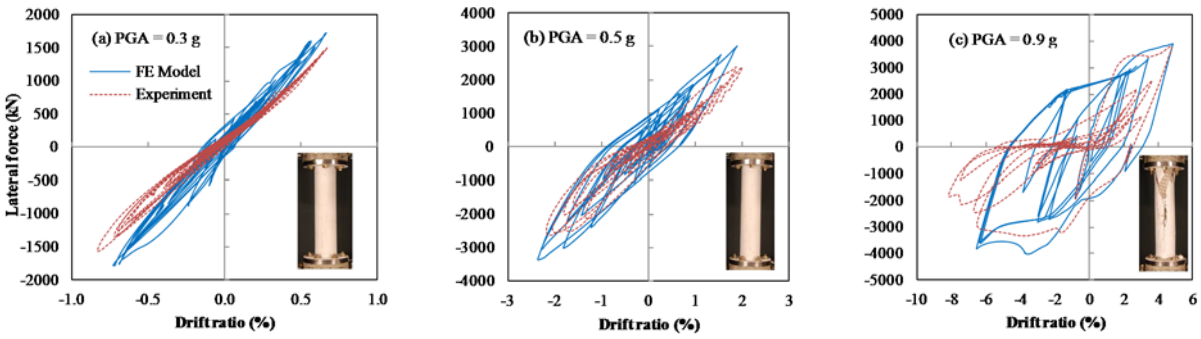

Figure 5.8 Sample results of Hybrid simulation experiments: (a) 0.3g; (b) 0.5g; (c) 0.9g

5.7.2 Bayesian Updating of Analytical Fragility Functions

Based on the Bayesian framework described in preceding section, the analytical fragility functions of Case 1 and Case 2 are updated using the hybrid simulation data. The joint prior distribution of the natural logarithm of the median PGA (μ) and the dispersion (σ) is formulated in Eq. (5.9). The likelihood function in Eq. (5.10) is formed using the hybrid simulation results expressed in binary number. The posterior distribution is thus proportional to the product of the prior distribution function and the likelihood function, as previously shown in Eq. (5.3).

Table 5.3 Hybrid simulation experimental results

Test number	PGA (g)	Tested Drift (mm)	Binary result ε (Limit state exceeded?)			
			Slight (93.44 mm)	Moderate (166.4 mm)	Extensive (275.2 mm)	Complete (441.6 mm)
1	0.2	17.38	0	0	0	0
2	0.3	55.07	0	0	0	0
3	0.4	116.5	1	0	0	0
4	0.5	141.53	1	0	0	0
5	0.6	195.11	1	1	0	0
6	0.7	304.6	1	1	1	0
7	0.8	384.77	1	1	1	0
8	0.9	523.37	1	1	1	1

To estimate the mode and mean of the posterior distribution, Markov Chain Monte Carlo (MCMC) with the Metropolis-Hastings scheme is utilized to draw samples from the posterior distribution. Reference is made to Koutsourelakis (2010) for the implementation detail of this sampling method. Essentially, a proposal density function $q(\boldsymbol{\theta}' \mid \boldsymbol{\theta}_0)$ is used to generate a new sample $\boldsymbol{\theta}'$ from the current sample $\boldsymbol{\theta}_0$. The probability of accepting the proposed sample is:

$$a = \min\left(1,\ \frac{f'(\boldsymbol{\theta}')\,q(\boldsymbol{\theta}_0 \mid \boldsymbol{\theta}')}{f'(\boldsymbol{\theta}_0)\,q(\boldsymbol{\theta}' \mid \boldsymbol{\theta}_0)}\right) \tag{5.14}$$

In this study, a random walk proposal density function is adopted for q. Totally 2×10^6 samples are drawn and the first 2000 samples are discarded to ensure convergence to the target distribution. The remained samples are further downsampled with a lag of 100 samples to reduce the interdependency between the samples. The posterior means are calculated directly using the samples. To estimate the posterior mode, kernel density estimation (Bowman and Azzalini, 1997) is applied to estimate the probability density function of the samples.

Table 5.4 Analytical and Bayesian updated fragility functions

Case*	Median PGA (g)				Dispersion			
	Slight	Moderate	Extensive	complete	Slight	Moderate	Extensive	complete
1	0.6306	0.8587	1.2092	1.5704	0.3324	0.3961	0.4338	0.4655
2	0.4075	0.5324	0.6768	0.866	0.2883	0.3876	0.4613	0.5106
3	0.3484	0.5587	0.6376	0.8709	0.2590	0.2770	0.3205	0.4936
4	0.3434	0.5301	0.6540	0.8613	0.2361	0.2742	0.3291	0.4852

*Case 1: analytical curves with uncalibrated bridge model; Case 2: analytical curves with calibrated model using cyclic test; Case 3: Bayesian updated curves of Case1 using hybrid simulation data; Case 4: Bayesian updated curves of Case 2 using hybrid simulation data.

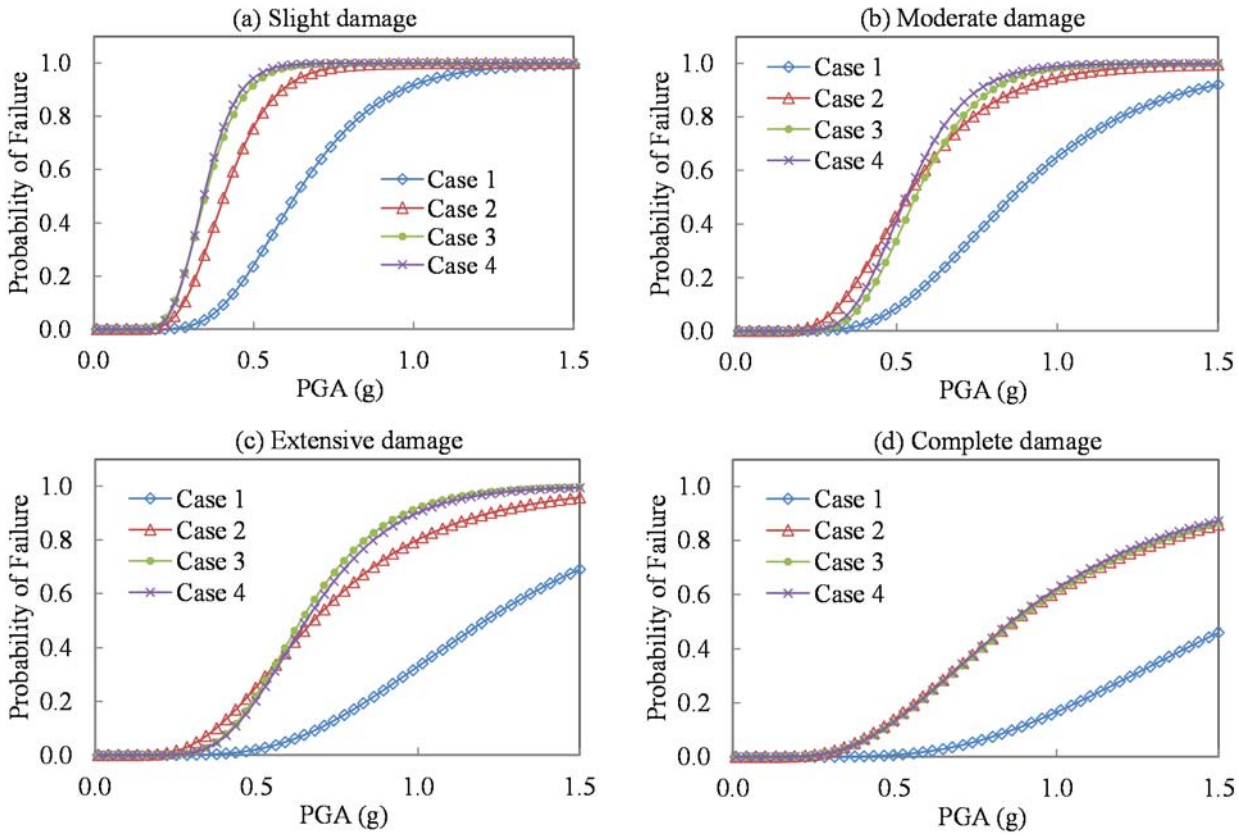

Figure 5.9 Comparison between the analytical and Bayesian updated fragility functions: (a) Slight damage; (b): Moderate damage; (c): Extensive damage; (d): Complete damage

The updated analytical fragility functions are summarized and depicted as Case 3 and Case 4 in Table 5.4 and Fig. 5.9, respectively. First of all, the fragility functions in Case 4 can be considered as the most reliable ones, in that they are derived in a way which incorporates the most experimental information, including the cyclic and the hybrid simulation tests, whereas other cases are based on either partial or no experimental data. Comparing Case 2 and Case 4, i.e. before and after Bayesian updating of the fragility functions for the calibrated model, both the median PGAs and the dispersions are decreased. The complete damage limit state has marginal change due to limited experimental information for this limit state, i.e. the hybrid simulation data shown in Table 5.3 has only one test that exceeds the complete damage limit state. In addition, the Bayesian updated fragility functions with the uncalibrated model shown in Case 3 achieve very close result to Case 4. In other words, through Bayesian updating, the information in the experimental data, which represents the real behavior of the bridge under earthquakes, is effectively conveyed to the updated fragility functions, even though the initial estimate has large deviation from the truth.

5.8 Risk Assessment

Earthquake risk assessment for bridges in the Imperial County, California, where the MRO Bridge is located, are conducted with the four sets of fragility functions using MAEviz, an open source platform for earthquake hazard risk management developed by the Mid-America

Earthquake (MAE) Center and the National Center for Supercomputing Applications (NCSA) at the University of Illinois at Urbana-Champaign (MAEviz, 2008). The inputs and procedure of seismic loss assessment in MAEviz are illustrated in Fig. 5.10 (Padgett et al., 2010). As shown in Fig. 5.10, the locations and characteristics from the bridge inventory, ground shaking at bridge locations and the fragility curves for the bridge classes are the key components involved in the earthquake risk assessment. In the analysis, the bridge damage states are evaluated based on the fragility functions and the ground motion intensities at the bridge locations, then the direct losses due to repair and replacement of the damage bridges are estimated using the replacement cost data and the bridge repair cost ratios. More details about the loss assessment analysis can be found in Padgett et al. (2010).

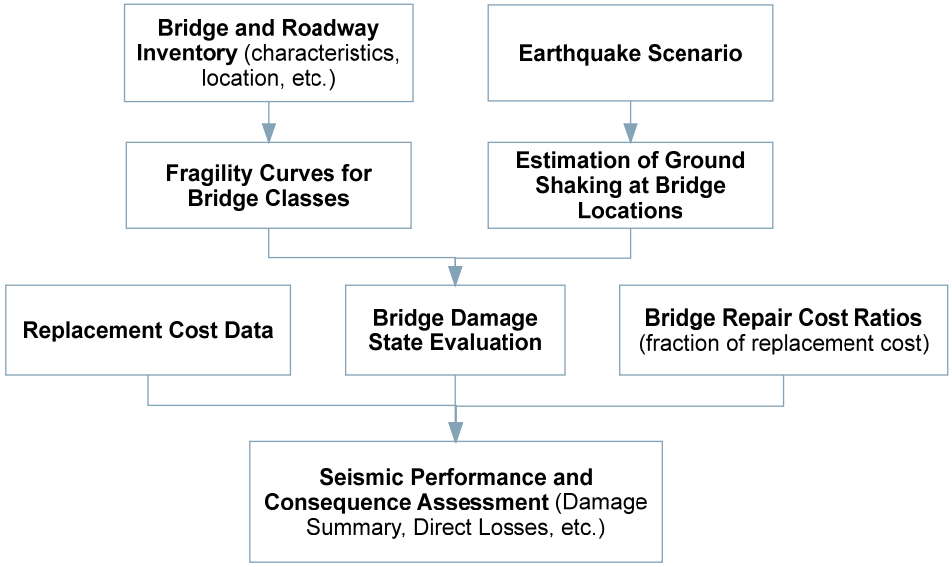

Figure 5.10 General flow chart for seismic loss assessment of bridge network (after Padgett et al. 2010)

From the National Bridge Inventory, 122 bridges in total are found to belong to the same category as the MRO Bridge. To examine the effect of the difference in fragility functions on the risk assessment result, assumption is made herein that all of these 122 bridges share the same fragility functions. The risk assessment analysis is therefore for illustrative purposes only due to this assumption. Hazard map is generated using the 1940 El Centro earthquake as the scenario earthquake in MAEviz. Fig. 5.11 depicts the bridge inventory and the generated hazard map. In the analysis, the fragility functions and the PGA values at bridge locations are used to determine the damage states of the bridges. Table 5.5 summarizes the number of bridges that fall into each damage states for the four cases. To estimate the repair cost, the bridge replacement cost data and the damage ratios used in Padgett et al. (2010) are adopted herein for illustration purpose. Repair cost of each bridge is then estimated and the total repair costs are summarized and listed in Table 5.5.

The risk assessment result is consistent with the fragility functions. First of all, the repair cost estimated by the fragility functions from the uncalibrated model (Case 1) is significantly underestimated and has a much higher uncertainty compared with Case 2. By applying Bayesian updating to both Case 1 and Case 2, as is the case in the fragility functions, the updated estimations of repair cost are very close (Case 3 and Case 4), showing once again the

effectiveness of Bayesian updating for the case when the prior information is inaccurate. When the fragility functions are derived with the calibrated model, the additional hybrid simulation tests serves as a validation of the analytical fragility functions, which are also slightly improved through Bayesian updating.

Table 5.5 Risk assessment results

Case	Number of Bridges in each limit state					Repair cost (unit: USD)	
	None	Slight	Moderate	Extensive	Complete	Mean	COV
1	95	17	10	0	0	340,833	0.651
2	64	6	38	12	2	2,400,717	0.265
3	66	5	37	12	2	2,268,015	0.273
4	66	5	37	12	2	2,293,434	0.270

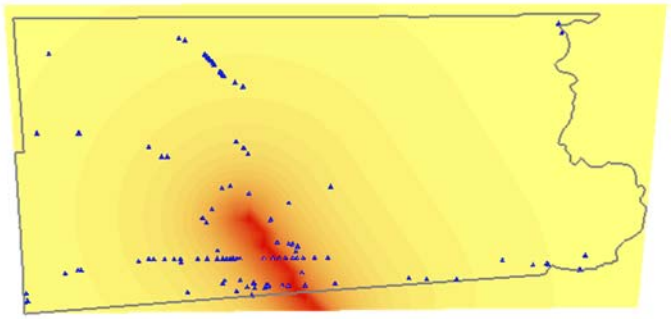

Figure 5.11 Bridge inventory and hazard map of Imperial County, CA (generated by MAEviz)

5.9 Summary

In this chapter, a two-stage approach for generating improved fragility functions for engineering structures was proposed. First, a finite element model, including the linear and nonlinear parameters, was calibrated using a cyclic test and seismic measurements. The generated analytical fragility functions were then updated using a few hybrid simulation tests through Bayesian updating. To illustrate the effectiveness of the proposed approach, four sets of fragility functions were derived for the Meloland Road Overcrossing Bridge, corresponding to four cases which represent an increasing level of data availability. Finally, risk assessment was conducted for Imperial County, California to illustrate the importance of fragility function accuracy. The fragility functions derived with the uncalibrated model were found to significantly underestimate the failure probability, as the bridge response is underestimated by the model, and are associated with larger uncertainty. A three-step model calibration method was proposed and applied to calibrate the nonlinear pier model, the linear deck model, and the nonlinear abutment model in a sequential manner. The effectiveness of the model calibration method is validated by comparison between the model prediction and the experimental results and seismic measurements.

The proposed Bayesian updating strategy based on a few hybrid simulation experiments is shown to be effective. When the initial analytical fragility functions are accurate, such as Case 2 when the fragilities are derived with the calibrated model, hybrid simulation tests serve as a

validation of the analytical fragility functions while slightly improving the curves through Bayesian updating. The strategy is attractive from the perspective of database maintenance for loss assessment systems; in that the fragility database can be updated in a continuous manner as more data becomes available. When the initial analytical fragility functions have significant inaccuracies, such as Case 1, hybrid simulation tests can effectively improve the fragility functions through Bayesian updating. This Bayesian updating strategy provides a systematic and effective way of improving fragility estimation to support reliable seismic risk assessment.

SUBSTRUCTURE HYBRID SIMULATION WITH MSE

Substructure hybrid simulation of engineering structures subjected to multiple-support excitation (MSE) is investigated in this chapter. The equations of motion formulated in relative coordinates (EOM-rel) has been widely used in conventional time-history analysis of MSE problems but has not been attempted to hybrid simulation. Only the formulation in absolute coordinates (EOM-abs) has been considered in previously study. The hybrid simulation problem for structure subjected to MSE is carefully formulated and the tradeoffs in the two approaches are examined. In addition, UI-SimCor, the hybrid simulation framework developed at the University of Illinois is extended to include the MSE capability. This chapter provides essential theoretical basis and practical tool for conducing hybrid simulation under MSE, which is important when high-fidelity fragility function estimation and seismic risk assessment are to be performed for structures subjected to MSE.

6.1 Formulations of Equations of Motion for MSE Problems

For the general case of earthquake excitation, the support degrees of freedom (DOFs) should be included in the equation of motion, which can be written in partitioned form as follows (Chopra, 2001):

$$\begin{bmatrix} \mathbf{M}_{ss} & \mathbf{M}_{sg} \\ \mathbf{M}_{gs} & \mathbf{M}_{gg} \end{bmatrix} \begin{Bmatrix} \ddot{\mathbf{x}}_s^a \\ \ddot{\mathbf{x}}_g \end{Bmatrix} + \begin{bmatrix} \mathbf{C}_{ss} & \mathbf{C}_{sg} \\ \mathbf{C}_{gs} & \mathbf{C}_{gg} \end{bmatrix} \begin{Bmatrix} \dot{\mathbf{x}}_s^a \\ \dot{\mathbf{x}}_g \end{Bmatrix} + \begin{bmatrix} \mathbf{K}_{ss} & \mathbf{K}_{sg} \\ \mathbf{K}_{gs} & \mathbf{K}_{gg} \end{bmatrix} \begin{Bmatrix} \mathbf{x}_s^a \\ \mathbf{x}_g \end{Bmatrix} = \begin{Bmatrix} \mathbf{0} \\ \mathbf{f}_g \end{Bmatrix} \tag{6.1}$$

in which subscript s denotes superstructure DOFs and subscript g denotes support/ground DOFs. The superscript a indicates absolute coordinate. The support force vector is represented by $\mathbf{f}_g$. For the sake of simplicity, Eq. (6.1) is formulated in terms of linear structures in which the stiffness matrix is constant. However, for nonlinear structures, the stiffness matrix can be state dependent.

Expanding the first block row of Eq. (6.1), the equations of motion can be rewritten as follows:

$$\mathbf{M}_{ss}\ddot{\mathbf{x}}_s^a + \mathbf{C}_{ss}\dot{\mathbf{x}}_s^a + \mathbf{K}_{ss}\mathbf{x}_s^a = -\mathbf{M}_{sg}\ddot{\mathbf{x}}_g - \mathbf{C}_{sg}\dot{\mathbf{x}}_g - \mathbf{K}_{sg}\mathbf{x}_g \tag{6.2}$$

For the lumped mass case, the coupling terms in the mass matrix are zero, and thus the equation of motion in absolute coordinates (designated EOM-abs) is

$$\mathbf{M}_{ss}\ddot{\mathbf{x}}_s^a + \mathbf{C}_{ss}\dot{\mathbf{x}}_s^a + \mathbf{K}_{ss}\mathbf{x}_s^a = -\mathbf{C}_{sg}\dot{\mathbf{x}}_g - \mathbf{K}_{sg}\mathbf{x}_g \tag{6.3a}$$

or

$$\mathbf{M}_{ss}\ddot{\mathbf{x}}_s^a + \mathbf{C}_{ss}\dot{\mathbf{x}}_s^a + \mathbf{F}_r = -\mathbf{C}_{sg}\dot{\mathbf{x}}_g \tag{6.3b}$$

in which $\mathbf{F}_r = \mathbf{K}_{ss}\mathbf{x}_s^a + \mathbf{K}_{sg}\mathbf{x}_g$ is the restoring force.

Based on the above formulation, the absolute displacement can be further decomposed into two parts, namely, a pseudo-static part and a dynamic part. The first part is caused by differential support movements, while the second part is due to inertial forces with respect to pseudo-static displacements, i.e. (Chopra, 2001)

$$\mathbf{x}_s^a = \mathbf{x}_d + \mathbf{x}_{ps} \tag{6.4}$$

where d denotes dynamic coordinates and ps denotes pseudo-static coordinates. The term $\mathbf{x}_{ps}$ can be obtained by solving the following static equation of motion,

$$\begin{bmatrix} \mathbf{K}_{ss} & \mathbf{K}_{sg} \\ \mathbf{K}_{gs} & \mathbf{K}_{gg} \end{bmatrix} \begin{Bmatrix} \mathbf{x}_{ps} \\ \mathbf{x}_{g} \end{Bmatrix} = \begin{Bmatrix} \mathbf{0} \\ \mathbf{f}_{g} \end{Bmatrix} \tag{6.5}$$

hence

$$\mathbf{x}_{ps} = -\mathbf{K}_{ss}^{-1}\mathbf{K}_{sg}\mathbf{x}_{g} = \mathbf{R}_{v}\mathbf{x}_{g} \tag{6.6}$$

where $\mathbf{R}_{v} = -\mathbf{K}_{ss}^{-1}\mathbf{K}_{sg}$ is called the influence factor matrix. Substituting Eqs. (6.4) and (6.6) into Eq. (6.3a), the equation of motion in dynamic coordinates (designated EOM-rel) can be obtained as follows

$$\mathbf{M}_{ss}\ddot{\mathbf{x}}_{d} + \mathbf{C}_{ss}\dot{\mathbf{x}}_{d} + \mathbf{K}_{ss}\mathbf{x}_{d} = -\mathbf{M}_{ss}\mathbf{R}_{v}\ddot{\mathbf{x}}_{g} - (\mathbf{C}_{ss}\mathbf{R}_{v} + \mathbf{C}_{sg})\dot{\mathbf{x}}_{g} \tag{6.7}$$

To have a damping force proportional to the relative velocity $\dot{\mathbf{x}}_{d}$, the coupling damping matrix $\mathbf{C}_{sg}$ can be set equal to $-\mathbf{C}_{ss}\mathbf{R}_{v}$ such that the second term in the RHS of Eq. (6.7) equals to zero. Then, Eq. (6.7) becomes

$$\mathbf{M}_{ss}\ddot{\mathbf{x}}_{d} + \mathbf{C}_{ss}\dot{\mathbf{x}}_{d} + \mathbf{K}_{ss}\mathbf{x}_{d} = -\mathbf{M}_{ss}\mathbf{R}_{v}\ddot{\mathbf{x}}_{g} \tag{6.8}$$

6.2 Comparison Between EOM-abs and EOM-rel

Generally, the EOM-rel approach is more widely used in the literature for conventional time history analyses involving MSE, because it retains a form similar to the conventional equations of motion for uniform base excitation. The ground acceleration is the only explicit input information required in the equation of motion, whereas EOM-abs requires both ground displacement and velocity, which cannot be obtained directly from typical seismic instrumentation. In addition, in the EOM-rel formulation, the decomposition of the total displacement into pseudo-static and dynamic components enables a physical interpretation of the coordinates for the structural response under MSE, i.e., the inertia forces and the differential movement of the supports.

In contrast to the situation for conventional time history analysis, if the EOM-rel is used in a hybrid simulation, the stiffness matrices $\mathbf{K}_{ss}$ and $\mathbf{K}_{sg}$ cannot be updated easily during the experiment, which may introduce error. Because the right hand side of Eq. (6.6) includes an influence matrix which depends on these stiffness matrices, the EOM-rel is not employed readily for hybrid simulation with changing stiffness. Namzy and Abdel-Ghaffar (1990) made an assumption that the changes in $\mathbf{K}_{ss}^{-1}$ and $\mathbf{K}_{sg}$ can cancel each other when they are multiplied together in Eq. (6.6); therefore, the influence matrix can be assumed constant and not affected by a change in the stiffness of the structure. The purpose for this assumption was to avoid inverting $\mathbf{K}_{ss}$ at the beginning of each iteration in the nonlinear time-stepping integration. However, further studies are needed to assess the error introduced by ignoring the change of stiffness in hybrid simulation using EOM-rel. The EOM-rel without updating the stiffness is therefore referred to as the EOM-rel approximation in subsequent discussion.

Note that the EOMs described in Eq (6.3a) and (6.8) are solved in a total manner, i.e., all the DOFs, belonging to both experimental and numerical substructures, are formulated in the

equations of motion; hence time stepping integration is applied to all the DOFs. A different approach, called the dynamic substructuring approach (Wagg et al., 2008 and Shing, 2008) is applicable when the dynamic response of the experimental substructure can be completely captured by experimental testing. In such a case, the need to create or update the stiffness matrix of the experimental substructure is obviated because numerical integration is not used at the experimental DOF. In the hybrid simulation conducted in this paper, the damping and inertial forces of the experimental substructure are added numerically, and thus the dynamic substructuring approach cannot be employed.

6.3 Effect of Ignoring Stiffness Change in EOM-rel

The effect of ignoring the stiffness change in experimental substructure for the EOM-rel can be qualitatively evaluated by understanding the influence matrix $\mathbf{R}_v = -\mathbf{K}_{ss}^{-1}\mathbf{K}_{sg}$ in Eq. (6.6). The summation of each row of $\mathbf{R}_v$ equals to one (or zero for the DOF's without associated ground motion input), $\mathbf{R}_v$ is therefore a weighting matrix for the multiple ground motion inputs. If the ground motion inputs are identical, as in the case of uniform ground motion excitation, a change in stiffness will have no influence on the input. However, if the ground motion inputs are different from each other, then a change in the weighting matrix (i.e., the influence matrix) will lead to different inputs to the structure, and thus to errors in the structural response if the change is not captured.

To quantitatively evaluate the effect of ignoring stiffness change, a numerical study is carried out. In the remainder of this section, numerical integration is employed to solve the EOM-rel approximation and EOM-abs to facilitate the direct comparison between the case when the nonlinear portion of stiffness matrices is neglected and the case when it is considered, respectively.

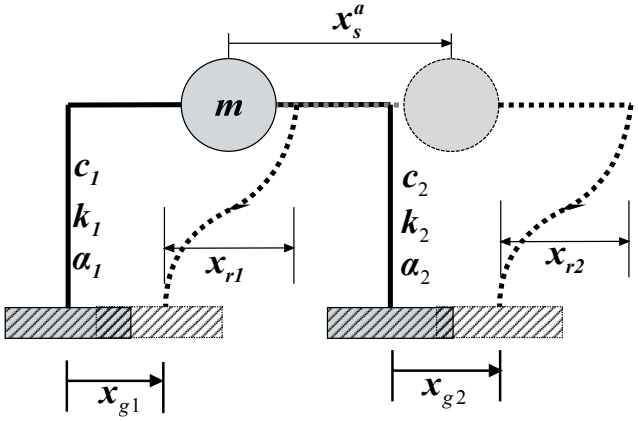

Figure 6.1 SDOF oscillators subjected to two ground excitations.

6.3.1 Nonlinear SDOF oscillator with two ground excitations

To highlight the effect of ignoring stiffness change, a single-degree-of-freedom (SDOF) oscillator excited by two ground motions is investigated, as shown in Fig. 6.1. The restoring force of each column is modeled using the Bouc-Wen hysteretic model (Wen, 1976; Barber and Wen, 1981) given by

$$f_{ri}(t) = \alpha_i k_i x_{ri}(t) + (1-\alpha_i) k_i x_y z_i(t), \quad i = 1, 2 \tag{6.9}$$

where $x_{ri} = x_d + x_{ps} - x_{gi}$ is the shear deformation of each column. The term k_i is the linear stiffness, x_y is the yield deformation, and α is the ratio of the post- to pre-yield stiffness. The evolutionary variable z_i models the smooth hysteretic behavior and is governed by the following differential equation

$$\dot{z}_i(t) = \frac{1}{x_y}\left(-\gamma_i \left|\dot{x}_{ri}(t)\right| \left|z_i(t)\right|^{n_i - 1} z_i(t) - \beta_i \dot{x}_{ri}(t) \left|z_i(t)\right|^{n_i} + A_i \dot{x}_{ri}(t)\right) \tag{6.10}$$

In the equation, the parameters γ_i, β_i, n_i, and A_i control the shape of the hysteretic loop. When $\gamma + \beta > 0$ and $\gamma - \beta = 0$, the model has several desirable attributes which exist in engineering materials such as steel, including linear unloading; reloading very closely along the previous unloading path; and a smooth transition between the pre- and post-yield region of response (Wen, 1976; Baber and Wen, 1981; Spencer, 1986), as shown in Fig. 6.2. The parameters of the SDOF oscillator are designated as listed in Table 6.1.

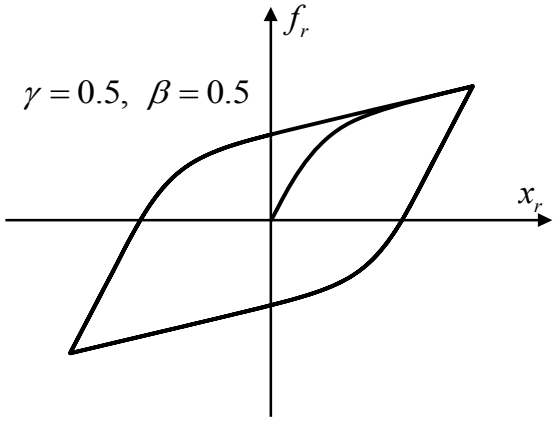

Figure 6.2 Bouc-Wen hysteretic model.

Table 6.1 Parameters of the SDOF oscillator

$m(kg)$	$x_y(m)$	$k_1(N/m)$	$k_2(N/m)$	$c_1(N \cdot s/m)$	c_2	α_1	α_2
2.07	0.01	100	500	50	50	0.3	0.01
γ_1	γ_2	n_1	n_2	β_1	β_2	A_1	A_2
0.5	0.5	2	2	0.5	0.5	1	1

In Table 6.1, m is the mass of the oscillator, k_1 and k_2, and c_1 and c_2 are the linear stiffness and damping factors of the two columns, respectively. With these defined parameters, the EOM-rel and EOM-abs can be expressed as

$$\text{EOM-rel: } \mathbf{M}_{ss}\ddot{\mathbf{x}}_d + \mathbf{C}_{ss}\dot{\mathbf{x}}_d + \mathbf{F}_{rd} = -\mathbf{M}_{ss}\mathbf{R}_v\ddot{\mathbf{x}}_g \tag{6.11}$$

$$\text{EOM-abs: } \mathbf{M}_{ss}\ddot{\mathbf{x}}_s^a + \mathbf{C}_{ss}\dot{\mathbf{x}}_s^a + \mathbf{F}_{ra} = -\mathbf{C}_{sg}\dot{\mathbf{x}}_g \tag{6.12}$$

where $\mathbf{F}_{rd}$ and $\mathbf{F}_{ra}$ are the restoring forces, and $\ddot{\mathbf{x}}_g$ is the ground acceleration vector. Each variable is derived as follows

$$\begin{aligned}
&\mathbf{M}_{ss} = m \\
&\mathbf{C}_{ss} = c_1 + c_2 \\
&\mathbf{C}_{sg} = \begin{bmatrix} -c_1 & -c_2 \end{bmatrix} \\
&\mathbf{F}_{rd} = \mathbf{K}_{ss}\mathbf{x}_d + \mathbf{K}_{BW}\mathbf{Z} \\
&\mathbf{F}_{ra} = \mathbf{K}_{ss}\mathbf{x}_s^a + \mathbf{K}_{BW}\mathbf{Z} + \mathbf{K}_{sg}\mathbf{x}_g \\
&\mathbf{R}_v = -\mathbf{K}_{ss}^{-1}\mathbf{K}_{sg}
\end{aligned} \tag{6.13}$$

in which

$$\begin{aligned}
&\mathbf{K}_{ss} = \alpha_1 k_1 + \alpha_2 k_2 \\
&\mathbf{K}_{BW} = \begin{bmatrix} (1-\alpha_1)k_1 & (1-\alpha_2)k_2 \end{bmatrix} \\
&\mathbf{K}_{sg} = \begin{bmatrix} -\alpha_1 k_1 & -\alpha_2 k_2 \end{bmatrix}, \\
&\mathbf{Z} = \begin{bmatrix} z_1 & z_2 \end{bmatrix}^{\mathrm{T}},\ \mathbf{x}_g = \begin{bmatrix} \ddot{x}_{g1} & \ddot{x}_{g2} \end{bmatrix}^{\mathrm{T}}
\end{aligned} \tag{6.14}$$

6.3.2 Time-step integration strategy

In the formulation of EOM-rel, the total displacement is decomposed into pseudo-static and dynamic components in a step-by-step manner; therefore, time-stepping integration is required to extract both components throughout the analysis. The EOM-rel and EOM-abs are thus transformed into the following incremental equations of motion

$$\text{EOM-rel: } \mathbf{M}_{ss}\Delta\ddot{\mathbf{x}}_d + \mathbf{C}_{ss}\Delta\dot{\mathbf{x}}_d + \Delta\mathbf{F}_{rd} = \Delta\mathbf{P}_d^{ext} \tag{6.15a}$$

$$\Delta\mathbf{P}_d^{ext} = -\mathbf{M}_{ss}\Delta\ddot{\mathbf{x}}_{ps} = \mathbf{M}_{ss}\left(\left[\mathbf{K}_{ss}^{\mathrm{T}}\right]^{-1}\mathbf{K}_{sg}^{\mathrm{T}}\right)\Delta\ddot{\mathbf{x}}_g \tag{6.15b}$$

$$\text{EOM-abs: } \mathbf{M}_{ss}\Delta\ddot{\mathbf{x}}_a^s + \mathbf{C}_{ss}\Delta\dot{\mathbf{x}}_a^s + \Delta\mathbf{F}_{ra} = \Delta\mathbf{P}_a^{ext} \tag{6.16a}$$

$$\Delta\mathbf{P}_a^{ext} = -\mathbf{C}_{sg}\Delta\dot{\mathbf{x}}_g \tag{6.16b}$$

In these equations, Δ indicates the increment in the responses for one integration step. Many procedures are available to solve these incremental equations of motion (Bathe and Wilson, 1973). In this study, the linear acceleration formulation ($\gamma = 1/2, \beta = 1/6$) of the Newmark-β method is selected (Newmark, 1959). It should be noted that $\mathbf{K}_{ss}^{\mathrm{T}}$ and $\mathbf{K}_{sg}^{\mathrm{T}}$ are the tangent stiffness matrices at the beginning of each time step when the secant stiffness is unknown. For the Bouc-Wen model, the tangent stiffness can be obtained from Eq. (6.17) and is expressed as

$$k_i^T = \frac{df_{ri}}{dx_{ri}} = \alpha_i k_i + (1-\alpha_i)k_i x_y \frac{dz_i(t)}{dx_{ri}},\quad i = 1, 2 \tag{6.17}$$

in which the first order derivative of the evolutionary parameter z_i can be derived from the differential equation shown in Eq. (6.18) (Spencer, 1986).

$$
\begin{aligned}
dz/dx_r &= A-(\gamma+\beta)z^n, && z\geq 0, \dot{x}_r \geq 0\\
dz/dx_r &= A-(\beta-\gamma)z^n, && z\geq 0, \dot{x}_r < 0\\
dz/dx_r &= A-(-1)^{n+1}(\gamma+\beta)z^n, && z<0, \dot{x}_r < 0\\
dz/dx_r &= A-(-1)^{n+1}(\beta-\gamma)z^n, && z<0, \dot{x}_r \geq 0
\end{aligned}
\tag{6.18}
$$

Replacing the secant stiffness with the tangent stiffness in the incremental equation of motion will cause a residual force at the end of each time increment, depending on the size of the time step. Therefore, the modified Newton-Raphson iteration scheme is applied at the end of each time step to achieve dynamic equilibrium (Chopra, 2001). During the iteration, to track the actual restoring forces of the columns in Eq. (6.9), the differential equation, Eq. (6.10), needs to be solved for the evolutionary parameter z. This solution is achieved using the ordinary differential equation solver, ode45 in MATLAB (Mathworks, 2009). The residual force, which is the difference between the external load and the restoring force from ode45, is then calculated. The additional displacement caused by the residual force is then computed and added to the response. This procedure is repeated until the percentage difference between two consecutive residual forces is less than a given tolerance (10^{-6} is used in this study).

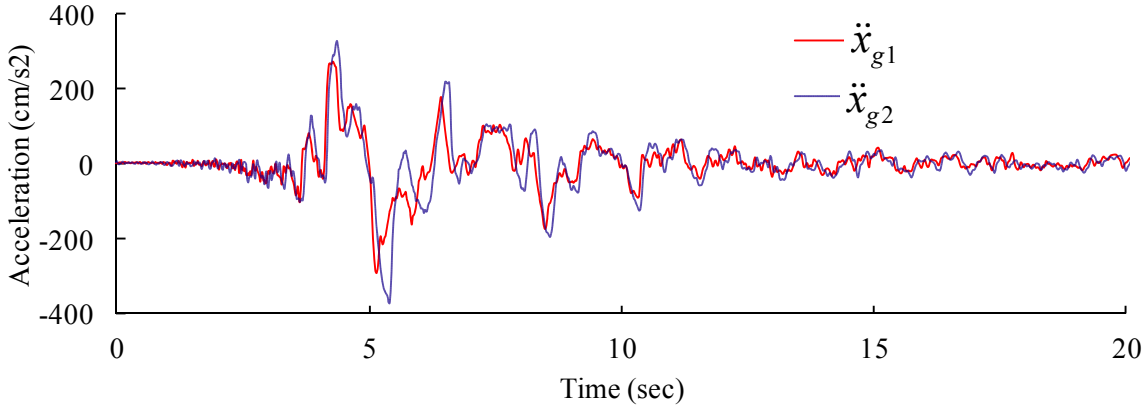

Figure 6.3 Input ground accelerations.

For the EOM-rel approximation, initial stiffness values are used for $\mathbf{K}_{ss}^{T}$ and $\mathbf{K}_{sg}^{T}$ in Eq. (6.15b) to simulate the case of ignoring nonlinear portion of stiffness in hybrid simulation, which also simplifies the Newton-Raphson iteration procedure by having known equivalent force before the iteration, as oppose to unknown force which may result in more complicated iteration. The result is then compared with EOM-abs.

6.3.3 Input ground motions and comparison of results

Two records from the 1979 Imperial Valley earthquake measured from the Meloland Road Overcrossing (MRO, CSMIP station NO. 1336) are used; $\ddot{x}_{g1}$ is the free-field response, and $\ddot{x}_{g2}$ is the embankment response, as shown in Fig. 6.3. Baseline correction was conducted for both acceleration records before they were integrated twice to get displacement time histories for restoring force calculations (Yang et al., 2006).

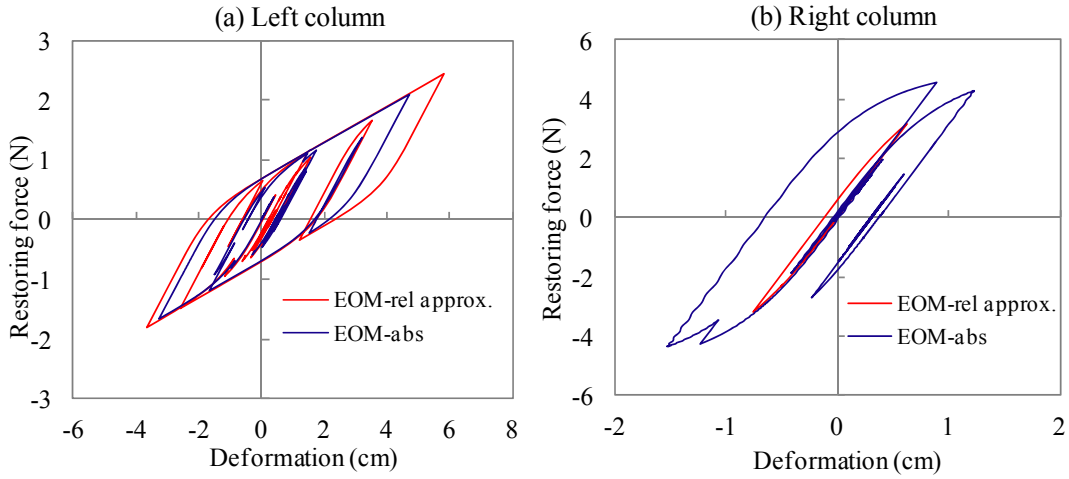

Figure 6.4 Hysteretic curves of the two columns in the EOM-rel approximation and EOM-abs formulation.

The shear deformation histories of the two columns are then calculated using the time-stepping integration method described in the preceding section. Comparisons between the EOM-rel approximation and the EOM-abs formulation are shown in Fig. 6.4. In EOM-rel approximation (i.e., where the stiffness change is neglected), the maximum shear deformation in left column is overestimated by 24.06% and the right column is underestimated by 50.96%. Therefore, for the EOM-rel approximation, neglecting the change of stiffness in nonlinear hybrid simulation may introduce significant error in the structural response. To further compare the two approaches for hybrid simulation, a comparison based on a highway bridge will be conducted using hybrid simulation in subsequent sections.

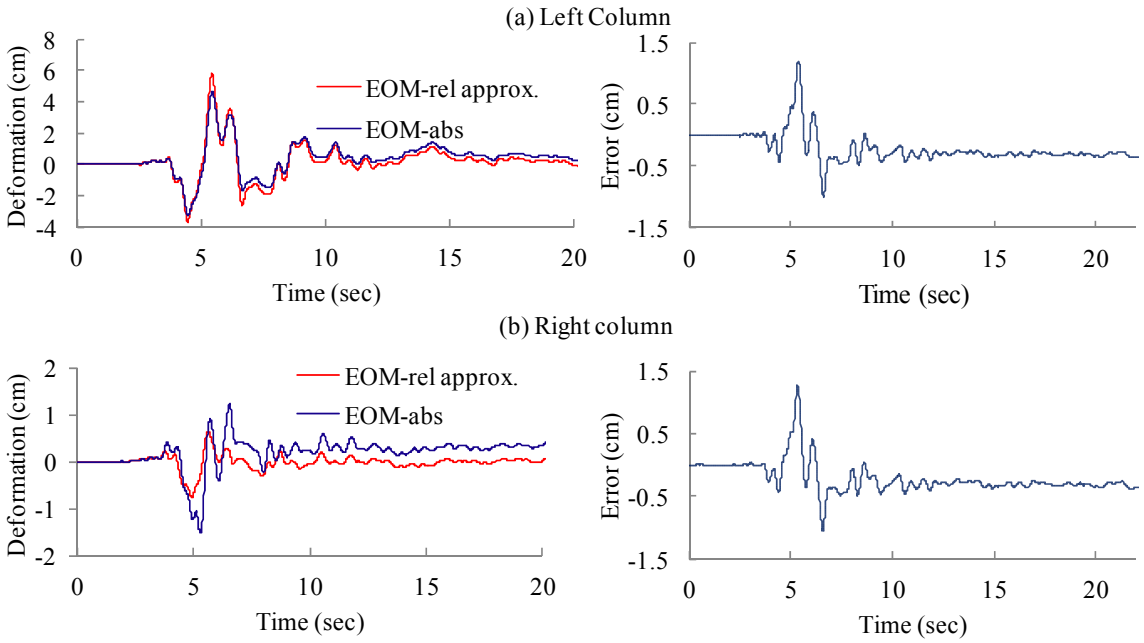

Figure 6.5 Deformation of the two columns in EOM-rel approximation and EOM-abs.

When calculating the difference between the exact and approximate deformation (i.e., the error) of the two columns relative to the ground, the ground motions x_{g1} and x_{g2} drop out of the expression. Moreover, because the displacements at the top of the columns for this SDOF system are identical, the error in the deformation for the two columns will be identical, as shown in Figure 6.5.

6.4 Implementation of Hybrid Simulation with MSE

The implementation of hybrid simulation in this section is completed by extending UI-SimCor (Kwon, 2008) to accommodate multiple ground motion inputs. UI-SimCor, the Multi-Site Substructure Pseudo-Dynamic Simulation Coordinator developed at the NEES site at the University of Illinois, is an object-oriented framework which allows for the combination of various analytical platforms and geographically distributed experimental models into pseudo-dynamic simulation (Kwon, 2008). A distinct feature of UI-SimCor is that all substructures, whether they are modeled numerically or experimentally, are treated equally as restoring force modules. A framework is provided for coordination of these substructures, which enables great flexibility to accommodate new simulation tools and integration schemes.

6.4.1 Static condensation for Hybrid Simulation with MSE

Static condensation temporarily eliminates the unimportant DOFs from the structure, and hence allows complex structures with many DOFs to be tested with pseudo-dynamic hybrid simulation. In hybrid simulation with MSE, the equation of motion, Eq. (6.1), can be rewritten as:

$$\begin{bmatrix} \mathbf{M}_i & \mathbf{0} & \mathbf{0} & \mathbf{0} \\ \mathbf{0} & \mathbf{0} & \mathbf{0} & \mathbf{0} \\ \mathbf{0} & \mathbf{0} & \mathbf{0} & \mathbf{0} \\ \mathbf{0} & \mathbf{0} & \mathbf{0} & \mathbf{0} \end{bmatrix} \begin{Bmatrix} \ddot{\mathbf{X}}_i^a \\ \ddot{\mathbf{X}}_j^a \\ \ddot{\mathbf{X}}_k^a \\ \ddot{\mathbf{X}}_g^a \end{Bmatrix} + \begin{bmatrix} \mathbf{K}_{ii} & \mathbf{K}_{ij} & \mathbf{K}_{ik} & \mathbf{K}_{ig} \\ \mathbf{K}_{ji} & \mathbf{K}_{jj} & \mathbf{K}_{jk} & \mathbf{K}_{jg} \\ \mathbf{K}_{ki} & \mathbf{K}_{kj} & \mathbf{K}_{kk} & \mathbf{K}_{kg} \\ \mathbf{K}_{gi} & \mathbf{K}_{gj} & \mathbf{K}_{gk} & \mathbf{K}_{gg} \end{bmatrix} \begin{Bmatrix} \mathbf{X}_i^a \\ \mathbf{X}_j^a \\ \mathbf{X}_k^a \\ \mathbf{X}_g \end{Bmatrix} = \begin{Bmatrix} \mathbf{0} \\ \mathbf{0} \\ \mathbf{0} \\ \mathbf{f}_g \end{Bmatrix} \tag{6.19}$$

where indices *i*, *j*, *k* and *g* denote the DOFs where masses are defined, DOFs that are of interest, DOFs that are not of interest, and DOFs attached to the ground which are also not of interest, respectively. Therefore, DOFs, *k* and *g* will be condensed out. The damping matrix is omitted here for simplicity.

By transforming Eq. (6.19) into the EOM-abs, we have the following equation:

$$\begin{bmatrix} \mathbf{M}_i & \mathbf{0} & \mathbf{0} \\ \mathbf{0} & \mathbf{0} & \mathbf{0} \\ \mathbf{0} & \mathbf{0} & \mathbf{0} \end{bmatrix} \begin{Bmatrix} \ddot{\mathbf{X}}_i^a \\ \ddot{\mathbf{X}}_j^a \\ \ddot{\mathbf{X}}_k^a \end{Bmatrix} + \begin{bmatrix} \mathbf{K}_{ii} & \mathbf{K}_{ij} & \mathbf{K}_{ik} \\ \mathbf{K}_{ji} & \mathbf{K}_{jj} & \mathbf{K}_{jk} \\ \mathbf{K}_{ki} & \mathbf{K}_{kj} & \mathbf{K}_{kk} \end{bmatrix} \begin{Bmatrix} \mathbf{X}_i^a \\ \mathbf{X}_j^a \\ \mathbf{X}_k^a \end{Bmatrix} + \begin{bmatrix} \mathbf{K}_{ig} \\ \mathbf{K}_{jg} \\ \mathbf{K}_{kg} \end{bmatrix} \mathbf{X}_g = \begin{Bmatrix} \mathbf{0} \\ \mathbf{0} \\ \mathbf{0} \end{Bmatrix} \tag{6.20}$$

where $\mathbf{f}_g$ is removed from equation by keeping the DOFs of the structure which are of interest. DOF *k* can be condensed through static condensation as below.

$$\begin{bmatrix} \mathbf{M}_i & \mathbf{0} \\ \mathbf{0} & \mathbf{0} \end{bmatrix} \begin{Bmatrix} \ddot{\mathbf{X}}_i^a \\ \ddot{\mathbf{X}}_j^a \end{Bmatrix} + \begin{bmatrix} \mathbf{K}_{ii}^* & \mathbf{K}_{ij}^* \\ \mathbf{K}_{ji}^* & \mathbf{K}_{jj}^* \end{bmatrix} \begin{Bmatrix} \mathbf{X}_i^a \\ \mathbf{X}_j^a \end{Bmatrix} + \begin{bmatrix} \mathbf{K}_{ig}^* \\ \mathbf{K}_{jg}^* \end{bmatrix} \mathbf{X}_g = \begin{Bmatrix} \mathbf{0} \\ \mathbf{0} \end{Bmatrix} \tag{6.21}$$

The condensed EOM-abs is obtained as follows:

$$\begin{bmatrix} \mathbf{M}_i & \mathbf{0} \\ \mathbf{0} & \mathbf{0} \end{bmatrix} \begin{Bmatrix} \ddot{\mathbf{X}}_i^a \\ \ddot{\mathbf{X}}_j^a \end{Bmatrix} + \begin{bmatrix} \mathbf{K}_{ii}^* & \mathbf{K}_{ij}^* \\ \mathbf{K}_{ji}^* & \mathbf{K}_{jj}^* \end{bmatrix} \begin{Bmatrix} \mathbf{X}_i^a \\ \mathbf{X}_j^a \end{Bmatrix} = -\begin{bmatrix} \mathbf{K}_{ig}^* \\ \mathbf{K}_{jg}^* \end{bmatrix} \mathbf{X}_g \tag{6.22}$$

in which

$$\begin{bmatrix} \mathbf{K}_{ii}^* & \mathbf{K}_{ij}^* \\ \mathbf{K}_{ji}^* & \mathbf{K}_{jj}^* \end{bmatrix} = \left\{ \begin{bmatrix} \mathbf{K}_{ii} & \mathbf{K}_{ij} \\ \mathbf{K}_{ji} & \mathbf{K}_{jj} \end{bmatrix} - \begin{bmatrix} \mathbf{K}_{ik} \\ \mathbf{K}_{jk} \end{bmatrix} \mathbf{K}_{kk}^{-1} \begin{bmatrix} \mathbf{K}_{ki} & \mathbf{K}_{kj} \end{bmatrix} \right\} \tag{6.23}$$

and

$$\begin{bmatrix} \mathbf{K}_{ig}^* \\ \mathbf{K}_{jg}^* \end{bmatrix} = \left\{ \begin{bmatrix} \mathbf{K}_{ig} \\ \mathbf{K}_{jg} \end{bmatrix} - \begin{bmatrix} \mathbf{K}_{ik} \\ \mathbf{K}_{jk} \end{bmatrix} \mathbf{K}_{kk}^{-1} \mathbf{K}_{kg} \right\} \tag{6.24}$$

The static equations of motion shown in Eq. (6.5) can be condensed in a similar manner such that the condensed pseudo-static displacement can be expressed as:

$$\begin{Bmatrix} \mathbf{X}_i^{ps} \\ \mathbf{X}_j^{ps} \end{Bmatrix} = -\begin{bmatrix} \mathbf{K}_{ii}^* & \mathbf{K}_{ij}^* \\ \mathbf{K}_{ji}^* & \mathbf{K}_{jj}^* \end{bmatrix}^{-1} \begin{bmatrix} \mathbf{K}_{ig}^* \\ \mathbf{K}_{jg}^* \end{bmatrix} \mathbf{X}_g = \mathbf{R}_v^* \mathbf{X}_g \tag{6.25}$$

where $\mathbf{R}_v^* = -\begin{bmatrix} \mathbf{K}_{ii}^* & \mathbf{K}_{ij}^* \\ \mathbf{K}_{ji}^* & \mathbf{K}_{jj}^* \end{bmatrix}^{-1} \begin{bmatrix} \mathbf{K}_{ig}^* \\ \mathbf{K}_{jg}^* \end{bmatrix}$ is called the condensed influence factor matrix. Substituting $\begin{Bmatrix} \mathbf{X}_i^a \\ \mathbf{X}_j^a \end{Bmatrix} = \begin{Bmatrix} \mathbf{X}_i^d \\ \mathbf{X}_j^d \end{Bmatrix} + \begin{Bmatrix} \mathbf{X}_i^{ps} \\ \mathbf{X}_j^{ps} \end{Bmatrix}$ into Eq. (6.22), we obtain the condensed EOM-rel as below:

$$\begin{bmatrix} \mathbf{M}_i & \mathbf{0} \\ \mathbf{0} & \mathbf{0} \end{bmatrix} \begin{Bmatrix} \ddot{\mathbf{X}}_i^d \\ \ddot{\mathbf{X}}_j^d \end{Bmatrix} + \begin{bmatrix} \mathbf{K}_{ii}^* & \mathbf{K}_{ij}^* \\ \mathbf{K}_{ji}^* & \mathbf{K}_{jj}^* \end{bmatrix} \begin{Bmatrix} \mathbf{X}_i^d \\ \mathbf{X}_j^d \end{Bmatrix} = -\begin{bmatrix} \mathbf{M}_i & \mathbf{0} \\ \mathbf{0} & \mathbf{0} \end{bmatrix} \begin{bmatrix} \mathbf{K}_{ii}^* & \mathbf{K}_{ij}^* \\ \mathbf{K}_{ji}^* & \mathbf{K}_{jj}^* \end{bmatrix}^{-1} \begin{bmatrix} \mathbf{K}_{ig}^* \\ \mathbf{K}_{jg}^* \end{bmatrix} \mathbf{X}_g \tag{6.26}$$

Eqs. (6.22) and (6.26) are typical equations of motion where all unknown terms are on the left side of equation while known forces terms are on the right side of the equation. The stiffness matrices in Eqs. (6.22) and (6.26) can either be obtained by using Eqs. (6.23) and (6.24), if the component stiffness matrices are known from structural analysis packages, or can be obtained from experimental tests by applying small displacements to each DOF and measuring the reaction forces.

6.4.2 Hybrid simulation procedure with MSE

The operator splitting method in conjunction with α-modified Newmark scheme (α-OS) (Combescure and Pegon, 1997) is implemented in UI-SimCor (Kwon, 2007). The Operator-Splitting (OS) method implements an implicit algorithm without iteration while the α-modified Newmark scheme tends to numerically damp spurious high-frequency oscillations. The algorithm was found to be unconditionally stable if the tangent stiffness is not greater than the elastic stiffness of the structure, which is the case for most of the civil engineering structures. For both the EOM-abs formulation and the EOM-rel approximation, the complications introduced by MSE can be easily accommodated by changing the applied force vector in the equation of motion and converting the absolute or dynamic displacements into relative displacements before

sending commands to each substructure. First, based on the condensed mass and stiffness matrices in Eqs. (6.22) and (6.26), the corresponding damping matrices can be formulated assuming proportional damping:

$$\mathbf{C}_{ss}^{*}=a_0\mathbf{M}_{ss}^{*}+a_1\mathbf{K}_{ss}^{*},\ \mathbf{C}_{sg}^{*}=-\mathbf{C}_{ss}^{*}\mathbf{R}_{v}^{*} \tag{6.27}$$

in which

$$\mathbf{M}_{ss}^{*}=\begin{bmatrix}\mathbf{M}_{i} & \\ & \mathbf{0}_{j}\end{bmatrix},\ \mathbf{K}_{ss}^{*}=\begin{bmatrix}\mathbf{K}_{ii}^{*} & \mathbf{K}_{ij}^{*}\\ \mathbf{K}_{ji}^{*} & \mathbf{K}_{jj}^{*}\end{bmatrix},\ \mathbf{K}_{sg}^{*}=\begin{bmatrix}\mathbf{K}_{ig}^{*}\\ \mathbf{K}_{jg}^{*}\end{bmatrix} \tag{6.28}$$

The constants a_0 and a_1 can be chosen to produce specified modal damping factors for two selected modes (Craig and Kurdila, 2006). By adding the damping matrices to the condensed equations of motion, we can obtain the complete equations of motion which are the basis of the hybrid simulation procedures.

For EOM-abs, adding the damping matrices to Eq. (6.21), we have the complete equation of motion as follows:

$$\mathbf{M}_{ss}^{*}\mathbf{a}(t)+\mathbf{C}_{ss}^{*}\mathbf{v}(t)+\mathbf{C}_{sg}^{*}\dot{\mathbf{X}}_{g}+\mathbf{K}_{ss}^{*}\mathbf{d}(t)+\mathbf{K}_{sg}^{*}\mathbf{X}_{g}=\mathbf{0} \tag{6.29}$$

or

$$\mathbf{M}_{ss}^{*}\mathbf{a}(t)+\mathbf{C}_{ss}^{*}\mathbf{v}(t)+\mathbf{r}(t)=\mathbf{f}(t) \tag{6.30}$$

In Eqs. (6.29) and (6.30),

$$\mathbf{a}(t)=\begin{Bmatrix}\ddot{\mathbf{X}}_{i}^{a}\\ \ddot{\mathbf{X}}_{j}^{a}\end{Bmatrix},\ \mathbf{v}(t)=\begin{Bmatrix}\dot{\mathbf{X}}_{i}^{a}\\ \dot{\mathbf{X}}_{j}^{a}\end{Bmatrix},\ \mathbf{d}(t)=\begin{Bmatrix}\mathbf{X}_{i}^{a}\\ \mathbf{X}_{j}^{a}\end{Bmatrix},\ \mathbf{r}(t)=\mathbf{K}_{ss}^{*}\mathbf{d}(t)+\mathbf{K}_{sg}^{*}\mathbf{X}_{g},\ \mathbf{f}(t)=-\mathbf{C}_{sg}^{*}\dot{\mathbf{X}}_{g} \tag{6.31}$$

For the EOM-rel approximation, adding the damping matrices to Eq. (6.26), we have the complete equation of motion as follows:

$$\mathbf{M}_{ss}^{*}\mathbf{a}(t)+\mathbf{C}_{ss}^{*}\mathbf{v}(t)+\mathbf{K}_{ss}^{*}\mathbf{d}(t)=-\mathbf{M}_{ss}^{*}\mathbf{R}_{v}^{*}\ddot{\mathbf{X}}_{g} \tag{6.32}$$

or

$$\mathbf{M}_{ss}^{*}\mathbf{a}(t)+\mathbf{C}_{ss}^{*}\mathbf{v}(t)+\mathbf{r}(t)=\mathbf{f}(t) \tag{6.33}$$

In Eqs. (6.32) and (6.33),

$$\mathbf{a}(t)=\begin{Bmatrix}\ddot{\mathbf{X}}_{i}^{d}\\ \ddot{\mathbf{X}}_{j}^{d}\end{Bmatrix},\ \mathbf{v}(t)=\begin{Bmatrix}\dot{\mathbf{X}}_{i}^{d}\\ \dot{\mathbf{X}}_{j}^{d}\end{Bmatrix},\ \mathbf{d}(t)=\begin{Bmatrix}\mathbf{X}_{i}^{d}\\ \mathbf{X}_{j}^{d}\end{Bmatrix},$$

$$\mathbf{r}(t)=\mathbf{K}_{ss}^{*}\mathbf{d}(t),\ \mathbf{f}(t)=-\mathbf{M}_{ss}^{*}\mathbf{R}_{v}^{*}\ddot{\mathbf{X}}_{g} \tag{6.34}$$

Then, according to Combescure and Pegon (2007), the hybrid simulation procedure using either the EOM-abs formulation or the EOM-rel approximation in conjunction with the α-OS scheme in the case of MSE are outlined in Fig. 6.6.

1. Choose Δt

   Evaluate $\hat{\mathbf{M}}$

   $$\hat{\mathbf{M}} = \mathbf{M}_{ss}^{*} + \gamma\Delta t(1+\alpha)\mathbf{C}_{ss}^{*} + \beta\Delta t^{2}(1+\alpha)\mathbf{K}_{ss}^{*}$$

2. Set n = 0

   Initialize $\hat{\mathbf{d}}_0, \mathbf{d}_0 = \tilde{\mathbf{d}}_0, \mathbf{v}_0, \mathbf{a}_0, \tilde{\mathbf{r}}_0,$ and $\mathbf{f}_0$

3. Input excitation $\mathbf{f}_{n+1}$

4. Compute $\tilde{\mathbf{d}}_{n+1}$ and $\mathbf{v}_{n+1}$

   $$\tilde{\mathbf{d}}_{n+1} = \mathbf{d}_n + \Delta t\mathbf{v}_n + \frac{\Delta t^{2}}{2}(1-2\beta)\mathbf{a}_n$$
   $$\tilde{\mathbf{v}}_{n+1} = \mathbf{v}_n + \Delta t(1-\gamma)\mathbf{a}_n$$

5. For the EOM-abs formulation, impose $\tilde{\mathbf{d}}_{n+1} - \mathbf{X}_g(n+1)$ to the structure

   For the EOM-rel approximation, impose $\tilde{\mathbf{d}}_{n+1} + \mathbf{R}_{v}^{*}\mathbf{X}_g(n+1) - \mathbf{X}_g(n+1)$ to the structure

6. Measure restoring force, $\tilde{\mathbf{r}}_{n+1}^{m}$, and displacement, $\tilde{\mathbf{d}}_{n+1}^{m}$

7. Compute $\mathbf{r}_{n+1}^{m} = \tilde{\mathbf{r}}_{n+1}^{m} - \mathbf{K}_{ss}^{*}\left(\tilde{\mathbf{d}}_{n+1}^{m} - \tilde{\mathbf{d}}_{n+1}\right)$

8. Compute $\tilde{\mathbf{f}}_{n+1} = (1+\alpha)\mathbf{f}_{n+1} - \alpha\mathbf{f}_n + \alpha\tilde{\mathbf{r}}_n - (1+\alpha)\tilde{\mathbf{r}}_{n+1} + \alpha\mathbf{C}_{ss}^{*}\tilde{\mathbf{v}}_n$
   $$-(1+\alpha)\mathbf{C}_{ss}^{*}\tilde{\mathbf{v}}_{n+1} + \alpha\left(\gamma\Delta t\mathbf{C}_{ss}^{*} + \beta\Delta t^{2}\mathbf{K}_{ss}^{*}\right)\mathbf{a}_n$$

9. Solve for $\mathbf{a}_{n+1}$ from $\hat{\mathbf{M}}\mathbf{a}_{n+1} = \hat{\mathbf{f}}_{n+1}$

10. Compute $\mathbf{d}_{n+1}$ and $\mathbf{v}_{n+1}$

    $$\mathbf{d}_{n+1} = \tilde{\mathbf{d}}_{n+1} + \Delta t^{2}\beta\mathbf{a}_{n+1}$$
    $$\mathbf{v}_{n+1} = \tilde{\mathbf{v}}_{n+1} + \Delta t\gamma\mathbf{a}_{n+1}$$

11. Set $n = n+1$ and go to step 3

Figure 6.6 Implementation of the α-OS method for the hybrid simulation with MSE.

In the case of the EOM-abs formulation, the fact that the applied force term $\mathbf{f}(t)$ in Eq. (6.33) depends only on damping and ground velocity might be confusing, because when damping is zero, there seems to be no external force to excite the structure. However, if one considers Step 5, the displacement applied to each substructure is the difference between the calculated absolute displacement and the ground displacement. Therefore, the ground displacement drives the initial time-stepping process.

Typically, substructures are fixed at one end and the relative displacements are applied at other DOFs. In the case of uniform ground excitation, the solution of the equations of motion can yield directly the relative displacements. If the substructure is connected to the ground, which is also fixed in the experiment, the relative displacements are readily applied to the control points. However, in the case of MSE, if one substructure is subjected to more than one ground motion,

only one of the ground nodes can be fixed and the rest of the nodes are treated as control points, where the relative displacements with respect to the fixed ground node are applied.

The proposed procedures are applied to a four-span freeway bridge to further investigate the error introduced by using the EOM-rel approximation based on real engineering structures.

6.5 Application to Santa-Monica Freeway Ramp Bridge

6.5.1 Bridge description and finite element modeling

The prototype bridge considered is the ramp structure of the Collector-Distributor 36 of the Santa-Monica Freeway (I-10), which was severely damaged during the Northridge Earthquake of 17 January 1994. It is a reinforced concrete continuous box-girder bridge with circular piers monolithically connected to the deck. Reference can be made to Broderick and Elnashai (1995) and Elnashai et al. (2005) for detailed information about this bridge.

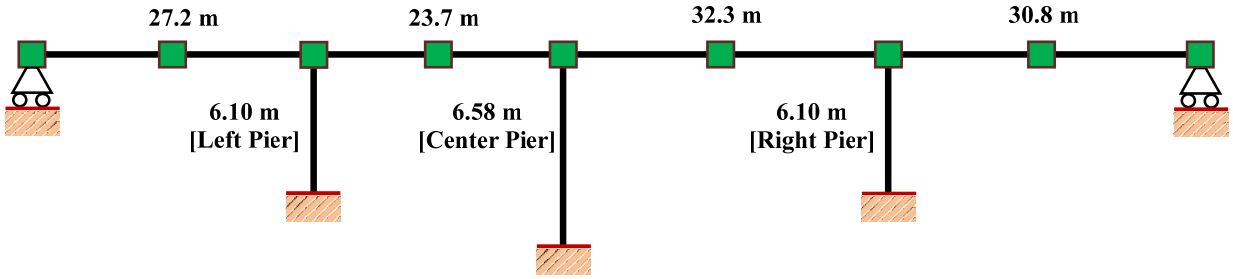

Figure 6.7 Layout of the Santa Monica Ramp Bridge (not to scale).

The bridge is simplified as a four-span bridge with three piers, as shown in Fig. 6.7. Finite element model is built in Zeus-NL (Elnashai et al., 2004). The deck section is a three-cell continuous RC box section but is equivalently modeled as an I-section with equal flange and web sizes. Linear elastic material is used to represent the deck, and hence no nonlinearity is allowed to develop. The three piers have identical cross section and are modeled with a uniaxial constant confinement concrete model. Lumped masses are calculated and placed along the deck. 2% damping is added to the first two modes of the structure by assuming proportional damping. As a result, the third to the seventh mode has damping which is slightly higher than 2%, but still less than 3%. Damping is higher beyond the seventh mode; however, because the first seven modes contribute 99.3% of the total modal mass, the overall response is not affected. Additionally, soil structure interaction (SSI) is neglected in this analysis, as the goal of this application is to compare the two formulations of the EOM's; therefore, the piers are assumed rigidly connected to the ground, while the two ends of the bridge are assumed restrained only in the vertical direction. The weight of the bridge is calculated and applied on top of the piers as an initial gravity load.

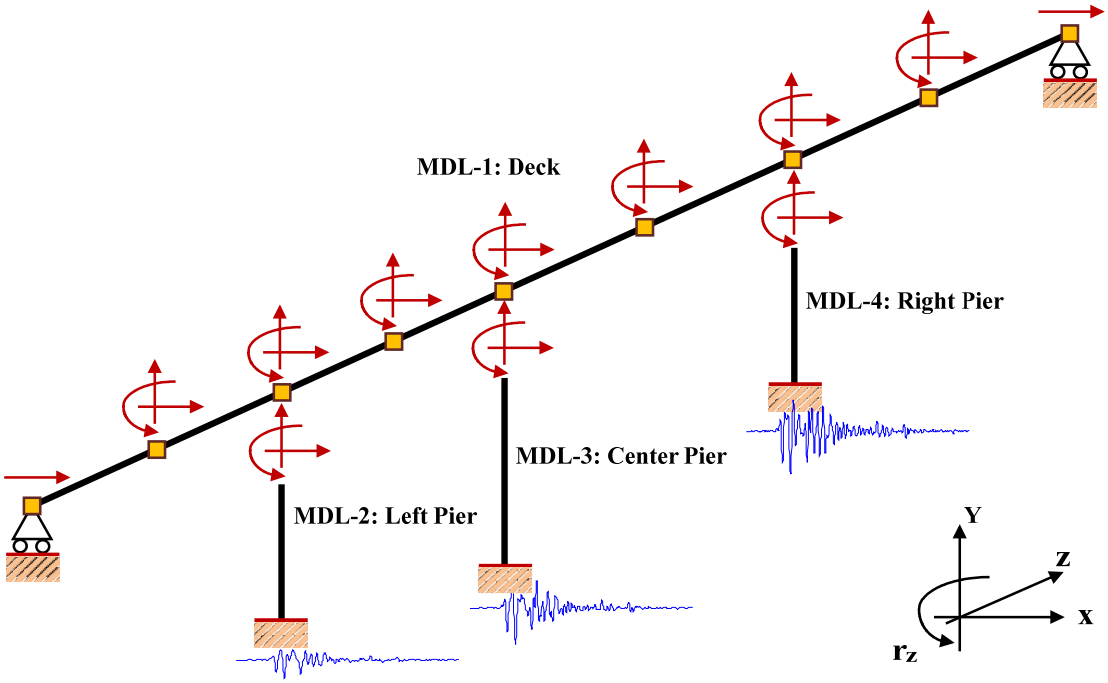

Figure 6.8 Sub-structures and effective DOFs.

6.5.2 Sub-structuring and input ground motions

To facilitate hybrid simulation, the bridge is partitioned into four sub-structures, namely the left pier, the center pier, the right pier, and the deck. The four sub-structures and their effective DOFs are shown in Fig. 6.8. The transverse motion of the bridge is selected for analysis. The model of each substructure is built in Zeus-NL as static analysis module, while UI-Simcor is used to coordinate between the four substructures to carry out the time-stepping integration with the α-OS scheme based on the two EOM formulations.

Among the multiple sources for asynchronous ground motion as discussed previously, the local site effect is considered in this study. The soil conditions at the locations of the three piers are assumed to be quite different, namely, soft, median and stiff soils for the left, center and right piers, respectively. The corresponding shear wave velocities are 360 m/s, 760 m/s and 1500 m/s. To introduce large nonlinearities into the bridge piers, the ground motion recorded during the Kobe earthquake of Jan. 16, 1995 at the JMA station is selected as the rock outcrop motion. 1-D site response analyses are then conducted using DEEPSOIL (Hashash et. al., 2009) to generate the surface ground motions, which are depicted in Fig. 6.9. Due to the different site conditions, the surface ground motions are quite different in terms of both amplitude and frequency content.

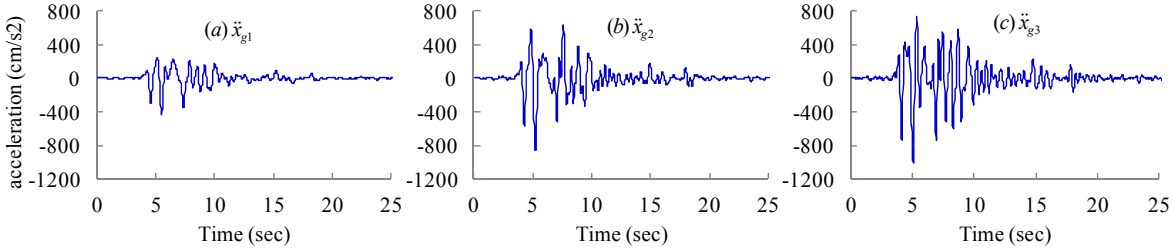

Figure 6.9 Ground motion inputs to the three piers: (a) left pier; (b) center pier; (c) right pier.

6.5.3 Simulation results and comparison

Following the procedures of hybrid simulation based on the EOM-abs formulation and the EOM-rel approximation, respectively, as proposed in the preceding section, simulations are conducted for the the Santa-Monica Ramp Bridge. To damp out any potential spurious high-mode responses, a value of 0.05 is used for α in the α-OS method. Additionally, dynamic time history analyses for the whole bridge model are also carried out in Zeus-NL as a baseline for comparison with hybrid simulation results.

The deformation time histories of the three piers in the transverse direction and the corresponding hysteresis loops are plotted in Fig. 6.10. The responses from hybrid simulations with EOM-abs match well with those from the complete bridge analyses in Zeus-NL, which verifies that all nonlinear terms are naturally included in the restoring force term in EOM-abs. The RMS (Root Mean Square) errors of the responses of the EOM-rel approximation are 9.85%, 16.69% and 9.64% for the left, center and right piers, respectively, due to ignoring the change of stiffness of the piers. .

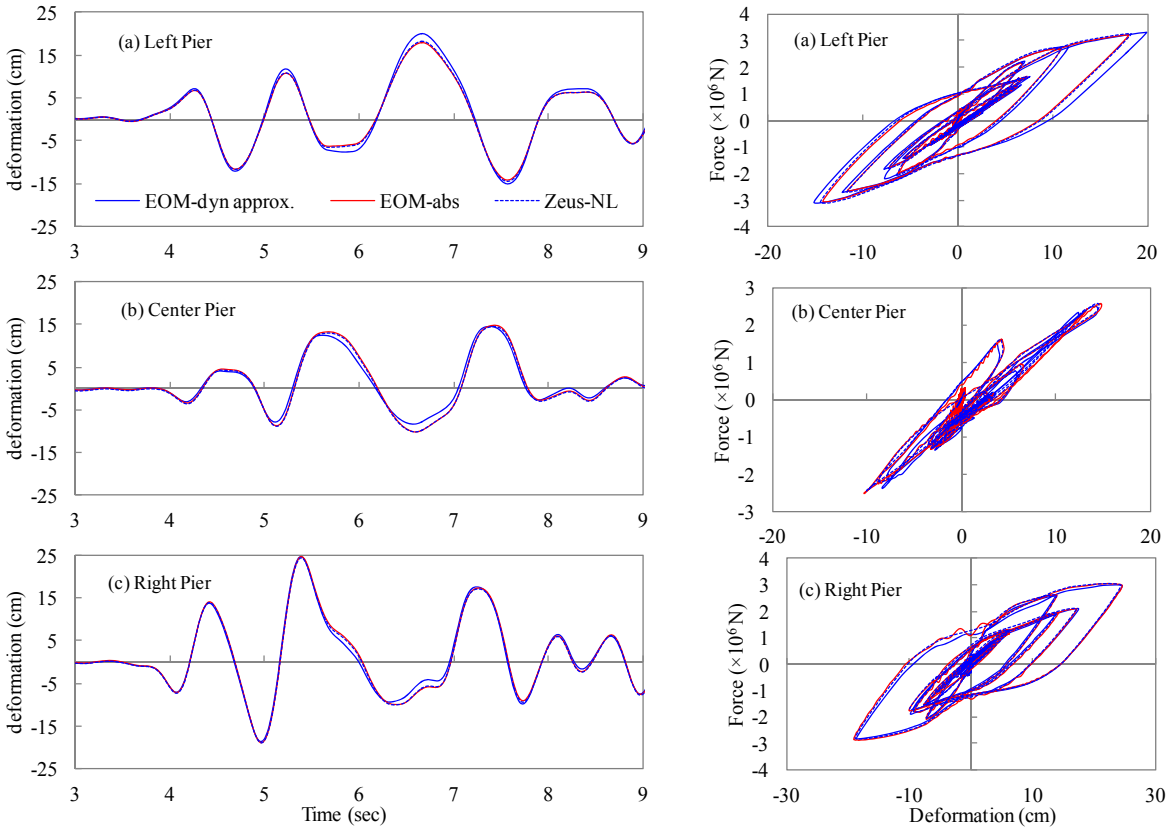

Figure 6.10 Deformation time histories and hysteresis loops of the three piers.

A parametric study is carried out considering different deck stiffnesses; recall that the relative stiffness among the deck and piers affects the influence matrix and hence the error in the response when using the EOM-rel approximation. The stiffness of the deck is changed by changing the Young's modulus from 0.1 to 1000 of the original value E_0. Figure 6.11 shows that when the deck stiffness is increased, the RMS errors of the piers responses are consistently

decreased, implying that when the stiffness change does not contribute significantly to the overall stiffness matrix of the structure, the EOM-rel approximation provides results with good accuracy. On the other hand, the error can be significant if the nonlinear component dominants the overall stiffness matrix. In such cases, the EOM-abs is recommended.

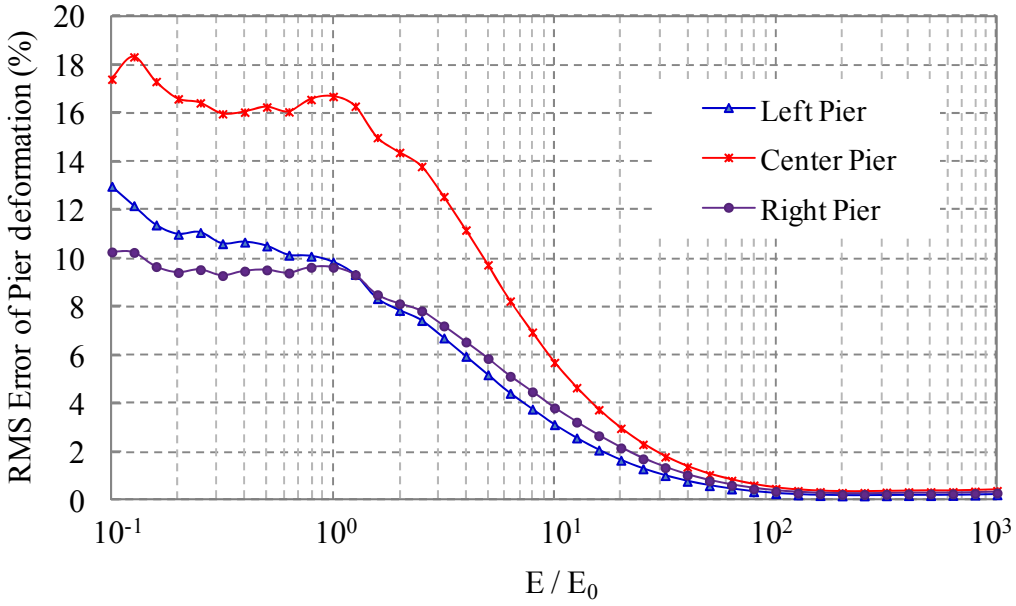

Figure 6.11 The change of RMS errors of pier deformations with the change of deck stiffness.

6.6 Summary

Hybrid simulation with multiple-support excitation has been investigated in this chapter. The two formulations of equations of motion for MSE have been carefully examined and compared. The formulation in relative coordinates, which has been widely adopted in conventional time history analysis of MSE problems, may produce large error in hybrid simulation if the experimental substructures undergo large nonlinearity and the change of stiffness in the experimental substructures plays a major role in the global stiffness of the structure. The formulation in absolute coordinates was therefore recommended for hybrid simulation and was incorporated into UI-SimCor, allowing accommodating of a wider range of earthquake excitation scenarios. With the developed theoretical basis and practical tool, hybrid simulation can be performed for structures subjected MSE to generate experimental data for improving fragility function estimation through Bayesian updating.

NEES INTEGRATED SEISMIC RISK ASSESSMENT FRAMEWORK

In this chapter, a framework, referred to as NEES Integrated Seismic Risk Assessment Framework, or NISRAF, has been described which integrates hybrid simulations with free-field and structure sensor measurements, hazard characterization, system identification-based model updating technology, probabilistic fragility analysis, and earthquake risk assessment. The system identification, model updating, hybrid simulation and fragility analysis components have been developed in this research to facilitate high-fidelity fragility analysis. First, the background and motivation are introduced. Then the architecture of the NISRAF is illustrated, followed by the description of each component implemented in the integrated platform. Finally, an example based on a six-story steel building is then presented.

7.1 Introduction

The fundamental objectives of research fields in earthquake engineering are seismic loss estimation and mitigation. Individual sub-disciplines have been focused on specific problems within earthquake risk research, such as strong motion measurement, system identification, model updating, structural performance evaluation through experimental or nonlinear analysis, fragility derivation, and development of loss estimation frameworks. The isolated studies allow researchers to focus on a particular problem at a fundamental level. Even though these fields of studies have progressed considerably and produced mature research outcomes, large uncertainties remain in the outcomes. These uncertainties may be reduced through integration of models and knowledge from different sub-disciplines. For instance, nonlinear analyses are essential for fragility relationship derivation. The most sophisticated models are still subject to very large uncertainties due to the uncertainty in model parameter estimation. As has been illustrated and proved in Chapter 5, in hybrid simulation, the experimental specimen alongside numerically represented components should be very well calibrated to replicate the behavior of real structures. Strong motion measurements from instrumented structures are being used to monitor structural integrity and to identify structural properties, such as the example presented in Chapter 4. The reliability of probabilistic seismic hazard can be significantly improved through free field strong motion measurements. The results of a limited number of hybrid simulations can be used to derive more reliable fragilities than those based on analysis alone. The Bayesian updating approach described in Chapter 5 is one of the examples. Different approaches are also available such as the iterative approach through a series of tests (Lin, 2010), which will be introduced in later section. The derived fragilities, with improved accuracy, and the calibrated hazard model are then fed into seismic loss assessment framework such as MAEviz and HAZUS. Systematic integration of these interdependent components can greatly reduce the uncertainties arising from engineering judgment and lead to more reliable seismic risk assessment.

7.2 Architecture of NISRAF

As illustrated in Fig. 7.1, the proposed framework consists of five components: seismic hazard characterization, system identification-based model calibration, hybrid simulation, fragility analysis, and earthquake risk assessment. Sensor instrumentation feeds structure and ground response data to modeling. Structural modeling leads to hybrid simulation using the most optimally tuned structure models, the results of which are used to derive calibrated fragility

relationships that are needed in earthquake risk assessment software, such as MAEviz and HAZUS. The ground modeling leads to advanced hazard representations that also employ site response to derive the best possible ground motion records for use with the tuned structure models.

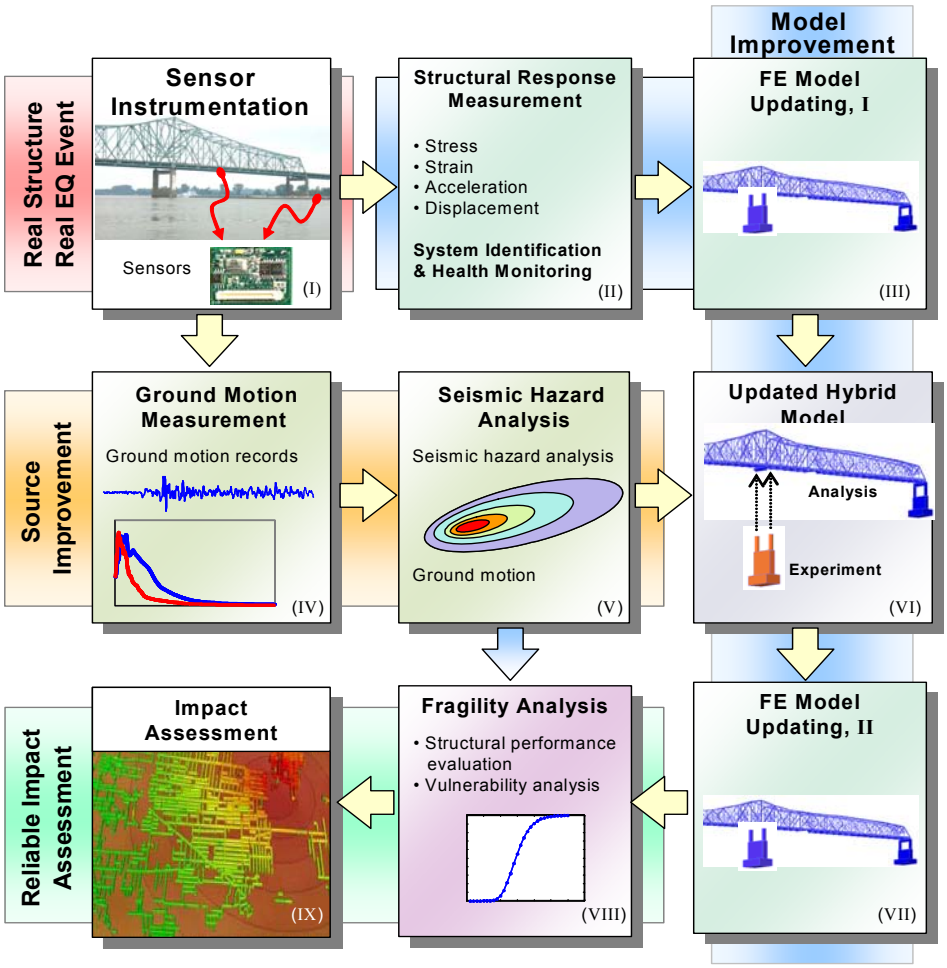

Figure 7.1 Architecture of NISRAF

7.3 NISRAF Components

NISRAF has been developed in MATLAB (Mathworks, 2009). The five interdependent components integrated in NISARF are described in detail in this section.

7.3.1 Seismic hazard characterization

An integrated hazard characterization analysis approach (Lin, 2010) has been implemented in NISRAF, which provides functionalities for both synthetic ground motion and hazard map generation. Three cases are considered in the seismic hazard characterization module.

Case 1 is when ground motion records from historic earthquakes are available at the target location. In such case, the available ground motion records are analyzed to obtain the response spectra of these records. Spectrum-compatible synthetic ground motions are then generated. SIMQKE (Gasparini and Vanmarcke, 1976) is employed and integrated in NISRAF

for generating these synthetic ground motions. NISRAF provides user-friendly interface for collecting parameters from users which are related to generating the input files for SIMQKE, such as the response spectra, duration, and intensity functions. If the available ground motions are measured from bedrock, then the above procedure can generate synthetic ground motions at the bedrock level. In this case, local site effect has to be taken into account. NISRAF has integrated the 1-D site response analysis program called DEEPSOIL (Hashash et al., 2009) to allow these bedrock motions to propagate through the user-defined soil column to the ground surface, hence generating surface ground motions which reflect the local site effect.

Case 2 is when no historic ground motion is available. User-supplied response spectra or these predicted by the ground motion attenuation model are accepted in NISARF. The next generation attenuation (NGA) model (Campbell and Bozorgnia, 2008) has been incorporated in NISRAF. After the response spectra are made ready, the rest of the procedure is the same as in case 1 to generate synthetic surface ground motions for hybrid simulation and fragility function estimation.

Case 3 is for generating hazard map for the area of interest. Hazard map is generated by leveraging the function provided in case 1 and case 2. The basic idea is that the area of interest is meshed into small cells, and spectrum-compatible synthetic ground motion at the center of each cell is generated using the approach describe above. The seismic intensity of each synthetic ground motion, such as PGA, is then calculated. The intensity values, along with the geographical coordinates, are synthesized to obtain the hazard map.

The above hazard characterization module implemented in NISRAF integrates seismic hazard analysis, synthetic ground motion generation, site response analysis, and hazard map generation. The use of instrumentation data provides an opportunity to calibrate the hazard model, and hence improves the reliability of the hazard characterization. In addition, the incorporation of site response analysis allows realistic surface ground motion to be generated, which may better reflect the situation of ground shaking that the target structure would experience in real earthquakes.

7.3.2 System identification-based model calibration

Among the various system identification methods, the Eigensystem Realization Algorithm (ERA) (Juang and Papa, 1985) is implemented in NISRAF due to its wide application and good performance in multi-input multi-output (MIMO) problems. The basic idea of ERA is to find a minimum realization of the system (a state-space representation with minimum dimensions) using the Singular Value Decomposition (SVD) on the Hankel matrix built by the Markov parameters (impulse response functions), so that the modal properties can be extracted from the realized minimum state-space representation. First, for a system with the numbers of input and output equal to p and q, respectively, the impulse response function $\mathbf{Y}$ is obtained by performing Inverse Fast Fourier Transform (IFFT) with transfer functions. Then, the following Hankel matrix is constructed:

$$\mathbf{H}_{rs}(k)=\begin{bmatrix} \mathbf{Y}(k) & \mathbf{Y}(k+1) & \mathbf{Y}(k+2) & \cdots & \mathbf{Y}(k+s-1) \\ \mathbf{Y}(k+1) & \mathbf{Y}(k+2) & \mathbf{Y}(k+3) & \cdots & \mathbf{Y}(k+s) \\ \mathbf{Y}(k+2) & \mathbf{Y}(k+3) & \mathbf{Y}(k+4) & \cdots & \mathbf{Y}(k+s+1) \\ \vdots & \vdots & \vdots & \ddots & \vdots \\ \mathbf{Y}(k+r-1) & \mathbf{Y}(k+r) & \mathbf{Y}(k+r+1) & \cdots & \mathbf{Y}(k+r+s-2) \end{bmatrix} \tag{7.1}$$

in which $\mathbf{Y}(k)$ is the impulse response function at time k, a block matrix consisting of p rows and q columns; r and s are the number of block rows and block columns; Singular value decomposition is then carried out for $\mathbf{H}_{rs}(k)$, which yields:

$$\mathbf{H}_{rs}(0) = \underline{\mathbf{P}}\underline{\mathbf{D}}\underline{\mathbf{Q}}^T \tag{7.2}$$

where $\underline{\mathbf{P}}$ and $\underline{\mathbf{Q}}$ are left and right singular vectors. $\underline{\mathbf{D}}$ is an $(r\times p)$ by $(s\times q)$ diagonal matrix with singular values on the diagonal. If $\mathbf{Y}$(k) is noise free, the number of non-zero singular values is the dimension of the minimum realization of the system. However, due to noise in reality, $\underline{\mathbf{D}}$ usually has full rank. The singular values associated with noise are usually much smaller compared with those corresponding to real modes. By preserving the first N biggest singular values, by which noise modes are eliminated, the minimum realization of the state space system can be calculated as

$$\begin{aligned}
\mathbf{A} &= \mathbf{D}^{-1/2}\mathbf{P}^T\mathbf{H}_{\mathrm{rs}}(1)\mathbf{Q}\mathbf{D}^{-1/2} \\
\mathbf{B} &= \mathbf{D}^{1/2}\mathbf{Q}\mathbf{E}_q \\
\mathbf{C} &= \mathbf{E}_p^T\mathbf{P}\mathbf{D}^{1/2}
\end{aligned} \tag{7.3}$$

In the above equations, $\mathbf{E}_p^T = [\mathbf{I}_p\ \mathbf{0}_p \cdots \mathbf{0}_p]$ and $\mathbf{E}_q^T = [\mathbf{I}_q\ \mathbf{0}_q \cdots \mathbf{0}_q]$. The above state space matrices are then transformed into modal coordinates by using the eigenvalues $\mathbf{Z}$ and the eigenvector matrix of $\mathbf{A}$, which yields:

$$\begin{aligned}
\mathbf{A}' &= \mathbf{\Psi}^{-1}\mathbf{A}\mathbf{\Psi} = \mathbf{Z} \\
\mathbf{B}' &= \mathbf{\Psi}^{-1}\mathbf{B} \\
\mathbf{C}' &= \mathbf{C}\mathbf{\Psi}
\end{aligned} \tag{7.4}$$

Mode shapes are the corresponding columns of $\mathbf{C}'$. The modal damping ratio, ξ_i and damped natural frequencies, ω_{di} can be calculated as

$$s_i = -\xi_i\omega_{ni} \pm i\omega_{di} = \ln(z_i)/\Delta t \tag{7.5}$$

where $\omega_{ni} = \omega_{di}/\sqrt{1-\zeta_i^2}$ are undamped natural frequencies, and Δt is the sampling interval.

As mentioned previously, measurements are always contaminated by noise in practice, resulting in nonzero values for all singular values in Eq. (7.2). Cutting of small singular values based on judgment does not guarantee reliable identification results. Therefore, the concept of stabilization diagram is employed to more effectively filter out noise modes, based on an idea that genuine modes should always exist in the system when the system order is increased. In NISRAF, the natural frequencies are identified for systems with different orders, by varying the number of retained singular values obtained in Eq. (7.2). For each particular order of the system, three mode accuracy indicators, namely, Modal Amplitude Coherence (MAC) (Juang and Pappa, 1985), Extended Modal Amplitude Coherence (EMAC), and Modal Phase Colinearity (MPC) (Pappa and Elliott, 1993) are used to eliminate the noise modes. The retained modes are plotted in a stabilization diagram. A mode which is identified for at least five times is considered stable and reliable. Among them, the one with highest EMAC value is then selected as the confirmed structural mode.

The model updating approach described in section 5.5.2 is implemented in NISRAF, which essentially takes the system identification result to form the objective function. The

implementation of model updating module takes advantage of the finite element modeling capability of NISRAF, which allows a structural model to be built within NISRAF, including geometry, structural elements, nodal connectivity, material properties, etc. Therefore, the candidate parameters are readily available and can be selected as needed. The objective function is customizable by including different number of modes and different weighting factors for frequencies and mode shapes. Sensitivity analysis is available to allow the appropriate parameters to be selected. Finally, model updating results, including the changes of the objective function, natural frequencies, mode shapes and the updating parameters, are summarized and displayed in tables. If the result is satisfactory and accepted, NISRAF updates the current model by incorporating the new parameters. Otherwise the model updating can be repeated with a different setup, such as optimization algorithm, objective function and candidate parameters, etc.

7.3.3 Hybrid Simulation

The hybrid simulation module was originally developed in SimBulid (Park et al., 2007), the pre- and post-processor for UI-SimCor. Taking advantage of the structural model built within NISRAF, substructures and effective DOFs can be defined and assigned conveniently in an interactive manner. The input files for UI-SimCor, including the configuration file, the ground motion input file, and the substructure models, are generated by NISRAF and are readily for use in UI-SimCor. Post-processing functions are also implemented to allow the results visually displayed in terms of graphs and animations.

7.3.4 Fragility analysis

Chapter 5 proposed a Bayesian approach to improve existing fragility functions based on a few hybrid simulation tests. If the fragility functions need to be generated based only on a limited number of hybrid simulation tests, the approach proposed by Lin (2010) can be adopted. In this approach, the median ground motion intensities (PGA, for example) of the fragility functions are estimated through laboratory tests, whereas the dispersion terms are adopted from literature.

To obtain the median ground motion intensities, a set of target structural responses is defined for the limit states. Then a few hybrid simulation tests are conducted with the goal of reaching the defined structural response by iterating on the scaling factor of ground motion input. For example, to find the median PGA for the immediate occupancy limit state, the PGA that will induce the target structure response is estimated through numerical analysis. A hybrid simulation test is then performed by using the estimated PGA value. If the measured peak response from the test is not equal to the target one, which is likely to happen due to the inaccuracy in the numerical model, the PGA is scaled based on the discrepancy and the hybrid simulation is repeated. This process is repeated for several times until the discrepancy is reduced with an acceptable tolerance. During the iteration process, the specimen may need to be replaced if it experienced apparent nonlinearity after one test.

7.3.5 Earthquake risk assessment

Through the previous components, NISRAF provides improved hazard map and fragility relationships. These results are formatted in an appropriated way such that they are compatible with earthquake risk assessment packages. Currently, the format of MAEviz is supported in NISRAF. MAEviz can be invoked from NISRAF and the compatible input files are readily fed into MAEviz for seismic risk assessment.

7.4 Application Example

7.4.1 Description of the selected structure and the finite element model

A six-story instrumented building (see Fig. 7.2) located in Burbank, California was selected to illustrate the use of NISRAF using the 1994 Northridge earthquake as the scenario event. This building is a steel moment resisting frame structure, in which the perimeter frames are the primary lateral load resisting system and the internal frames only resist the gravity load. According to the Strong Motion Instrumentation Program (SMIP) geotechnical report (Fumal et al., 1979), the top 30 meters of soil at the Burbank site is comprised of fine sandy loam, gravelly sand, and sandy loam and loamy sand. The average measured shear-wave velocity is 405 m/s in fine sandy loam, and 452 m/s in gravelly sand and sandy loam and loamy sand. The building was instrumented by the California Strong Motion Instrumentation Program (CSMIP) in 1980 with 13 sensor channels. Fig. 7.2 shows the plan view of the building and the sensor locations. Several significant earthquakes were captured, including the 1987 Whitter earthquake, the 1991 Sierra Madre earthquake and the 1994 Northridge earthquake. More details about the building and the site condition can be found in Anderson and Bertero (1991) and Fumal et al. (1979).

Figure 7.2 A six-story building in Burbank, California

The finite element model was built in NISRAF, as shown in Fig. 7.3. Due to the fact that only the perimeter frames are lateral load resistant system, a 2-D frame was modeled to represent the entire structure. Section dimensions and material properties for each beam and column were based on design documents. Lumped masses were used and applied at the beam-column connections. Concrete slabs were modeled and connected to the steel girders using rigid elements to account for their contribution to stiffness. The width of each slab was calculated based on the effective width defined in the ANSI/AISC 360-05 specification (AISC, 2005) and the distances to steel girders are based on the design drawings.

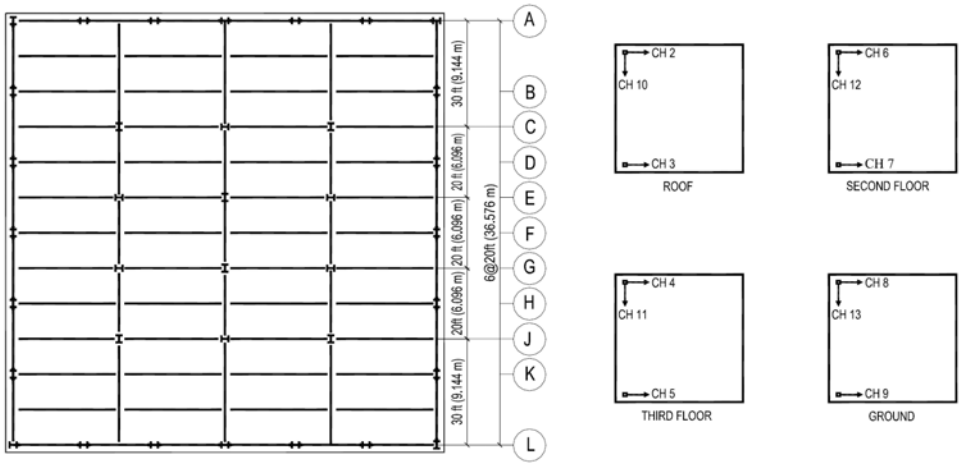

Figure 7.3 Plan view of Burbank building and sensor locations

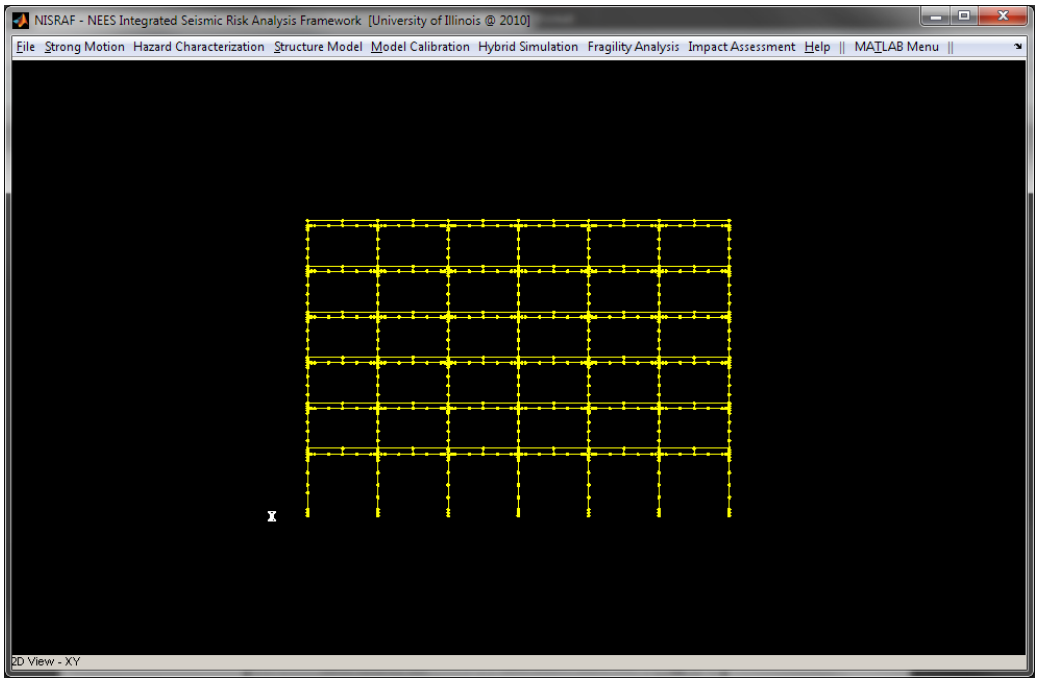

Figure 7.4 Analytical model for Burbank building built in NISRAF

7.4.2 Hazard characterization

Three sets of synthetic ground motions were generated for fragility function estimation, which corresponds to three hazard levels including 10%, 5% and 2% probability of exceedance in 50 years. First of all, the NGA model was calibrated using the measured free-field record from the 1994 Northridge earthquake (Lin, 2010). Then, similar to the description in section 5.6.2, seismic hazard deaggregation analysis was performed and the results were fed into NISRAF hazard characterization module. Synthetic ground motions were generated at the bedrock level and were

then passed through DEEPSOIL for site response analysis. Fig. 7.5 shows the time history and response spectrum of one synthetic ground motion in NISRAF.

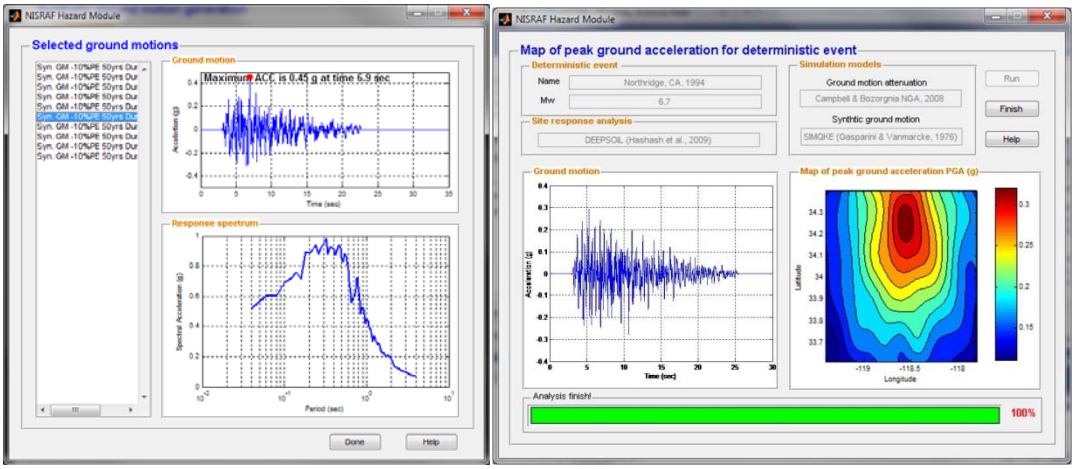

Figure 7.5 Synthetic ground motions and hazard map in NISRAF (Lin, 2010)

Hazard map was also generated in NISRAF for later seismic risk assessment in Los Angeles area. To have realistic site condition, the Los Angeles area was divided into 6 parts, each of them uses one borehole log to represent its site condition (Lin, 2010). The area is then divided into more refined cells. Synthetic ground motion was generated for each cell and the hazard map was created by collecting the PGA values from all the synthetic ground motions. Fig. 7.5 also depicts the generated hazard map in NISRAF.

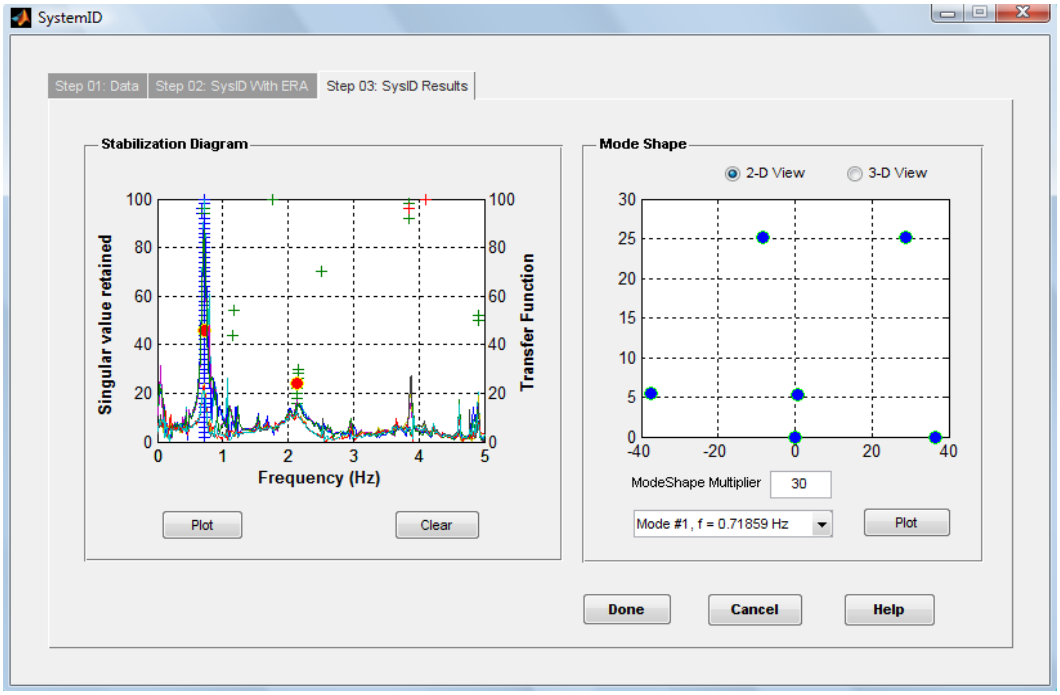

Figure 7.6 System identification of Burbank building

7.4.3 System identification and model calibration

Input channels and output channels were defined first in order to form impulse response functions which were assembled for the Hankel matrix. Based on the design drawings, exterior and interior columns are firstly supported on steel girders and reinforced concrete girders, respectively, and both of them are in turn supported on a pair of 32 feet long and 30 inches diameter reinforced concrete piles. Therefore, it is reasonable to consider that all columns are fixed. Hence, the records from the ground floor were treated as the input motions, while other records were considered as the responses of the structure. Consequently, channel 8 and 9 were defined as input, while channels 2 to 7 were output channels, and, hence, the dimension of impulse function matrices was 2 by 6. Note that channels 4 and 5 were not working properly during the Northridge earthquake of 1994. Therefore, data from these two channels were not available and only four output channels were available. The dimension of impulse response function matrices was 2 by 4 for the Northridge earthquake.

The ERA method was then performed for the Northridge earthquake record in NISRAF. The stabilization diagrams and the identified mode shapes were shown in Fig. 7.6. The first and second lateral bending modes were then identified as 0.72 Hz and 2.14 Hz, respectively. The associated damping ratios were 3.37% and 6.71%.

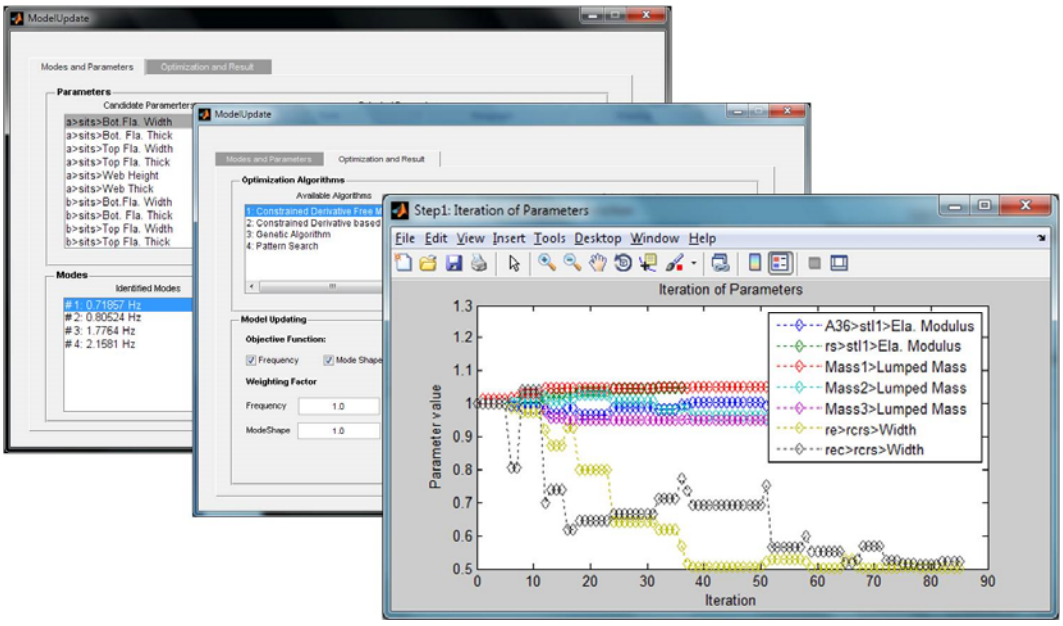

Figure 7.7 Model updating of Burbank building in NISRAF

With the identified natural frequencies and mode shapes, dynamic FE model updating was then performed to improve the FE model of the Burbank building. Parameters were selected based on the sensitivity of the first two modes to the selected parameters (see Table 7.1). To keep the physical meaning of each parameter, lower and upper bounds were applied based on the degree of uncertainties. For example, the effective widths were calculated based on AISC specification, which was likely to be very conservative. In addition, the deflection of the slab defined the contribution of the slab to the composite beam, thus affecting the effective width. Therefore, the effective width of slab had large uncertainty, thus a relatively larger range of variation (±50%) was applied.

The objective function was minimized by the Nelder-Mead method. Fig. 7.7 shows the GUI of the model updating module in NISRAF. The results listed in Table 7.2 show that the errors between the identified and updated model reduced to 1% and 5.78% for the first and second natural frequency, respectively. Meanwhile, the second mode shape was improved, which gave a value of 0.981 for the *MAC*. With this refined finite element model, hybrid simulation was conducted to yield a seismic response prediction with higher accuracy.

Table 7.1 Structural parameters before and after model updating

Updating parameters	Description	Initial Value	Bound (%)	Updated Value	Change (%)
Es (N/mm^2)	Young's modulus of steel	2.1×10^5	±5	2.21×10^5	5.00
Mass1 (10^3kg)	Lumped mass at 2nd floor	45.65	±5	43.37	-4.99
Mass2 (10^3kg)	Lumped mass at 3rd-5th floor	36.53	±5	38.36	5.01
Mass3 (10^3kg)	Lumped mass at top floor	54.84	±5	52.1	-5.00
WS1 (mm)	Effective width of concrete slab at 2nd-5th floor	762	±50	1143	50.00
WS2 (mm)	Effective width of concrete slab at top floor	914.4	±50	1371	49.93

Table 7.2 Modal parameters before and after model updating

Mode	Original FE model			Updated FE model		
	frequency (Hz)		*MAC*	frequency (Hz)		*MAC*
	value	error (%)		value	error (%)	
1	0.688	-4.312	0.999	0.712	-1.001	0.999
2	1.956	-8.769	0.975	2.020	-5.784	0.981

7.4.4 Fragility function estimation using hybrid simulation

Following the approach described in section 7.3.4, Lin (2010) performed eight hybrid simulation tests using three small-scale column specimens made by aluminum. Substructuring of the building structure is shown in Fig. 7.8 and Fig. 7.9. The lower part of the left column in the first storey is modeled experimentally with the aluminum column, while the rest of the structure is modeled numerically. Zeus-NL was selected as the static analysis module for the numerical substructure. Median PGA values corresponding to the three limit states, i.e. immediate occupancy, life safety and collapse prevention, were obtained from the tests. The dispersion of each limit state was adopted from FEMA 350 (FEMA, 2000). The generated fragility curves are shown in Fig. 7.6(b).

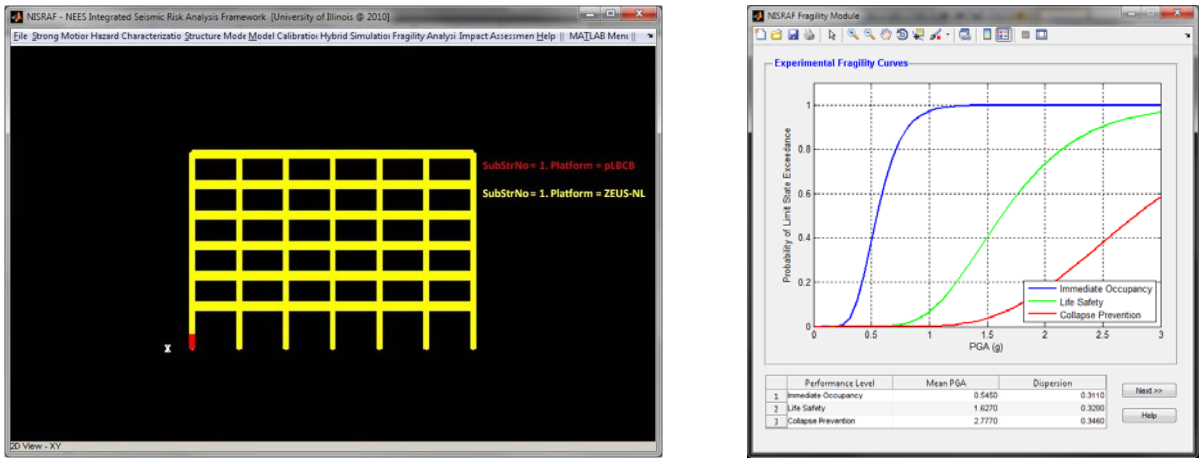

(a) Hybrid simulation model (b) Fragility curves

Figure 7.8 Hybrid simulation model of Burbank building and the estimated fragility curves (Lin, 2010)

7.4.5 Seismic risk assessment

With the hazard map and the fragility functions, seismic risk assessment was conducted in MAEviz to estimate the probability of damage of the Burbank building (Lin, 2010). The result listed in Table 7.3 shows 15% probability of exceeding the immediate occupancy limit state. The result based on MAEviz default fragility functions has 37% probably of exceeding the immediate occupancy limit state and 4% probability of exceeding the life safety limit state. However, based on the post-earthquake report made by the Applied Technology Council (ATC, 2001), this building was observed slight damage after the Northridge earthquake. Therefore, the risk assessment by NISRAF is more realistic than the one from using the MAEviz default fragility functions.

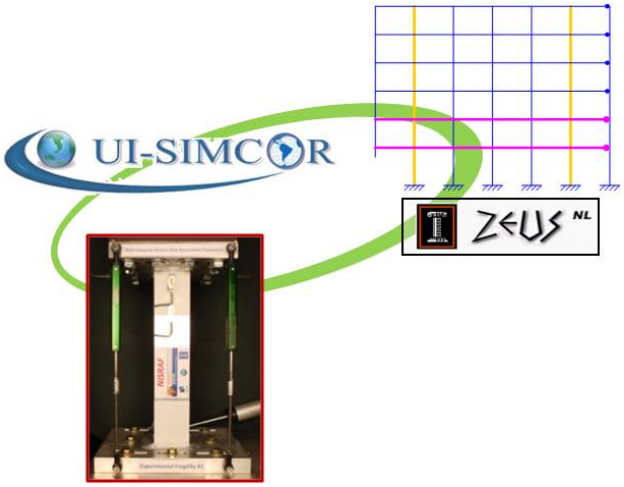

Figure 7.9 Analytical and experimental substructures of Burbank building (Lin, 2010)

Table 7.3 Comparison between seismic risk assessment results (Lin, 2010)

	Probability of exceeding limit state		
	Immediate Occupancy	Life Safety	Collapse Prevention
NISRAF	0.15	0.00	0.00
MAEviz default	0.37	0.04	0.00

7.5 Potential, Limitations, and Challenges

The proposed risk assessment framework delivers a scalable and extensible platform for risk assessment. It constitutes the first time that the integration of all components of risk assessment, including substructure hybrid simulation, has been attempted. Utilizing NISRAF, uncertainty estimation in loss estimation will become much easier than before and opportunities for reducing uncertainty through bringing the various research and development communities together will arise. In addition, NISRAF provides a stimulus to seismologists, geotechnical and structural earthquake engineers, and structural control and risk assessment experts to improve their algorithms to achieve reliable assessment of losses that would underpin mitigation, response and recovery planning.

NISRAF, in its current form, has limitations. As the first release of the framework, although basic functions in each component have been implemented which allow NISRAF to solve a broad spectrum of problems towards seismic risk assessment, more options or methods need to be added to make NISRAF more versatile. For example, the modeling function is only compatible with Zeus-NL; therefore, the defined numerical substructures can only be analyzed by Zeus-NL. Adding other finite element packages, such as OpenSees (McKenna and Fenves, 2001) and ABAQUS (Hibbit et al., 2001), etc., will allow NISRAF to accommodate more types of structural models. In the system identification module, ERA is the only algorithm implemented in NISRAF. However, other algorithms may be more suited for system identification using seismic measurements, such as the ARX method described in Chapter 5. Similarly, the inclusion of other model updating techniques will strengthen the capability of the model updating module of NISRAF. As mentioned before, NISARF is featured by its extensibility due to the modular design of each component. Therefore, new algorithms can be developed separately and then appended to NISRAF, as long as the data structure of NISRAF is used for the input and output of each component.

7.6 Summary

This chapter presents the NEES Integrated Seismic Risk Assessment Framework (NISRAF), which is composed of modularly designed components for seismic hazard characterization, system identification-based model updating, hybrid simulation, probability fragility analysis, and earthquake risk assessment. The design architecture of NISRAF has been described and each component has been introduced. NISRAF was then applied to estimate the fragility functions of a six-story building and the probability of damage of the building under the Northridge

earthquake. The result demonstrated that the methodology employed in NISRAF was able to give more accurate estimation than using the default fragility functions in MAEviz. Finally, the potential, limitations, and challenges of NISRAF were discussed.

CONCLUSIONS AND FUTURE STUDIES

8.1 Conclusions

This report presented an integrated approach to high-fidelity fragility analysis. The approach brings together a number of key components involved in the process of fragility analysis, including monitoring, modeling, and hybrid simulation, to reduce the uncertainties in the result. More specifically, in the developed approach, monitoring with wireless smart sensor networks facilitates efficient and accurate pre- and post-disaster data collection, new modeling techniques including innovative system identification and model updating enables accurate structural modeling, hybrid simulation as an advanced numerical-experimental simulation tool generates highly realistic and accurate structural response data under earthquakes, and Bayesian-based approach improves the analytical fragility function by incorporating hybrid simulation data. Finally, a broad framework was developed for reliable seismic risk assessment which includes both the fragility analysis and the hazard characterization components.

An extensive review on the current status of structural health monitoring, system identification, hybrid simulation, and fragility analysis identified the gaps of knowledge in each area. Structural health monitoring provides essential data to characterize the behavior of structures. Wireless smart sensor networks facilitate efficient data collection, which is especially important for pre- and post-earthquake structural assessment. However, the efficiency of data collection and the quality of collected data in terms of time synchronization need to be improved. With data collected, the key structural characteristics can be extracted from the data through system identification. Identification of civil structures under earthquake loading is challenging, not only because earthquake excitations and the induced structural responses are transient signals with short duration, but also the input-output relationship is often complicated due to the intrinsically three-dimensional input and the complexity of civil engineering structures. Hybrid simulation provides an effective and efficient experimental way of examining the structural response under earthquake loading. However, the effort in exploring the hybrid simulation method considering MSE has been limited. Such investigation is important if fragility functions are to be generated for structures under MSE. The derivation of fragility functions has been extensively studied in the past; however, large uncertainties still exist, mainly due to the limited collaboration between the interdependent components involved in the course of fragility estimation. Bayesian updating provides a systematic way of improving existing fragility estimation incorporating new data, such as data from hybrid simulation. The effectiveness of improving fragility estimation by incorporating a few data points from hybrid simulation through Bayesian updating has not been investigated. The literature review defined a clear roadmap for the subsequent research topics explored in this report.

To improve the efficiency of data collection using WSSNs and the quality of collected data, a new post-sensing time synchronization approach was proposed. In the new approach, the gateway node broadcasts beacon messages during sensing, therefore the delay imposed on the previous approach is removed and the nonlinear clock drift during long-term data collection can be accurately captured and compensated. To account for potential conflict between the sample acquisition and RF communication, outlier detection method based on Cook's distance has been implemented to detect and remove outliers before clock drift estimation. Test results showed that the new approach was able to achieve higher accuracy of time synchronization in long-term data collection when nonlinearity in clock drift became significant. In addition to the time

synchronization method, a single-sink multi-hop (SSMH) data transfer method has been integrated into the ISHMP Service Toolsuite. Flooding-based remote command has been implemented to initiate the SSMH process. Also, new flooding-based commands have also been developed to efficiently wakeup and reset the network before and after the data transfer.

To address the challenge of system identification with highly coupled seismic response signals, a new strategy of MIMO system identification based on decoupling was proposed. The idea is to simplify the MIMO problems by converting them into a number of SIMO ones, which are computationally less complex and hence can potentially yield more accurate result. A QR decomposition-based method was introduced to extract the contribution of a specific input to a desired output, so as to decouple the system. Three factors, including the memory length, the input correlation, the system damping, have been investigated to assess the accuracy of the decoupling method. For civil engineering structures subjected to multi-directional earthquake inputs, if the angle between the inputs is larger than 80 degrees, the decoupling method can generally produce satisfactory result. In addition to the decoupling strategy, an automatic system identification method combining the ARX and ERA methods has been proposed. The method takes the advantage of the great performance of the ARX method in dealing with the transient and short duration seismic records. Meanwhile, it utilizes the noise mode indicators, including the EMAC and MPC, to delineate the structural and noise modes in the fitted ARX model. The decoupling strategy and the ARX-ERA method were applied to identify the modal parameters of the MRO Bridge subjected to earthquake loadings. The decoupling method was capable of removing the contribution from the lateral input to the vertical output, hence was able to convert the MIMO problem into SIMO problems in the vertical direction. The ARX-ERA method effectively identified three modes based on the decoupled signals.

Bayesian updating of fragility functions using hybrid simulation data has been investigated. The median ground motion intensity and the dispersion were treated as random variables and were described as prior distributions. The corresponding values from the initial fragility functions were used to construct these distributions. The hybrid simulation results were used to build the likelihood function. MCMC was adopted to estimate the updated parameters of the fragility functions by taking samples from the posterior distributions. In order to validate the effectiveness of the Bayesian updating approach with a few hybrid simulation data, comparison was made to fragility functions of the MRO Bridge generated in four different ways, which represents an increasing level of data availability. The ones with highest fidelity were generated with structural model calibrated using cyclic testing data and measured seismic data, and the analytical fragility functions were then further updated using hybrid simulation experiments, whereas in other cases, only partial data or no data was used in fragility analysis. The comparison showed that the Bayesian updating strategy with a few hybrid simulation data was able to achieve high accuracy in the updated fragility functions even though the initial estimates were far from the baseline. This strategy provides a systematic way of maintaining the database of seismic risk assessment systems and allows improvement of the fidelity of the fragility function in a consistent way as more and more data becomes available.

Hybrid simulation method considering MSE was then studied in this report. Emphasis has been placed on the evaluation of accuracy for the solution of equations of motion in relative coordinates (EOM-rel approximation), which has been widely used in conventional time-history analysis of MSE problems but has not been attempted to hybrid simulation. The evaluation was conducted first by employing both the EOM-rel approximation and EOM-abs formulation to determine the response of a single degree of freedom (SDOF) nonlinear oscillator with two

ground inputs; subsequent evaluation was conducted for hybrid simulation of a four-span highway ramp bridge. Implementation of the two formulations in hybrid simulation with MSE has been proposed to enable this comparison. In the first evaluation, significant error was found in EOM-rel approximation when linear stiffness matrices were used in the influence matrix, as only the two nonlinear columns were contributing to the stiffness matrices. For the four-span Highway Bridge, significant errors were also found when using the EOM-rel approximation. A parametric study showed that the errors are reduced by increasing the stiffness of the deck, implying that the EOM-rel approximation can provide results with good accuracy in the case that the change of stiffness in the experimental substructure does not affect significantly the overall stiffness matrix. Conversely, the error in the EOM-rel approximation can be significant if the change in the stiffness of the experimental substructure plays a major role in the global stiffness of the structure. In such cases, the EOM-abs is recommended to be used in hybrid simulation with MSE.

Taking advantage of the integrated high-fidelity fragility analysis approach, a comprehensive framework for seismic risk assessment has been developed. Besides the fragility analysis component, this framework also incorporates a seismic hazard analysis component, providing high-fidelity analysis for hazard characterization. The key idea is to provide an extensible and scalable platform for reliable seismic risk assessment. Therefore, GUIs have been developed for each component to facilitate ease of use, such as seismic hazard characterization, synthetic ground motion generation, finite element modeling, system identification and model updating, hybrid simulation, and seismic impact assessment. The modular design of each component allows new methodologies and algorithms to be added to the framework, providing extensibility. A seismic assessment of a building structure has demonstrated the functionality of each component. The final result has verified that the fragility functions estimated using the integrated approach developed in this report is more realistic than the default ones provided by MAEviz.

This research has demonstrated the effectiveness of the idea of improving the fidelity of fragility estimation by integrating the key areas involved in the estimation process. It has also illustrated that while research on each individual area by improving the methodologies and algorithms is important for advancing the knowledge at low levels, bringing together the advancements in these individual areas and emphasizing their interdependence and the interaction among them is also critical for achieving higher-level improvement which has direct impact on society, such as seismic risk assessment to support for both pre- and post-disaster decision-making. This research has not only delivered an extensible and scalable framework for high-fidelity fragility analysis and reliable seismic risk assessment, but also provided advances in wireless smart sensor networks, system identification, and pseudo-dynamic testing in civil engineering applications.

8.2 Future Studies

This report has explored a number of critical research areas involved in the process of estimating high-fidelity fragility functions. A few challenges have been addressed with the developed new algorithms and strategies. Meanwhile, a number of future research directions have been identified based upon some of the remained challenges and the limitations of current methods. These future research directions are detailed below.

8.2.1 Wireless Smart Sensor Networks

Structural health monitoring using WSSNs sometimes requires more than one network when spatially distributed structures, such as long-span bridges, are to be monitored due to the limited radio communication range of wireless smart sensors. The post-sensing time synchronization approach showed great performance in synchronizing sensor nodes within one network. However, challenges still exist in synchronization of sensor nodes in multiple networks. One possible solution is to use low cost Global Positioning System (GPS). GPS devices generate standard Pulse Per Second (PPS) timing signals which has nanosecond-level precision. To synchronize multiple sensor networks, the gateway node in each network is connected with one GPS and monitors the generated PPS signal. The timing of each step in post-sensing time synchronization, such as sending the initial beacon signal before sensing, calculation of the sensing start time, sending the first beacon signal during sensing, etc., can be precisely controlled by the PPS signal through hardware interrupt. Such precise control of timing based on a common time frame, i.e. the PPS signal, ensures synchronized activities among the separated sensor networks.

Another desired feature of WSSN-based SHM is the capability of running without a base station. In campaign-type monitoring, the sensor network may need to be deployed for a few days or weeks to collect enough data. However, civil infrastructures are often located in remote areas where power supply is not always available to support a base station. In such a case, the gateway node has to run independently without being connected to a base station. A unique scheme is therefore needed to manage the gateway node to allow continuous and autonomous operation over an extended period of time without draining the battery. The successful development of this feature will provide a powerful tool for a wide range of applications involving unattended short-term continuous and autonomous campaign monitoring of civil infrastructures.

8.2.2 System Identification

The system identification strategy based on decoupling needs further investigation for systems with larger number of inputs. This approach was shown to be able to address the challenges raised by multi-directional earthquake input. Therefore, the investigation of its performance was carried out using systems with only three inputs. However, for more complicated system identification problems, such as structures under Multiple-Support Excitation (MSE), the number of inputs can be much larger than three. One potential challenge is that the size of the matrix involved in the QR decomposition will increase dramatically if the number of inputs increases, hence the error may become more significant.

8.2.3 Hybrid Simulation

The proposed hybrid simulation method considering MSE needs to be verified experimentally. The comparison between the EOM-rel and EOM-abs can be further verified by conducting a series of experiments using the procedures detailed in Section 6.4.2.

The hybrid simulation studied in this report belongs to pseudo-dynamic testing, in which the target displacements are applied at slow speed. This feature allows detailed examination of the test specimens during experiments. It also lowers the requirement of the hydraulic actuators in terms of speed, and hence allows testing of large-scale structures in a cost-effective way. However, this type of hybrid simulation is not able to test structures with rate dependent

components, such as dampers, friction devices, and base isolation. To test these types of structures, Real-time hybrid simulation (RTHS) must be employed. In RTHS, testing is performed in a real-time manner. In a testing cycle, the computation, communication, and actuator movement are finished within the interval of time-stepping integration (usually less than 10 ms). Time delay and time lag compensation has been the research focus for RTHS in the past. Many challenges also exist in RTHS when multiple actuators and multi-dimensional problems are considered.

8.2.4 Bayesian Updating of Fragility Functions

The strategy of improving fragility function estimation by incorporating a few hybrid simulation data has been shown effective. However, there are some details in the procedure which can be improved in the future. For example, the point estimation of the updated parameters was done by Markov Chain Monte Carlo (MCMC) sampling, which lacks efficiency in terms of computation. Other sampling techniques, such as the importance sampling, can be explored. Moreover, the likelihood function was shown to play an important role in the Bayesian updating process. In current formulation of likelihood function, every hybrid simulation data point was treated as a realization of a Bernoulli experiment, hence the measured response was converted to a binary number before being included in the likelihood function. However, in fact, information was lost during the conversion. In other words, the current formulation of likelihood function does not fully utilize the experimental information from hybrid simulation. Other types of likelihood function should be investigated.

REFERENCES

Adler, R., Flanigan, M., Huang, J., Kling, R., Kushalnagar, N., Nachman, L., et al. (2005). "Intel mote 2: An advanced platform for demanding sensor network applications." *Proc. of the 3rd International Conference on Embedded Networked Sensor Systems*, 298-298.

AISC (2005). "Specification for structural steel buildings." ANSI/AISC 360-05, *American Institute of Steel Construction, Inc.*, Chicago.

Allemang, R. J., Brown, D. L. (1982). "A correlation coefficient for modal vector analysis," *Proceedings of the International Modal Analysis Conference*, Orlando, Florida, 110~116.

Alves, S. W. and Hall, J. F. (2006). "System identification of a concrete arch dam and calibration of its finite element model." *Earthquake Engineering and Structural Dynamics*, 35:1321-1337.

Anderson, D. G. (2003). Laboratory Testing of Nonlinear Soil Properties: I & II. prepared by CH2M HILL, Bellevue, Washington for the Lifeline Research Program, Pacific Earthquake Engineering Research Center, University of California at Berkeley, December.

Anderson, P., Basseville, M., Brincker, R., Mevel, L., Ventura, C. E., and Zhou, W. (2007). "Seismic damage assessment in structural using stochastic subspace-based algorithm." *ECCOMAS Thematic Conference on Computational Methods in Structural Dynamics and Earthquake Engineering*, Rethymno, Grete, Greece, 13-16 June.

Anderson, J. C., Bertero, V. V. (1991). "Seismic performance of an instrumented six-story steel building." *Report UCB/EERC-91/11*, University of California, Berkeley, U.S.A.

Ang, A. H. and Tang, W.H. (1975). Probability Concepts in Engineering Planning and Design. Vol.I. Basic Principles, John Wiley & Sons, New York.

ANSS (2005). Guidelines for ANSS Seismic Monitoring of Engineered Civil Systems. *U.S.Geological Survey, USGS Open-File 2005-1039*.

Antonacci,E., Ceci, A. M., Colarieti A., Gattulli, V., Graziosi, F., Lepidi, M. and Potenza, F. (2011). "Dynamic testing and health monitoring via wireless sensor networks in the post-earthquake assessment of structural conditions at L'Aquila." *Proceedings of the 8th International Conference on Structural Dynamics*, EURODYN 2011, Leuven, Belgium, 4-6 July 2011.

Aoki, S., Fujino, Y., and Abe, M. (2003). "Intelligent Bridge Maintenance System using MEMS and network technology." *Proceedings of SPIE – Smart Systems and NDE for Civil Infrastructures*, 5057, 37-42.

Arici, Y. and Mosalam, K. M. (2003). "System identification of instrumented bridge systems." *Earthquake Engineering and Structural Dynamics*, 32:999-1020.

Applied Technology Council (1996). "Seismic Evaluation and Retrofit of Concrete Buildings," Report ATC-40, Applied Technology Council, Redwood City, California.

Applied Technology Council (2001). "Database on the performance of structures near strong-motion recordings: 1994 Northridge, California, earthquake." *Report No. ATC-38*, Redwood City, CA.

Aviram, A., Mackie, K. R. and Stojadinovic, B. (2008). "Guidelines for Nonlinear Analysis of Bridge Structures in California," Technical Report 2008/03, Pacific Earthquake Engineering Research Center, University of California, Berkeley.

Ayyub, B. M., and Lai, K. (1989). "Structural Reliability Assessment Using Latin Hypercube Sampling." *Proceedings of ICOSSAR'89, the 5th International Conference on Structural Safety and Reliability*, Part II, ASCE, New York, NY, USA, 1177-1184.

Baber, T.T. and Wen, Y.K. (1981). "Random vibration of degrading pinching systemshysteretic, degrading systems." *Journal of Engineering Mechanics Division*, Vol. 107, No. 6, 1069-1087.

Basheer, M. R., Rao, V., and Derriso, M. (2003). "Self-organizing Wireless Sensor Networks for Structural Health Monitoring." *Proceedings of the 4th International Workshop on Structural Health Monitoring*, Stanford, CA, September 15-17, 1193-1206.

Bathe, K.J., Wilson, E.L. (1973). "Stability and accuracy analysis of direct integration methods." *Earthquake Engineering and Structural Dynamics.* Vol. 1, 283-291.

Beck, J. L. and Jennings, P. C. (1980). "Structural identification using linear models and earthquake records." *Earthquake Engineering and Structural Dynamics*, Vol. 8, 145-160.

Bendat, J. S. and Piersol, A. G. (1993). Engineering applications of correlation and spectral analysis, Wiley, New York.

Bennett, R., Hayes-Gill, B., Crowe, J. A., Armitage, R., Rodgers, D., and Hendroff, A. (1999). "Wireless Monitoring of Highways," *Proceedings of the SPIE - Smart Systems for Bridges, Structures, and Highways*, Newport Beach, CA, March 1-2, , vol. 3671, 173-182.

Bentz, E. C., (2000). "Sectional Analysis of Reinforced Concrete Members," Ph.D. Thesis, Department of Civil Engineering, University of Toronto.

Bowman, A. W., and Azzalini, A. (1997). Applied Smoothing Techniques for Data Analysis. New York: Oxford University Press.

Brincker, R., Zhang, L. and Anderson, P. (2001). "Model identification of output-only systems using frequency domain decomposition." Smart Materials and Structures, 10, 441-445.

Broderick, B.M., and Elnashai, A.S. (1995). "Analysis of the failure of Interstate 10 freeway ramp during the Northridge earthquake of 17 January 1994." *Earthquake Engineering and Structural Dynamics*, Vol. 24, 189-208.

Brownjohn, J. M. W. (2007). "Structural health monitoring of civil infrastructure." *Phil. Trans. R. Soc. A* 365, 589–622.

Brownjohn, J. M. W., Moyo, P., Omenzetter, P. & Lu, Y. (2003). "Assessment of highway bridge upgrading by dynamic testing and finite element model updating." *ASCE J. Bridge Eng.* 8: 162–172.

Brownjohn, J. M. W., Bocciolone, M., Curami, A., Falco, M. and Zasso A. (1994). "Humber Bridge full-scale measurement campaigns." *Journal of Wind Engineering and Industrial Aerodynamics*, 52:185-218.

Campbell, K. W. and Bozorgnia, Y. (2008). "NGA Ground Motion Model for the Geometric Mean Horizontal Component of PGA, PGV, PGD and 5% Damped Linear Elastic Response Spectra for Periods Ranging from 0.01 to 10 s," *Earthquake Spectra*, 24(1): 139-172.

Carrion, J. E., Spencer Jr., B. F., and Phillips, B. M. (2009). "Real-time hybrid simulation for structural control performance assessment." *Earthquake Engineering and Engineering Vibration*, 8:481-492.

Casciati, F. and Magonette, G. (1999). "Testing facilities and laboratory validation." *Advances in Structural Control* (ed. J. Rodellar, A. H. Barbat and F. Casciati), pp. 1-23. Barcelona: CINME.

Çelebi, M. (2004). "Structural Monitoring Arrays – Past, Present, and Future." *Proc. NATO Workshop on Future Directions on Strong Motion and Engineering Seismology*, Kuşadasi, Izmir, Turkey, May 17-21, 2004.

Çelebi, M. (2006). "Real-Time Seismic Monitoring of the New Cape Girardeau Bridge and Preliminary Analyses of Recorded Data: An Overview." *Earthquake Spectra*, 22:609-630.

Chaudhary, M. T. A., Abe, M., Fujino, Y., and Yoshida, J. (2000). "System identification of two base-isolated bridges using seismic records." *Journal of Structural Engineering*, 126(10): 1187-1195.

Chen, S, Billings, S. A., and Luo, W. (1989). "Orthogonal least squares methods and their application to non-linear system identification." Int. J. Control, 50 (5), 1873-1896.

Chen, S, Cowan, C. F. N, and Grant, P. M. (1991). "Orthogonal least squares learning algorithm for radical basis function networks." IEEE Transaction on Neural Networks, 2(2), 302-309.

Choe, D., Gardoni, P. and Rosowsky, D. (2007). "Closed-Form Fragility Estimates, Parameter Sensitivity, and Bayesian Updating for RC Columns," Journal of Engineering Mechanics, 133(7): 833-843.

Chopra, A. K. (2001). *Dynamics of structures: Theory and applications to earthquake engineering*, 2nd Ed., Prentice Hall, Upper Saddle River, N.J.

Clough, R.W and Penzien, J., (1975), *Dynamics of Structures*, Mc Graw-Hill, New York, 534 pp.

Combescure, D. and Pegon, P. (1997). "α-Operator Splitting time integration technique for pseudodynamic testing error propagation analysis." *Soil Dynamics and Earthquake Engineering*, 16, 427-443.

Cornell, A. C., Jalayer, F., and Hamburger, R. O. (2002). "Probabilistic Basis for 2000 SAC Federal Emergency Management Agency Steel Moment Frame Guidelines." *Journal of Structural Engineering*, 128(4), 526–532.

Cook, R. Dennis, (1977). "Detection of Influential Observations in Linear Regression". *Technometrics*, 19 (1): 15–18.

Craig, R.R., Jr. and Kurdila A.J., (2006), Fundamentals of Structural Dynamics, 2nd Ed., John Wiley & Son, Inc., Hoboken, New Jersey, 728pp.

Crossbow Technology, Inc, "MICA2 Wireless Measurement System," San Jose, CA (2007).

Crouse, C. B. and Price, T. (1993). "Dynamic Soil-foundation Interaction at the Meloland Road Overcrossing." Proc. ASCE Structural Engineering in Natural Hazards Mitigation, Irvine, Calif., Vol. 1, 355-360.

Daniell, J. and Vervaeck, A. (2012). "Damaging Earthquakes Database 2011 – The Year in Review." *CEDIM Earthquake Loss Estimation Series, Research Report No. 2012-01*, CEDIM, Karlsruhe, Germany.

Darby, A. P., Blakeborough, A. and Williams, M. S. (2000). "Real-time substructure tests using hydraulic actuator." *Journal of Engineering Mechanics*, 125, 1133-1139.

Der Kiureghian, A. (1999a). "Fragility estimates for electrical substation equipment," Proc. 5th U.S. Conference on Lifeline Earthquake Engineering, August 1999, Seattle, WA, W. Elliott and P. McDonough, Eds, 643-652.

Der Kiureghian, A. (1999b). "A Bayesian framework for fragility assessment," Proc. 8th Int. Conf. On Applications of Statistics and Probability (ICASP) in Civil Engineering Reliability and Risk Analysis, Sydney, Australia, December 1999, R.E. Melchers and M. G. Stewart, Eds., 1, 219-226.

Der Kiureghian, A. (2002). "Bayesian methods for seismic fragility assessment of lifeline components," In Acceptable Risk Processes: Lifelines and Natural Hazards, ASCE Council on Disaster Reduction and Technical Council on Lifeline Earthquake Engineering Monograph N0. 21, C. Taylor and E. VanMarcke, Editors, March 2002, 61-77.

Draper, N. R. and Smith, H. (1998). Applied Regression Analysis (Third Edition). Wiley, New York.

Dutta, A. (1999). "On Energy Based Seismic Analysis and Design of Highway Bridges," PhD thesis, State University of New York at Buffalo.

Elnashai, A. S. (2003). "Next generation vulnerability functions for RC structures," *Proceeding of Response of Structures to Extreme Loading*, Toronto, Canada, August 2003.

Elnashai, A.S., Spencer, B.F., Kuchma, D., Ghaboussi, J., Hashash, Y. and Quan, G. (2004). "Multi-Axial Full-Scale Sub-Structured Testing and Simulation (MUST-SIM) Facility at the University of Illinois at Urbana-Champaign," *Proceedings of the 13th World Conference on Earthquake Engineering*, Vancouver, Canada, August 2004.

Elnashai, A. S., Papanikolaou V., and Lee, D. (2004). Zeus NL – a system for inelastic analysis of structures, Mid-America Earthquake Center, University of Illinois at Urbana-Champaign, Program Release January 2004.

Elson, J. E., Girod, L., and Estrin, D. (2002). "Fine-Grained Network Time Synchronization using Reference Broadcasts." The fifth symposium on operating system design and implementation (OSDI), p. 147-163.

Farrar, C. R. (2001). "Historical Overview of Structural Health Monitoring." *Lecture Notes on Structural Health Monitoring Using Statistical Pattern Recognition*, Los Alamos Dynamics, Los Alamos, NM.

Farrar C. R. and Worden, K. (2007). "An introduction to structural health monitoring." *Phil. Trans. R. Soc.* A 365: 303-315. (doi:10.1098/rsta.2006.1928)

Felber, A. J. (1993). Development of a hybrid bridge evaluation system. Ph.D. thesis, Department of Civil Engineering, University of British Columbia, Vancouver, Canada.

FEMA (2000). Recommended Seismic Design Criteria for New Steel Moment-Frame Buildings, Report No. FEMA-350, Washington D.C.

FEMA (2008). HAZUS-*MH Estimated Annualized Earthquake Losses for the United States*, Report No. FEMA-366, Washington, D.C.

Frankel, A. D. and Leyendecker, E. V. (2001). "Seismic Hazard Curves and Uniform Hazard Response Spectra for the United States," Open-File Report 01-436, U.S. Geological Survey: Menlo Park, CA.

Fumal, T. E., Gibbs, J. F., and Roth, E. F. (1979). "In-situ measurements of seismic velocity at 19 locations in the Los Angeles, California region" *SMIP geotechnical report No. 131*, U.S. Geological Survey.

Ganeriwal, S, Kumar, R., and Srivastava, M. B. (2003). "Time-Syn Protocol for Sensor Networks." The first ACM conference on embedded networked sensor system (SenSys), P. 138-149.

Gardoni, P., Der Kiureghian, A. and Mosalam, K. M. (2002). "Probabilistic Capacity Models and Fragility Estimates for Reinforced Concrete Columns based on Experimental Observations," Journal of Engineering Mechanics, 128(10): 1024-1038.

Gardoni, P., Mosalam, K. M. and Der Kiureghian, A. D. (2003). "Probabilistic Seismic Demand Models and Fragility Estimates for RC Bridges," Journal of Earthquake Engineering, 7:S1, 79-106.

Gasparini, D. A. and Vanmarcke, E. H. (1976). "Simulated Earthquake Motions Compatible with Prescribed Response Spectra, Evaluation of Seismic Safety of Buildings," Report No.2, Massachusetts Institute of Technology.

Gay, D., Levis, P., von Behren, R., Welsh, M., Brewer, E. and Culler, D. (2003). "The nesC language: a holistic approach to networked embedded systems." *Proceedings of the ACM SUGPLAN Conference on Programming Language Design and Implementation, ser. PLDI'03*. New York, NY, USA: ACM, 2003, pp. 1-11.

Giles, R. K., Kim, R., Spencer Jr., B. F., Bergman, L. A., Shield, C. K. and Sweeney, S. C. (2011). "Structural Health Indices for Steel Truss Bridges," *T. Proulx (ed.), Civil Engineering Topics, Volume 4, Conference Proceedings of the Society for Experimental Mechanics Series*, 7, 391-398.

Hao, H and Duan, X. (1996). "Multiple excitation effect on response of symmetric buildings." *Engineering Structures*, 18(9), 732-740.

Hashash, Y., Groholski, D.R., Phillips, C.A., Park, D. (2009). DEEPSOIL V3.5beta, User Manual and Tutorial.

Hibbit, H. D., Karlsson, B. I., and Sorensen (2001). *ABAQUS theory manual. Version 6.2.*

Holub, C. J. (2009). "Interaction of Variable Axial Load and Shear Effects in RC Bridges," Ph.D. Thesis, University of Illinois at Urbana-Champaign, Urbana, Illinois.

Huang, Q., Gardoni, P. and Hurlebaus, S. (2010). "Probabilistic Seismic Demand Models and Fragility Estimates for Reinforced Concrete Highway Bridge with One Single-Column Bent," Journal of Engineering Mechanics, 136(11): 1340-1353.

Huang, C. S. and Lin, H. L. (2001). "Modal identification of structures from ambient vibration, free vibration, and seismic response data via a subspace approach." *Earthquake Engineering and Structural Dynamics*, 30:1857-1878.

Huang, M. J., Shakal, A. F. (2001). "Structure instrumentation in the California Strong Motion Instrumentation Program." *Strong Motion Instrumentation for Civil Engineering Structures, NATO ASI Series*, vol 373: 17-31

Hwang, H., Liu, J. B., and Chiu, Y.-H. (2000). "Seismic Fragility Analysis of Highway Bridges." *Report No. MAEC RR-4*, Center for Earthquake Research Information.

Iwan, W. D. (2008). *"Some Milestones In Strong Motion Monitoring (Abstract)." SMIP08 Seminar on Utilization of Strong-Motion Data*, p. 57 - 58.

Izuddin, B.A., Karayannis, C.G., and Elnashai, A.S. (1994). "Advanced nonlinear formulation for reinforced concrete beam-columns," Journal of Structural Engineering, 120(10): 2913-2934.

Jang, S., Li, J. and Spencer Jr., B. F. (2012). "Corrosion Estimation of a Historic Truss Bridge using Model Updating." *ASCE Journal of Bridge Engineering*. (In press)

Jernigan, J. B. and Hwang, H. (2002). "Development of Bridge Fragility Curves." *7th US National Conference on Earthquake Engineering*, Boston, Mass.

Ji, X., Fenves, G. L., Kajiwara, K., and Nakashima, M. (2011). "Seismic damage detection of a full-scale shaking table test structure." Journal of Structural Engineering, 137(1), 14-21.

Jo, H., Park, J. W., Spencer Jr., B. F., and Jung, H. J. (2012). "Design and validation of high-precision wireless strain sensors for structural health monitoring of steel structures." *Proc. SPIE 8345*, 834518 (2012), DOI:10.1117/12.915392

Jo, H., Rice, J. A., and Spencer Jr., B. F. (2010). "Development of high-sensitivity accelerometer board for structural health monitoring." *Proc. SPIE 7647*, 764706 (2010), DOI:10.1117/12.848905

Jo, H., Sim, S. H., Mechitov, K.A., Kim, R., Li, J., Moinzadeh, P., Spencer Jr, B. F. et al. (2011). "Hybrid wireless smart sensor network for full-scale structural health monitoring of a cable-stayed bridge." *Proc. SPIE 7981*, 798105 (2011), DOI:10.1117/12.880513

Johnson, D. B., Maltz, D. A., and Hu, Y. C. (2007). *The dynamic source routing protocol for mobile ad hoc networks (DSR)*, Technical Report, IETF MANET Working Group.

Juang, J. N. and Pappa, R. S. (1985). "An Eigensystem Realization Algorithm for Modal Parameter Identification and Modal Reduction." *Journal of Guidance Control and Dynamics*, 8(5):620-627.

Kempton, J. J. and Stewart, J. P. (2006). "Prediction Equations for Significant Duration of Earthquake Ground Motions Considering Site and Near-Source Effects," *Earthquake Spectra*, 22(4): 985-1013.

Kim, S., Pakzad, S., Culler, D., Demmel, J., Fenves, G., Glaser, S., and Turon, M. (2007). "Health Monitoring of civil infrastructures using wireless sensor networks." *Proceedings of the 6th International Conference on Information Processing in Sensor Networks*, Cambridge, Massachusetts, USA, April.

Kling, R. M. (2003). "Intel mote: An enhanced sensor network node." *Proc. of the International Workshop on Advanced Sensors, Structural Health Monitoring, and Smart Structures*, Tokyo, Japan, Nov 10-11.

Kling, R., Adler, R., Huang, J., Hummel, V., and Nachman, L. (2005). "Intel mote-based sensor networks." *Structural Control and Health Monitoring*, 12, 469-479.

Kottapalli, V. A., Kiremidjian, A. S., Lynch, J. P., Carryer, E., Kenny, T. W., Law, K. H.,. and Lei, Y. (2003). "Two-tiered wireless sensor network architecture for structural health monitoring." *Smart Structures and Materials, San Diego, CA, March 3-6, Proceedings of the SPIE*, Vol. 5057, 8-19.

Koutsourelakis, P. S. (2010). "Assessing structural vulnerability against earthquakes using multi-dimensional fragility surfaces: A Bayesian framework," *Probability Engineering Mechanics*, 25: 49-60.

Kwon, O. and Elnashai, A. S. (2007). "Probabilistic Seismic Assessment of Structure, Foundation and Soil Interacting Systems," *NSEL Report Series*, Report No. NSEL-004, December 2007.

Kwon, O.S., Nakata, N., Elnashai, A., and Spencer Jr., B. F. (2005). "A Framework for Multi-site Distributed Simulation and Application to Complex Structural Systems," *Journal of Earthquake Engineering*, 9 (5):741–753.

Lee, D. H. and Elnashai, A. S. (2001). "Seismic Analysis of RC Bridge Columns with Flexure-Shear Interaction," Journal *of Structural Engineering, ASCE*, 127(5): 546-553.

Li, J., Lin, S. L., Zong, X., Spencer Jr., B. F., Elnashai, A. S., and Agrawal, A. K. (2009). "An integrated earthquake impact assessment framework." *ANCER Annual Meeting*, August 13-14, Urbana, Illinois.

Lin, S. L. (2010). An integrated earthquake impact assessment system. Ph.D. Thesis University of Illinois at Urbana-Champaign.

Lind, I. and Ljung, L. (2008). "Regressor and structure selection in NARX models using a structured ANOVA approach." Automaica, 44, 383-395.

Ljung, L. (1999). System identification: Theory for the user, 2nd edition, Prentice-Hall, Inc, Englewood Cliffs, NJ.

Loh, C.–H. and Lin, H.-M. (1996). "Application of off-line and on-line identification techniques to building seismic response data." *Earthquake Engineering and Structural Dynamics*, Vol. 25, 269-290.

Loh, C.–H. and Wu, T.-C. (2000). "System identification of Fei-Tsui arch dam from forced vibration and seismic response data." *Journal of Earthquake Engineering*, 4(4):511-537.

Lus, H., Betti, R. and Longman, R. W. (1999). "Identification of linear structural systems using earthquake-induced vibration data." *Earthquake Engineering and Structural Dynamics*, 28, 1449-1467.

Lynch, S. M. (2007). Introduction to Applied Bayesian Statistics and Estimation for Social Scientists, Springer, New York.

Lynch, J. P., Law, K. H., Kiremidjian, A. S., Kenny, T. W., Carryer, E., and Partridge, A. (2001). "The Design of a Wireless Sensing Unit for Structural Health Monitoring." *Proceedings of the 3rd International Workshop on Structural Health Monitoring*, Stanford, CA, September 12-14.

Lynch, J. P., Law, K. H., Kiremidjian, A. S., Kenny, T. W., and Carryer, E. (2002). "A Wireless Modular Monitoring System for Civil Structures." Proceedings of the 20th International Modal Analysis Conference (IMAC XX), Los Angeles, CA, February 4-7, 1-6.

Lynch, J. P. and Loh, K. J. (2006). "A Summary Review of Wireless Sensors and Sensor Networks for Structural Health Monitoring." *The Shock and Vibration Digest*, 38(2): 91-128.

MAEviz (2008). "MAEviz Software," Mid-America Earthquake Center, University of Illinois at Urbana-Champaign, Urbana, Illinois, "http://mae.cee.uiuc.edu/software_and_tools/maeviz.html" February 12.

Mahin, S. A. and Shing, P. B. (1985). "Pseudodynamic methods for seismic testing." *Journal of Structural Engineering*. 111, 1482-1503.

Mander, J. B. and Basoz, N. (1999). "Seismic Fragility Curve Theory for Highway Bridges." *5th US Conference on Lifeline Earthquake Engineering*, Seattle, WA, USA.

Mackie, K. and Stojadinovic, B. (2001). "Probabilistic Seismic Demand Model for California Bridges." *Journal of Bridge Engineering*, 6(6), 468–480.

Madas, P., Elnashai, A.S. (1992). "A new passive confinement model for the analysis of concrete structures subjected to cyclic and transient dynamic loading," Earthquake Engineering and Structural Dynamics, Vol. 21, 409-431.

Maroti, M., Kusy, B., Simon, G., and Ledeczi, A. (2004). "The flooding time synchronization protocol." Proceedings of 2nd International Conference on Embedded Networked Sensor Systems, Baltimore, MD, 39-49.

MATLAB User's Guide, (2009). Mathworks, Natick, MA.

McKenna, F. and Fenves, G. L. (2001). *The OpenSees command language manual, version 1.2.*, Pacific Earthquake Engineering Research Center, University of California at Berkeley.

Mechitov, K. A. (2011). A Service-oriented Architecture for Dynamic Macroprogramming of Sensor Networks. Ph.D. Thesis, University of Illinois at Urbana-Champaign.

MEMSIC, Inc. (2010). "ISM400, Imote2 Structural Health Monitoring Board", Andover, MA.

Miller, A. (1990). Subset Selection in Regression. London: Chapman and Hall.

Mills, D. L. (1991). "Internet Time Synchronization: The Network Time Protocol." *IEEE Transactions on Communications* COM 39 No. 10, 1482-1493.

Mosalam, K.M., Ayala, G., White, R.N., and Roth, C. (1997). "Seismic Fragility of LRC Frames with and without Masonry Infill Walls," *Journal of Earthquake Engineering*, 1(4):693-720.

Mosqueda, G., Stojadinovic, B., and Mahin, S. (2004). "Geographically distributed continuous hybrid simulation*." Proceedings of the 13th world conference on Earthquake Engineering, Vancouver, Canada*, Paper No. 0959.

Nagayama, T., Moinzadeh, P., Mechitov, K., Ushita, M., Makihata, N., Ieiri, M., Agha, G., Spencer Jr., B. F., Fujino, Y., and Seo, J.-W. (2010). "Reliable multi-hop communication for structural health monitoring." *Smart Structures and Systems*, 6(5):481-504.

Nagayama, T., Ruiz-Sandoval, M., Spencer Jr., B. F., Mechitov, K. and Agha, G. (2004). "Wireless Strain Sensor Development for Civil Infrastructure." *First International Workshop on Networked Sensing Systems (INSS)*, pp 97-100.

Nagayama, T. and Spencer Jr., B. F. (2007). "Structural Health Monitoring using Smart Sensors." *NSEL Report Series,* No. 1, University of Illinois at Urbana-Champaign. http://hdl.handle.net/2142/3521.

Nagayama, T., Spencer Jr., B. F., Mechitov, K. A., and Agha, G. (2008). "Middleware services for structural health monitoring using smart sensors." *Smart Structures and Systems*, 6(5): 481-504.

Nakashima, M., Kaminisono, T., Ishida, M., and Ando, K. (1990). "Integration technique for substructure pseudodynamic test." *Proc. 4th Natl. Conf. on Earthquake Engineering*, Palm Springs, pp. 515-524.

Nakashima, M., Kato, H., and Takaoka, E. (1992). "Development of real-time pseudo dynamic testing." *Earthquake Engineering and Structural Dynamics*, 21, 79-92.

Nazmy, A. S., Abdel-Ghaffar, A. M. (1990). "Non-linear earthquake-response analysis of long-span cable-stayed bridges: applications." *Earthquake eng. struct. dyn.* 19, 63-76.

Newmark, N.M. (1959). "A method of computation for structural dynamics." *Proc. Am. Soc.Civ. Engs, 85,* EM3, 67-94.

Ni, Y. Q. (2010). "Structural Health Monitoring for Civil Infrastructure Systems: From Research to Application." *Proceedings of the Fifth European Workshop on Structural Health Monitoring*, Naples, Italy, June 28 – July 4, 2010.

Nielson, B.G. (2005). "Analytical fragility curves for highway bridges in moderate seismic zones," Ph.D. Thesis. Georgia Institute of Technology, Atlanta, Georgia.

Nielson, B. G. and DesRoches, R. D. (2007). "Seismic Fragility Methodology for Highway Bridges Using a Component Level Approach," Earthquake Engineering and Structural Dynamics, 36:823-839

Overschee, P. V. and Moor, B. D. (1996). Subspace identification for linear systems – Theory, Implementation, Applications. Kluwer academic Publishers, ISBN 0-7923-9717-7.

Padgett, J. E., DesRoches, R., and Nilsson, E. (2010). "Regional Seismic Risk Assessment of Bridge Network in Charleston, South Carolina." Journal of Earthquake Engineering, 14:918-933.

Pan, Y. (2007). "Seismic Fragility and Risk Management of Highway Bridges in New York State," Ph.D. Thesis, the City University of New York, New York, NY.

Pan, Y., Agrawal, A.K. and Ghosn, M. (2007). "Seismic Fragility of Continuous Steel Highway Bridges in New York State," *Journal of Bridge Engineering, ASCE,* 12(6): 689-699.

Pappa, R. S. and Elliott, K. B. (1993). "Consistent-mode indicator for the eigensystem realization algorithm." *J. Guid. Control Dyn*., 16(5): 852-858.

Park, K. S., Kwon, O. S., Spencer, B. F., Elnashai, A. S., 2007, "Tutorial for Beta version of SimBuild, Pre- and Post-processor for UI-SimCor ," Department of Civil and Environmental Engineering, University of Illinois at Urbana-Champaign, Urbana, Illinois.

Park, V. D. and Corson, M. S. (1997). "A highly adaptive distributed routing algorithm for mobile ad hoc networks," *Proceedings IEEE INFOCOM '97, The Conference on Computer Communications, Sixteenth Annual Joint Conference of the IEEE computer and Communications Societies, Driving the Information Revolution*, Kobe, Japan, April.

Pegon, P. and Pinto, A. V. (2000). "Pseudo-dynamic testing with substructuring at the ELSA laboratory." *Earthquake Engineering and Structural Dynamics*. 29:905-925.

Perkins, C. E. and Royer, E. M. (1999). "Ad-hoc on-demand distance vector routing," *Proceedings of the second IEEE workshop on mobile computing systems and applications*, February.

Pinto, A. V., Pegon, P, Magonette, G., and Tsionis, G. (2004). "Pseudo-dynamic testing of bridges using non-linear substructuring." *Earthquake Engineering and Structural Dynamics*, 33:1125-1146.

Pollard, D. (2005). *Handbook of Aeronautical Inspection and Pre-Purchase*. Trafford Publishing, Bloomington, IN, United States of America. P. 256.

Rice, J. A., Mechitov, K., Sim, S. H., Nagayama, T., Jang, S., Kim, R., Spencer Jr., B. F., Agha, G. and Fujino, Y. (2010). "Flexible Smart Sensor Framework for Autonomous Structural Health Monitoring," *Smart Stuct. Syst*. 6, 423-38.

Rice, J. A. and Spencer Jr., B. F. (2009). "Structural Health Monitoring Sensor Development for the Imote2 Platform." *Proceedings of Sensors and Smart Structures Technologies for Civil, Mechanical, and Aerospace Systems (SPIE 6932)*, San Diego, CA, USA.

Rice, J. A. and Spencer Jr., B. F. (2009). "Flexible Smart Sensor Framework for Autonomous Full-scale Structural Health Monitoring." *NSEL Report Series*, No. 18, University of Illinois at Urbana-Champaign. http://hdl.handle.net/2142/13635.

Robert, C. P. (2007). The Bayesian Choice: From Decision-Theoretic Foundations to Computational Implementation (2nd Edition). Springer, New York.

Robert, N. (2007). "The Intersection of Earthquake Structural Response Monitoring and Structural Health Monitoring (Abstract)." *SMIP07 Seminar on Utilization of Strong-Motion Data*, p. 115 - 116.

Rojahn, C. and Sharpe, R. L. (1985). "ATC-13, Earthquake Damage Evaluation Data for California," Applied Technology Council, California.

Rossetto, T., Elnashai, A. (2003). "Derivation of vulnerability functions for European-type RC structures based on observational data," *Engineering Structures*, 25: 1241-1263.

Rossetto, T. and Elnashai, A. (2004). "A New Analytical Procedure for the Derivation of Displacement-Based Vulnerability Curves for Populations of Structures." *13th World Conference on Eartquake Engineering*, Vancouver, B.C. Canada.

Saadeghvaziri, M.A. and Foutch, D. A. (1991). "Dynamic Behaviour of R/C Highway Bridges Under the Combined Effect of Vertical and Horizontal Earthquake Motions." Earthquake Engineering and Structural Dynamics, Vol. 20, 535-549.

Saito, T. and Beck, J. (2010), "Bayesian model selection for ARX models and its application to structural health monitoring." Earthquake Engineering and Structural Dynamics, 39:1737-1759.

Shah, H. C., Mortgat, C. P., Kiremidjian, A. S. and Zsutty, T. C. (1975). "A Study of Seismic Risk for Nicaragua, Part I," Report No. 11, Department of Civil and Environmental Engineering, Stanford University.

Shing P. B. (2008). "Real-Time Hybrid Testing Techniques." in *Modern Testing Techniques for Structural Systems Dynamics and Control* , Edited by O. S. Bursi and D. J. Wagg, CISM-Springer Wien New York.

Shing, P. B. and Mahin, S. A. (1985). "Computational aspects of a seismic performance test method using on-line computer control." *Earthquake Engineering and Structural Dynamics*, 13(4):507-526.

Shing, B. and Manivannan, T. (1990). "On the accuracy of an implicit algorithm for pseudodynamic tests." *Earthquake Engineering and Structural Dynamics*, 119, 631-651.

Shing, B., Vannan, M. T., and Cater, E. (1991) "Implicit time integration for pseudodynamic tests." *Earthquake Engineering and Structural Dynamics*, 20, 551-576.

Shinozuka, M., Feng, M. Q., Lee, J. and Naganuma, T. (2000). "Statistical analysis of fragility curves," *Journal of Engineering Mechanics, ASCE*, 126(12):1224-1231.

Sim, S. H. and Spencer Jr., B. F. (2009). "Decentralized Strategies for Monitoring Structures using Wireless Smart Sensor Networks." *NSEL Report Series*, No. 19, University of Illinois at Urbana-Champaign.

Singhal A., Kiremidjian A. S. (1998). "Method for probabilistic evaluation of seismic structural damage," *Journal of Structural Engineering*, *ASCE*, 122(12): 1459-67.

Siringoringo, D. and Fujino, Y. (2006). "System identification applied to long-span cable-supported bridges using seismic records." *Earthquake Engineering and Structural Dynamics*. 37:361-386.

Smyth, A. W., Pei, J. S. and Masri, S. F. (2003). "System identification of the Vincent Thomas suspension bridge using earthquake records." *Earthquake Engineering and Structural Dynamics*. 32:339-367..

Straser, E. G. & Kiremidjian A. S. (1998). "A modular, wireless damage monitoring system for structures." *The John A. Blume Earthquake Engineering Center Technical Report*, *128*.

Spectral Dynamics, Inc. <http://www.spectraldynamics.com> (Feb. 2, 2012).

Spencer, B. F., Jr. (1986). ''On the reliability of nonlinear hysteretic structures subjected to broadband random excitation.'' *Lecture notes in engineering*, C. A. Brebbia and S. A. Orszag, eds., 21, Springer, New York.

Spencer Jr., B. F. et al. (2004). The MOST experiment: earthquake engineering on the grid. *Technical Report NEESgrid-2004-41*.

Spencer Jr., B. F., Elnashai, A., Kuchma, D., Kim, S., Holub, C. and Nakata, N. (2006). "Multi-Site Soil-Structure-Foundation Interaction Test (MISST)." University of Illinois at Urbana-Champaign.

Spencer Jr., B. F., Nagayama, T., Rice, J. A., and Agha, G. A. (2007). "Smart sensing technology: a new paradigm for structural health monitoring." *Proc. 39th Joint Panel Meeting on Wind & Seismic Effects, UJNR,* Tsukuba, Japan.

Spencer Jr., B.F., Ruiz-Sandoval, M and Kurata, N. (2004), Smart Sensing Technology: Opportunities and Challenges, *Structural Control and Health Monitoring* 11, 349– 368.

Takanashi, K. and Nakashima, M. (1987). "Japanese activities on online testing." *Journal of Engineering Mechanics*. 113, 1014-1032.

Tsai, K.-C., Yeh, C.-C., Yang, Y.-S., Wang, K.-J., and Chen, P.-C. (2003). "Seismic hazard mitigation: internet-based hybrid testing framework and examples." *International Colloquium on Natural Hazard Mitigation: Methods and Applications*, France, May.

Uddin, M.B. and Castelluccia, C. (2010). "Toward clock skew based wireless sensor node services," *In ICST Wireless Internet Conference (WICON)'10*, 1–9.

U. S. Geological Survey (1999). *Requirement for an Advanced National Seismic System*, U. S. Geological Survey Circular 1188.

USGS (2012). "Earthquake Facts and Statistics." *http://neic.usgs.gov/neis/eqlists/eqstats.html*, Date Accessed: March 05, 2012.

Wagg, D., Neild, S. and Gawthrop, P. (2008). "Real-Time Testing With Dynamic Substructuring." in *Modern Testing Techniques for Structural Systems Dynamics and Control* , Edited by O. S. Bursi and D. J. Wagg, CISM-Springer Wien New York.

Wantanabe, E., Kitada, T., Kunitomo, S., and Nagata, K. (2001). "Parallel pseudodynamic seismic loading test on elevated bridge system through the internet." *The Eighth East Asian-Pacific Conference on Structural Engineering and Construction*, Singapore, December.

Wei, H. L., Billings, S. A., and Liu, J. (2004). "Term and variable selection for non-linear system identification." Int. J. Control, 77(1), 86-110.

Wen, Y. K. (1976). "Method for random vibration of hysteretic systems." *J. Eng. Mech. Div.,* 102(2), 249-263.

Werner, S.D., Beck, J.L., Katafygiotis, L., and Nisar, A. (1993). "Seismic Analysis of Meloland Road Overcrossing Using Calibrated Structural and Foundation Models." Proc. ASCE Structural Engineering in Natural Hazards Mitigation, Irvine, Calif., Vol. 1, 367-372.

Werner, S. D., Beck, J. L. and Levine, M. B. (1987). "Seismic response evaluation of Meloland Road Overpass using 1979 Imperial Valley earthquake records." Earthquake Engineering and Structural Dynamics, Vol. 15, 249-274.

Westwick, D. T., Pohlmeyer, E. A., Solla, S. A., Miller, L. E., and Perreault, E. J. (2006). "Identification of Multiple-Input Systems with Highly Coupled Inputs: Application to EMG Prediction from Multiple Intracortical Electrodes." Neural Computation, 18, 329-355.

Williams, M. S. and Blakeborough, A. (2001). "Laboratory testing of structures under dynamic loads : an introductory review." *Phil. Trans. R. Soc. Lond*. A 359, 1651-1669.

Wilson, J. C. and Tan, B. S. (1988). "Bridge Abutments: Assessing Their Influence on Earthquake Response of Meloland Road Overpass." Journal of Engineering Mechanics, 116(8), 1838-1856.

Wong, K. Y. (2004). "Instrumentation and health monitoring of cable-supported bridges." *Struct. Control Health Monit*. 11:91-124.

Wong, K. Y., and Ni, Y. Q. (2009). "Modular architecture of structural health monitoring system for cable-supported bridges." *Encyclopedia of structural health monitoring*, Vol. 5, C. Boller, F.-K. Chang, and Y. Fujino eds., Wiley, Chichester, UK, 2089–2105.

Wu, B., Wang, Q., Shing, P. B., and Ou, J. P. (2007). "Equivalent force control method for generalized real-time substructure testing with implicit integration." *Earthquake Engineering and Structural Dynamics*, 36(9):1127-1149.

Wyss, G. D., and Jorgensen, K. H. (1998). "A User's Guide to LHS: Sandia's Latin Hypercube Sampling Software." Risk Assessment and Systems Modeling Department, Sandia National Laboratories, Albuquerque, NM.

Xia, Y., Fujino, Y., Abe, M. and Murakoshi, J. (2005). "Short-term and long-term health monitoring experience of a short highway bridge: case study." *Bridge Structures*, 1(1): 43-53.

Yang, Z., Cai, L., Liu, Y., and Pan, J. (2012)."Environment-Aware Clock Skew Estimation and Synchronization for Wireless Sensor Networks," *IEEE Infocom*, Orlando, FL, USA, March.

Yang, J., Li, J. B., and Lin, G. (2006). "A simple approach to integration of acceleration data for dynamic soil–structure interaction analysis." *Soil dynamics and earthquake engineering* 26, 725-734.

Yu, O., Allen, D. L., and Drnevich, V. P. (1991). "Seismic Vulnerability Assessment of Bridges on Earthquake Priority Routes in Western Kentucky." *3rd US Conference on Lifeline Earthquake Engineering*, Los Angeles, CA, USA.

Zhang, J. and Makris, N. (2001). "Seismic Response Analysis of Highway Overcrossings Including Soil-Structure Interaction." *PEER Report* 2001/02.

Zhong, J., Gardoni, P., Rosowsky, D. and Haukaas, T. (2008). "Probabilistic Seismic Demand Models and Fragility Estimates for Reinforced Concrete Bridges with Two-Column Bents," Journal of Engineering Mechanics, 134(6): 495-504.

List of Recent NSEL Reports

No.	*Authors*	*Title*	*Date*
021	Linderman, L.E., Rice, J.A., Barot, S., Spencer, B.F., and Bernhard, J.T.	Characterization of Wireless Smart Sensor Performance	Feb. 2010
.			
022	Miller, T.I. and Spencer, B.F.	Solar Energy Harvesting and Software Enhancements for Autonomous Wireless Smart Sensor Networks	March 2010
023	Denavit, M.D. and Hajjar, J.F.	Nonlinear Seismic Analysis of Circular Concrete-Filled Steel Tube Members and Frames	March 2010
024	Spencer, B.F. and Yun, C.-B. (Eds.)	Wireless Sensor Advances and Applications for Civil Infrastructure Monitoring	June 2010
025	Eatherton, M.R.. and Hajjar, J.F.	Large-Scale Cyclic and Hybrid Simulation Testing and Development of a Controlled-Rocking Steel Building System with Replaceable Fuses	Sept. 2010
026	Hall, K., Eatherton, M.R., and Hajjar, J.F.	Nonlinear Behavior of Controlled Rocking Steel-Framed Building Systems with Replaceable Energy Dissipating Fuses	Oct. 2010
027	Yeo, D. and Jones, N.P.	Computational Study on 3-D Aerodynamic Characteristics of Flow around a Yawed, Inclined, Circular Cylinder	Mar. 2011
028	Phillips, B.M. and Spencer, B.F.	Model-Based Servo-Hydraulic Control for Real-Time Hybrid Simulation	June 2011
029	Linderman, L.E., Mechitov, K.A., and Spencer, B.F.	Real-Time Wireless Data Acquisition for Structural Health Monitoring and Control	June 2011
030	Chang, C.-M. and Spencer, B.F.	Multi-axial Active Isolation for Seismic Protection of Buildings	May 2012
031	Phillips, B.M. and Spencer, B.F.	Model-Based Framework for Real-Time Dynamic Structural Performance Evaluation	August 2012
032	Moreu, F. and LaFave, J.M.	Current Research Topics: Railroad Bridges and Structural Engineering	October 2012
033	Linderman, L.E., Spencer, B.F.	Smart Wireless Control of Civil Structures	January 2014
034	Denavit, M.D. and Hajjar, J.F.	Characterization of Behavior of Steel-Concrete Composite Members and Frames with Applications for Design	July 2014
035	Jang, S. and Spencer, B.F.	Structural Health Monitoring for Bridge Structures using Wireless Smart Sensors	May 2015
036	Jo, H. and Spencer, B.F.	Multi-scale Structural Health Monitoring using Wireless Smart Sensors	May 2015
037	Li, J. and Spencer, B.F.	Monitoring, Modeling, and Hybrid Simulation: An Integrated Bayesian-based Approach to High-fidelity Fragility Analysis	May 2015